"Novel developments in Fourier domain optical coherence tomography and nonlinear tomographic interferometry"

Mallat, Kamel

Abstract

In this thesis we present novel methods to improve the limitations in Optical Coherence Tomography (OCT). They are divided into two parts. The first part deals with the axial resolution limitation in OCT systems. We give a description of the Fourier Domain OCT (FDOCT), and then we show theoretically how to enhance the axial resolution in a particular case of a two-layer sample where one of the two layers is moving continuously, while these two layers are separated by a distance lower than the physical axial resolution. The second part of the thesis demonstrates a novel full theoretical model that uses the second order autocorrelation interferometry technique in nonlinear optics to eliminate the strong background DC, and therefore enhance the imaging contrast. A femtosecond laser emits the light at 1300nm wavelength, it travels through a polarized beam splitter which divides the light in two orthogonal polarizations, one will probe the reference and the other will probe the sample. By...

Document type : *Thèse (Dissertation)*

UNIVERSITE CATHOLIQUE DE LOUVAIN

Faculty of Science

Institute of Condensed Matter and Nanosciences – IMCN

Nanoscopic Physics – NAPS

Thesis presented for the Ph.D. degree in Science - Physics

Kamel MALLAT

Novel developments in Fourier Domain Optical Coherence Tomography and Nonlinear tomographic interferometry

PhD committee

Prof. Xavier URBAIN (UCL) (Supervisor)

Prof. Alain CORNET (UCL) (Supervisor)

Prof. Bernard PIRAUX (UCL) (Chairperson)

Prof. Laurent FRANCIS (UCL) (Secretary)

Prof. Philippe ANTOINE (LAMBDAX, Belgium)

Prof. José Luis FERNANDEZ (University of Vigo, Spain)

Prof. Marc GEORGES (Liege Space Center, Belgium)

General introduction

In recent years, Micro Electro Mechanical Systems, known by the acronym MEMS have become a trend for microelectronics industries. Many kinds of micro-sensors based on MEMS technology [1] have been proposed in a wide range of applications such as gas, pressure, current, temperature measurements. But the most challenging issue for the industry is the packaging and the testing of the inside of these devices, due to its very small size and complex structure [2]. One of the major problems concerns the characterization of these MEMS, for example the extraction of their vibration frequency, the measurement of a step height or shape or the detection of inhomogeneity inside the MEMS. The Optical Coherence Tomography or OCT method presents a good noninvasive solution to characterize these MEMS.

OCT is based on optical two wave's interferometry (Michelson). It uses broadband light source with a short coherence length, to produce cross-sectional images at different depth scans. The backscattered light that comes from the multiple layers of a sample interferes with the light that is reflected by a reference mirror. The axial resolution of an OCT system is inversely proportional to the bandwidth of the laser source.

The complex structure of dynamic MEMS (e.g. accelerometer) requires sometimes working with multilayer sample, so it is likely possible that the distance between the layers is smaller than the axial resolution, which makes it impossible to separate the layers in the tomographic images.
Another issue is the presence of metal in the front face [3], which prevents the light from passing through the MEMS. This can be resolved by doing backside imaging, and the light will travel through silicon, which compels us to work in the infrared. But this will lead to a detected signal merged with

the continuous component (hereafter DC) due to the reflection from the unwanted interfaces before hitting the desired layer. This DC contains no useful information about the sample, it will affect the sensitivity [4] of the imaging system, and it may saturate the detector.

In this thesis we present novel methods to improve the limitations in Optical Coherence Tomography. These novel methods are divided into two parts.

The first part deals with the axial resolution limitation in OCT systems. We give a description of the Fourier Domain Optical Coherence Tomography (FDOCT), and then we show theoretically how to enhance the axial resolution in a particular case of a two-layer sample where one of the two layers is moving continuously, while these two layers are separated by a distance lower than the physical axial resolution. The idea is based on moving one of the layers continuously, and then by performing temporal analysis on the detected signal, we show that is possible to separate these two layers.

A complete description of the FDOCT system design is explained. The validation of the concept is done by using simulations and experimental measurements in this first part.

The second part of the thesis deals with the DC issue. We present a novel full theoretical model that uses the second order autocorrelation interferometry technique in nonlinear optics to cancel out the strong background DC, and therefore enhance the imaging contrast. A femtosecond laser emits the light at 1300nm wavelength, it travels through a polarized beam splitter which divides the light in two orthogonal polarizations, one will probe the reference and the other will probe the sample. By realizing the second harmonic generation, in type II configuration, it is possible to eliminate the DC. The setup is adapted, in an original manner, so as to realize interferometric measurements on the sample arm using three waves

coupling. A full description of the method with solid theoretical models justified by simulation and experimental results is presented in this part to validate the proof of concept.

This part of the thesis shows the possibility to use non-linear interferometry in order to provide interferometric measurements on a dark field even if strong parasitic light is reflected by the sample.

Contents

General introduction 3
Acknowledgements 9
Introduction 13
1. Fourier Domain and sub-axial resolution 17
1.1 Overview 17
1.2 FDOCT principles 19
1.3 Temporal analysis of a dynamic sample 23
1.4 Sub axial resolution using temporal analysis 25
1.5 Summary 29
2. Experimental proof of concept of sub-axial resolution 31
2.1 Experimental setup 31
2.2 Setup characterization 35
2.2.1 Lateral resolution 35
2.2.2 Sensitivity Fall Off 37
2.2.3 Calibration of the piezo (electric) actuator 39
2.3 Proof-of-concept experimental results 40
2.3.1 Large step displacement 41
2.3.2 Small step displacement 44
2.4 Summary 45
3. Nonlinear optics theory for the type (II) SHG 53
3.1 Overview 53
3.2 Polarization 55
3.3 Second Harmonic Generation (SHG) 56
3.4 Uniaxial crystals and index ellipsoid 59
3.5 The effective nonlinear coefficient 62
3.6 Phase matching 65

3.6.1 Type II phase matching $o+e\ SHGe$ 66
3.6.2 Type II phase matching $o+e\ SHGo$ 67
3.7 Summary 67
4. Nonlinear interferometry-Theory and simulation 69
4.1 Introduction to the autocorrelation technique for fast pulses characterization..... 69
4.2 Crossed orthogonal polarization autocorrelation..... 75
4.2.1 Theoretical demonstration of linear and nonlinear fringes in the case of orthogonal polarizations..... 76
4.2.2 Unbalanced return field case 79
4.2.3 Balanced return field case 87
4.2.4 Dispersion in one arm 87
4.3 Simulations..... 91
4.3.1 Unbalanced return field..... 91
4.3.2 Balanced return fields 104
4.3.3 Dispersion in one arm 108
4.3.3 Asymmetric Gaussian pulse envelope 115
4.6 Summary 125
5. Experimental setup and results..... 127
5.1 Setup..... 127
5.2 Femtosecond laser 129
5.2.2 Mode locking 131
5.2.2 Laser chain 133
5.3 Thin air wedge sample and Fizeau principles 139
5.4 Results and validation..... 141
5.4.1 Contrast of the Michelson Nonlinear fringes versus the angle for Balanced return field..... 141
5.4.2 Experimental Linear and nonlinear Michelson fringes versus delay..... 145

5.4.3 Experimental Fizeau fringes in linear OCT to calibrate the nonlinear OCT setup 148
5.4.4 Tomographic application using femtosecond gated method and FDOCT method..... 154
5.7 Summary 163
Conclusion and perspectives..... 164
Bibliography 169
Appendix A. Algorithm for separating two layers within the coherence length. 174
Appendix B. Unbalanced case: Eq (4.33) to (4.34) 178
Appendix D. TDOCT VS FDOCT 186
Appendix E. Fourier transform of the autocorrelation function using the formula (4.18) 187

Acknowledgements

I would like to thank my PhD advisors, Professors Alain Cornet and Xavier Urbain, for supporting me during these past years. Alain is someone you will instantly like and never forget once you meet him. He's the smartest person I know with very awesome sense of humor. I wish that I could be as lively, enthusiastic, and full of energy as Alain and to be able to command an audience as we as he can. Xavier has been very supportive and has given me the freedom to test and simulate different ideas without objection. He has also provided great help and insightful discussions about the research. I thank them both for helping me to finish the manuscript after reading the many version of it. I am also very grateful to Professor Philippe Antoine for the efforts he made to comment this manuscript, and I also thank him for believing in me in the very beginning with the opportunity to start this work.

I would like to thank enormously Professor José Luis Fernández from the University of Vigo (Spain) for the great collaboration that we have. I could say that this work wouldn't be done without the great experience and effort of José. I thank him deeply for letting me using their femtosecond laser source to achieve this work, for the guidance and for the great advices in the experiments and the writing of this manuscript. I am also very grateful for Cristina Trillo for starting this project.

Professor Laurent Francis is another person who gave without return, a lot of scientific guidance to help make this work possible. I thank him for trying always his best to make this work advance.

I thank deeply Bernard Piraux and Marc Georges for being part of my private defense and for all the effort and the comments that let me improve this manuscript.

I also would like to thank all my colleagues in our laboratory; I thank Marc Daman for his help when I had any questions about software or hardware. I also thank the creative Daniel Dedouaire for his fast response when I needed some pieces for the experiment, I am grateful to Nicole Coisman for all her fine administrate work that makes the scientific work flow easily. I thank Professor Pierre Defrance for all the encouragement, Amin Amin for his scientific help all these years, Amine Salhi for sharing his great knowledge, Abdessitir Deraoui for the scientific discussion and all the members of our laboratory.

I dedicate this thesis to my family because they gave me all the support and the encouragement. I thank my Mom and Dad for their infinite love and acceptance, I thank gratefully my two beloved sisters and my big brother for believing in me and in my choices.

First Part

Introduction

Recently, the demand from industrial organizations to characterize surface deformation in particular devices such as micro electromechanical system (MEMS) has increased [1], but the small size of these components has made direct contact with the sample difficult to achieve [2]. For this reason, non-contact methods like Optical Coherence Tomography OCT are used. OCT is an imaging technique with high spatial resolution [4, 5, 6]; it uses interferometric measurements based on low coherence source, in which the light is divided into two parts. The first part hits a reference mirror while the second probes the sample at a depth corresponding to optical contact, i.e. for equal distance traveled in both arms of the interferometer. The depth position through the sample can be determined using TDOCT or FDOCT [5]. FDOCT method gives a major advantage in measuring the vibration and the deformation because of its high acquisition speed (see comparison in Appendix D).

A major limitation in FDOCT is the axial resolution, and the presence of silicon constrains us to work with a proper wavelength range (1300nm-1600nm) to avoid silicon absorption. This limits the axial resolution to a few micrometers, between 4µm and 16µm [4]. As a result, if the distance between two layers is smaller than the physical axial resolution it would be impossible to discriminate them using this method. In other words, it would be impossible to detect the inhomogeneity or the roughness of the inner surface, since the two surfaces will be seen as one.

A solution to such problem is to use a light source with broader bandwidth, providing better resolution through reduced coherence length. The super luminescent diodes in the infrared have spectral bandwidths of 15-70nm, which means a corresponding coherence length in a range from 49 to

10µm; the quantum-dot SLED with 150nm bandwidth centered at 1.2µm has demonstrated a resolution of 4µm [7], but it suffers from insufficient power. Hui Wang *et al*. demonstrated a combined multiple-SLED broadband light source [8] at 1300nm with 145nm bandwidth (5µm axial resolution) with over 10mW of power. Femtosecond Ti:sapphire lasers achieved resolution lower than 1µm, but the centered wavelength was in the visible (800nm) which is not suitable for working with Silicon. These approaches depend on the extent of the spectral width of the source.

Other methods propose the improvement of the axial resolution without changing the source. Hitzenberger *et al*. suggested measuring the thickness of a thin foil located behind a dispersive medium [9]. Using the dispersion, we increase the width of the coherence envelope and therefore we improve the axial resolution, this method has its limitation when the source is not Gaussian, because the shape of the source has an influence on the exact width of the coherence envelope. Another method was proposed by Zhang *et al*. based on destructive interference [10]. It uses the superposition of interference of the signal light with three reference mirrors instead of one; however if the wavelength fluctuation is larger than 10nm this method is not recommended. Chang *et al*. proposed a theoretical three–step method to enhance the axial resolution of an OCT system [11], but this method needs a movable arm so it cannot be applied to the Fourier-domain OCT. Bousi *et al*. proposed a method which works on time domain OCT; it improves the axial resolution by a factor of 7. It is based on step-frequency encoding using frequency shifting [12]. These methods cannot achieve a super resolution which is essential for the detection of inhomogeneity in MEMS.

Many methods have been proposed for dynamic MEMS characterization. Shavrin *et al*. proposed a stroboscopic white-light interferometry to characterize out-of-plane surface vibration [13]. Using the temporal analysis of the phase they extracted the amplitude of the MEMS

vibration with a precision of few nanometers. Zhong *et al*. introduced a new technique for quantitatively characterizing the vibration and the inner structure of a sample in real time [14]. They used the FDOCT to characterize vibrations with a frequency up to 250Hz with an axial resolution of 1µm. This method works fine, but the central wavelength 650nm was far from our goal which is the infrared.

To overcome this physical limitation, we propose a novel method that can extract the frequency and improve the axial resolution. This method can be applied to dynamic MEMS only and uses the FDOCT setup. The idea is to activate one of two closely lying surfaces (this can be done electrically). The OCT signal is then acquired as a function of time and then processed in the Fourier domain in order to isolate the component that oscillates at the driving frequency from the other component. By using this method, which will be explained later in more details, we can improve the axial resolution of our OCT system and we will be able to resolve the two surfaces.

Figure 0.1 shows the idea of our method. The red peak represents the reflected intensity from the fixed layer noted as layer 2; the blue peak represents the reflected intensity from the oscillating layer noted as layer 1. We see clearly that the distance between the two peaks is lower than the axial resolution; therefore we observe only the black curve which contains the information about layer1 + layer 2.

By applying the Fourier transforms from time to frequency domain, and since one of the two layers is oscillating continuously, we will be able to isolate and separate the two peaks (layers), therefore improving the axial resolution.

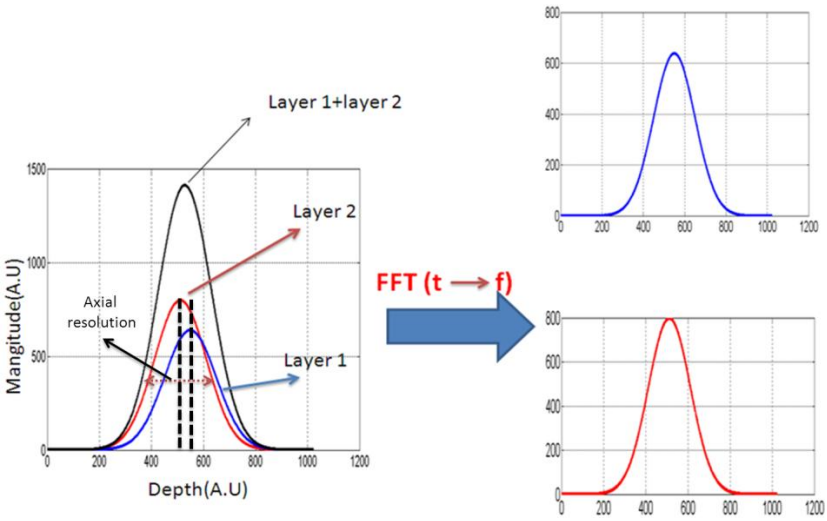

Figure 0.1 Reflectivity versus depth for two layers where the distance is within the axial resolution, on the right: Separation of the two layers

This part contains two chapters.

- In chapter 1 we introduce the Fourier domain OCT, then we develop the novel theoretical model to improve the axial resolution.
  This model is based on a two layers sample.
- In chapter 2 we describe the experimental setup used to realize the proof of concept of this method. We show experimental results which validate the concept.

1. Fourier Domain and sub-axial resolution

In this chapter, we introduce the Fourier Domain Optical Coherence Tomography. We describe the principles of FDOCT and its limitations, and then we talk about the axial resolution issue. We then show how to make temporal analysis of a dynamic sample, to extract the frequency and amplitude of the oscillation. We finish by explaining the theory on how to improve the axial resolution using temporal analysis.

1.1 Overview

Optical coherence tomography (OCT) is a non-invasive optical imaging method that obtains depth structures even in weakly diffusing samples (often used in ophthalmology); it uses the light with shorter wavelength to reach higher axial resolution. On the other hand, the attenuation in the sample is higher when the wavelength is short, therefore the OCT can achieve 1-3mm penetration depth in transparent samples [4].

OCT is a technique that uses Michelson interferometry; it was first introduced by Huang *et al.* in 1991. It is based on the interference between the recombined broadband light field from a reference arm mirror and the sample arm as presented in *Figure 1-1*. We observe interference fringes when the optical path lengths of the sample and reference arm coincide within the coherence length, which can be determined by the temporal coherence of the light source. The axial resolution of an OCT interferometry for a specific central wavelength is inversely proportional to the bandwidth of the light source [4, 5, 6]. The variation of the refractive index between layers in the sample will appear as intensity peaks in spatial domain when performing the Fourier transform of the interference signal in the case of FDOCT.

OCT can be used as 2D or 3D imaging technique, where the 2D image can be observed by using a galvanometric scanner, which will perform lateral scans in the two directions (horizontal and vertical direction) which are perpendicular to illumination axis.

The 3D image is obtained by acquiring one depth scan; the depth scan can be done by using a translating mirror to change the reference path length, therefore to match the multiple optical paths within the layers of the sample. This method is called Time Domain OCT. We can also obtain depth information using Fourier domain OCT, where the broadband interference is acquired with spectrally separated detectors as a function of the wavenumber. Then by performing a Fourier transform of the acquired data from the wavenumber domain to the spatial domain we will get the depth information. Note that in this case there is no need for any mechanical movement of the reference mirror, and the depth scan can be done with a single measurement.

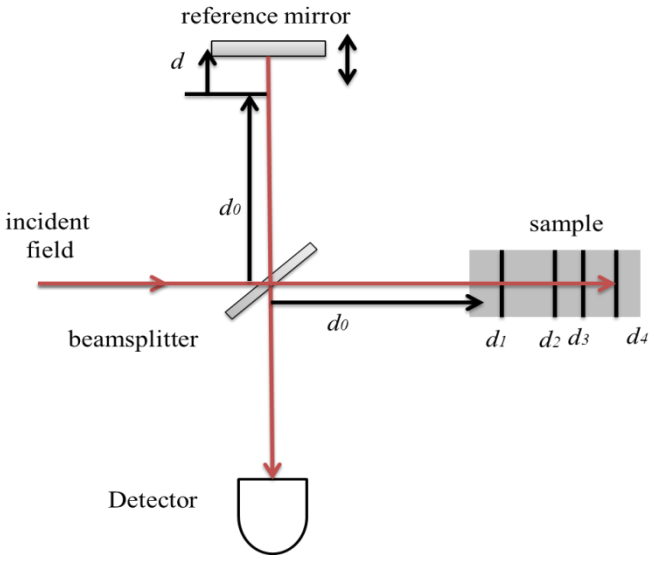

Figure 1-1 Michelson interferometer, Time Domain OCT

1.2 FDOCT principles

In FDOCT we do not need a moving reference mirror to scan the reference path through depth; this gives a major advantage against the time domain OCT (see Appendix D)[15]. FDOCT has also a better SNR comparing to TDOCT [15]. The axial depth profile is obtained from the Fourier transformation of the spectrum. We use a broadband light source, and the interferometer output spectrum is detected using an array of detectors (CCD line camera). Combined with a spectrometer the depth profile is measured from that spectrum without moving the reference arm mirror. It is possible to acquire video images using a high speed CCD camera.

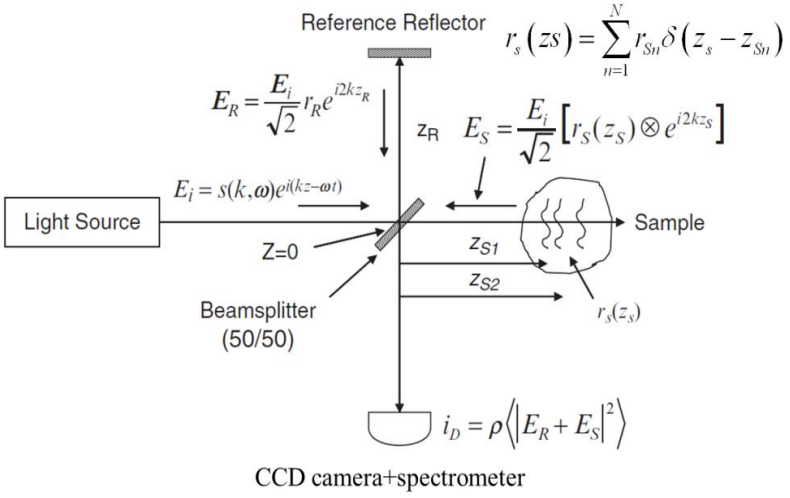

Figure 1-2 Schematic figure of the Fourier Domain OCT system

A typical OCT is shown in *Figure 1-2*. The interferometer is illuminated by a polychromatic wave; the light is split by a *50/50* beam splitter in an ideal situation. A part of the light will probe the fixed mirror considered as the reference arm, the other part will probe the multilayer sample. We define the field in each part of the interferometer:

Light field from the source:

$$E_{in}(k) = s(k)e^{j(kz)} \tag{1.1}$$

Reference field: the field after reflection by the fixed mirror

$$E_R(k) = \frac{E_{in}}{\sqrt{2}} r_R e^{j2kz_R} \tag{1.2}$$

Sample field: the field after reflection by the multilayer sample

$$E_S(k) = \frac{E_{in}}{\sqrt{2}} \sum_{n=1}^{N} r_{sn} e^{j2kz_{S_n}} \tag{1.3}$$

The sum in this equation comes from having multiple interfaces with different reflection coefficients.

$s(k)$ is the source spectrum, r_{sn} is the reflection coefficient from each layer of the sample, and r_R is the reflection coefficient from the reference arm; z_R and z_{S_n} are the positions of the reference and n^{th} sample reflector, respectively, *k* is the wavenumber and *N* is the number of layers.

The light fields from the reference and the sample arms are mixed in the coupler and travel to the detector. Optical detectors are sensitive to the square of fields, therefore:

$$I_D(k) \propto \left|E_R + E_S\right|^2 = \left[\left|E_R\right|^2 + \left|E_S\right|^2 + 2\,\mathrm{Re}\left(E_R E_S\right)\right] \tag{1.4}$$

Note that the detector photocurrent $I_D(k)$ depends on the wavenumber due to the use of a grating.

By combining equations(1.1), (1.2), (1.3) and (1.4) we obtain:

$$\begin{aligned} I_D(k) \propto & \left[S(k)\left(R_R + R_{S_1} + R_{S_2} + R_{S_3} + \ldots\right)\right] \ \underline{\text{DC}} \\ & + [S(k)\sum_{n=1}^{N}\sqrt{R_R R_{Sn}}\left(e^{j2k(z_R - z_{S_n})} + e^{-j2k(z_R - z_{S_n})}\right) \ \underline{\text{Cross-Correlation}} \\ & + [S(k)\sum_{n\neq m=1}^{N}\sqrt{R_{S_m} R_{S_n}}\left(e^{j2k(z_{S_m} - z_{S_n})} + e^{-j2k(z_{S_m} - z_{S_n})}\right) \ \underline{\text{Auto-correlation}} \end{aligned} \tag{1.5}$$

where $S(k) = |s(k)|^2$ is the source power spectral density, R_R is the reference arm's reflectivity, and R_{Si} is the individual interface's reflectivity in the sample arm.

Equation (1.5) can be written as follows:

$$I_D(k) \propto \begin{pmatrix} R_R + \sum_{n=1}^{N} R_n & \underline{\text{DC}} \\ +2\sqrt{R_R}\sum_{n=1}^{N}\sqrt{R_n}\cos\left(2k(z_R - z_{S_n})\right) & \underline{\text{Cross-Correlation}} \\ +2\sum_{n=1}^{N}\sum_{n\neq m=1}^{N}\sqrt{R_n R_m}\cos\left(2k(z_m - z_{S_n})\right) & \underline{\text{Auto-correlation}} \end{pmatrix}$$

(1.6)

The first line represents the non-interferometric spectral signal; it is the DC term which corresponds to the reflection from each arm regardless the presence of interferences. In reality the reflection from the sample arm is negligible compared to the reflection from the reference arm; therefore the reflection from the reference arm will dominate the DC term.

The second line represents the cross-interferometric signal, it represents the interference between the reference beam and each layer of the sample, it is proportional to the sum of the square root of the sample's reflectivity coefficients, and they are typically smaller than the DC component, because we consider that the reflection that comes from the sample is always smaller than the reflection that comes from the mirror.

The third line represents the autocorrelation signal; it corresponds to the interference between reflections on different layers of the sample, which is present regardless the presence of the reference. But it can be negligible if we choose a proper reference reflectivity. In other words, if the coefficient $R_R \gg R_{n,m}$ (Reference arm's reflectivity is a lot larger than the individual

interface's reflectivity of the sample arm), the third line or the autocorrelation will be negligible.

The source power spectral density is assumed to have a Gaussian form or can be reshaped numerically to a Gaussian; it is convenient to use such form in modelling, because it approximates the spectrum of the actual light sources and also has useful Fourier transform:

$$S(k) = \frac{1}{\Delta k\sqrt{\pi}} e^{-\left(\frac{k-k_0}{\Delta k}\right)^2} = \frac{1}{\Delta k\sqrt{\pi}} e^{-\left(\frac{k}{\Delta k}\right)^2} \otimes \delta(k-k_0) \qquad (1.7)$$

k_0 represents the central wavenumber of the light source spectrum , Δk represents its spectral bandwidth and $\otimes$ corresponds to the convolution symbol. We calculate its inverse Fourier transform or what is called the point spread function (PSF):

$$\Upsilon(\mathrm{z}) = \mathrm{TF}\left[\mathrm{S}(\mathrm{k})\right] = e^{-z^2\Delta k^2}.e^{j2k_0 z} = H(z)e^{j2k_0 z} \qquad (1.8)$$

where z is the distance between the beam splitter and the object and $H(z) = e^{-z^2\Delta k^2}$. Hereafter we note the optical path $z' = 2z$.

The main characteristic of the PSF is its full width at half maximum (FWHM), which corresponds to the coherence length (axial resolution) of the light source defined by:

$$l_c = \frac{2\ln(2)}{\pi}\frac{\lambda_0^2}{\Delta\lambda} \qquad (1.9)$$

Here, $\lambda_0 = 2\pi / k_0$ is the center wavelength of the light source and $\Delta\lambda$ is its wavelength bandwidth, defined as the FWHM of its wavelength spectrum.

$\Upsilon(\Delta \mathrm{z})$ is a complex number with an amplitude $e^{-\Delta z^2\Delta k^2}$ and a phase $2k_0\Delta z$ which is linear versus Δz when taking into consideration that Δz is smaller than $\lambda_0/2$.

The detected intensity spectrum from equation (1.6) is then Fourier transformed into the spatial domain, to reconstruct the depth-resolved optical structure of the sample.

Considering that the sample contains two layers only, we obtain:

$$\begin{aligned} i_D(z) &= TF\left[I_D(k)\right] \\ &\propto \left[\Upsilon(z)\left(R_R + R_{S_1} + R_{S_2}\right)\right] + \\ \Upsilon(z)\otimes &\left(\begin{array}{l} \sqrt{R_R R_{S_1}}\left[\delta\left(z' + 2\left(z_R - z_{S_1}\right)\right) + \delta\left(z' - 2\left(z_R - z_{S_1}\right)\right)\right] \\ + \sqrt{R_R R_{S_2}}\left[\delta\left(z' + 2\left(z_R - z_{S_2}\right)\right) + \delta\left(z' - 2\left(z_R - z_{S_2}\right)\right)\right] \end{array}\right) + \\ \Upsilon(z)\otimes &\left(\sqrt{R_{S_1} R_{S_2}}\left[\delta\left(z' + 2\left(z_{S_1} - z_{S_2}\right)\right) + \delta\left(z' - 2\left(z_{S_1} - z_{S_2}\right)\right)\right]\right) \end{aligned} \quad (1.10)$$

Hereafter we consider that the auto-correlation term is negligible, we justify this by choosing a proper reference with dominant reflective coefficient ($\sqrt{R_{S_1} R_{S_2}} \ll \sqrt{R_R R_{S_2}}$ *and* $\sqrt{R_R R_{S_1}}$), therefore (1.10) becomes:

$$\begin{aligned} i_D(z) &\propto \left[\Upsilon(z)\left(R_R + R_{S_1} + R_{S_2}\right)\right] \qquad (DC) \\ &+ \Upsilon(z)\otimes \left(\begin{array}{l} \sqrt{R_R R_{S_1}}\left[\delta\left(z' + 2\left(z_R - z_{S_1}\right)\right) + \delta\left(z' - 2\left(z_R - z_{S_1}\right)\right)\right] + \\ \sqrt{R_R R_{S_2}}\left[\delta\left(z' + 2\left(z_R - z_{S_2}\right)\right) + \delta\left(z' - 2\left(z_R - z_{S_2}\right)\right)\right] \end{array}\right) \\ &\qquad (Cross - correlation\ term) \end{aligned}$$

(1.11)

1.3 Temporal analysis of a dynamic sample

We show in *Figure 1-3* the A scan (Intensity versus depth) of a two-layers sample, it is based on the equation found in(1.11). The peak at zero corresponds to the DC term; the peak at the position $2(z_R - z_{S1})$ corresponds to the interference between the layer 1 and the reference mirror, and the

position $2(z_R\text{-}z_{S2})$ corresponds to the interference between the layer 2 and the reference mirror. The relative displacement of each sample interface from the reference position is multiplied by 2, which can be explained by the round trip of the light to each interface. Each peak has a Gaussian shape with FWHM (full width at half maximum) equal to the coherence length; this comes from the PSF function $\Upsilon(z)$. The symmetric shape of this figure is explained by the mathematical definition of the Fourier transform, the complex conjugate artifact comes from the fact that the detected intensity is real, so its Fourier transform should be Hermitian symmetric. The falloff sensitivity or the decreasing in the intensity of each peak versus the depth comes from the spectrometer which has a limited spectral resolution, which can be modelled by a Gaussian function. The convolution of this Gaussian with the spectrum intensity[1] will lead to a decrease in the intensity away from the optical contact [16].

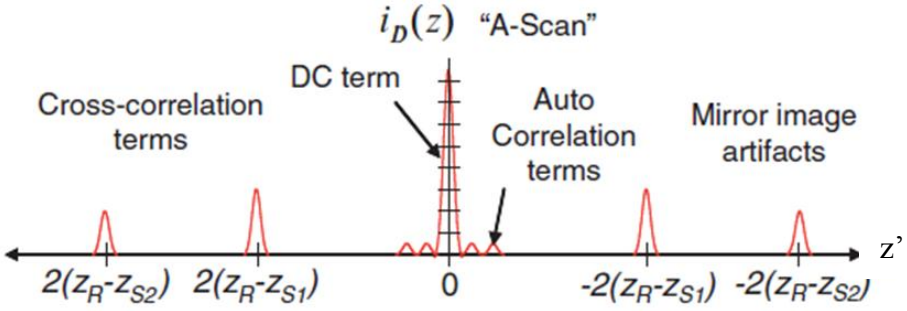

Figure 1-3 Intensity versus depth, the two layers are spatially separated in the Fourier domain

The contribution of each layer to $i_D(z)$ can be written as a complex number with amplitude and a phase, therefore:

[1] $i_D(k) \otimes exp\left(\frac{-\ln(2)k^2}{\delta_r^2}\right) \overset{F}{\leftrightarrow} i_D(z').exp\left(\frac{-z'^2\delta_r^2}{4\ln(2)}\right)$ where δ_r represents the spectral resolution of the spectrometer; it corresponds to the FWHM spectral resolution.

$$\tilde{Z}_{Layer1,2} = A_{1,2} e^{j\varphi_{1,2}} \tag{1.12}$$

Where $A_{1,2} = \sqrt{R_R R_{S_{1,2}}}\, H\left(z' \pm 2\left(z_R - z_{S_{1,2}}\right)\right)$

And $\varphi_{1,2} = k_0\left(z' \pm 2\left(z_R - z_{S_{1,2}}\right)\right) = 2k_0 X_{1,2}$

with $2X_{1,2} = z' \pm 2\left(z_R - z_{S_{1,2}}\right)$;

Note that the phase expression of each peak is dependent on the depth position. It is possible to set $X_{1,2}=0$ if $z=(z_R-z_{S1,2})$. This means that if we locate the exact position of the center of the peak 1 or 2, its phase becomes equal to zero.

If we suppose now that the second layer is moving periodically, its phase expression changes and it becomes:

$$\varphi_2 = 2k_0\left(X_2 + a_p sin(2\pi f_0 t)\right) \tag{1.13}$$

Where a_p is the vibration amplitude and f_0 its frequency.

The Fourier transform of this phase expression from time domain to frequency domain:

$$\mathrm{TF}\left[\varphi_2(t \to f)\right] = 2k_0 X_2 \delta(f) + \frac{k_0 a_p}{j}\left[\delta(f + f_0) - \delta(f - f_0)\right] \tag{1.14}$$

We are able from this equation to extract the amplitude a_p and the frequency f_0 of the dynamic interface, by applying a band-pass filter to the oscillating component in (1.14).

1.4 Sub axial resolution using temporal analysis

We consider this time that the two layers are not spatially separated in the Fourier domain, in another words the distance between the two layers

is lower than the coherence length, see *Figure 1-4*. In fact the contributions of the 2 layers are overlapped when we plot the intensity versus depth.

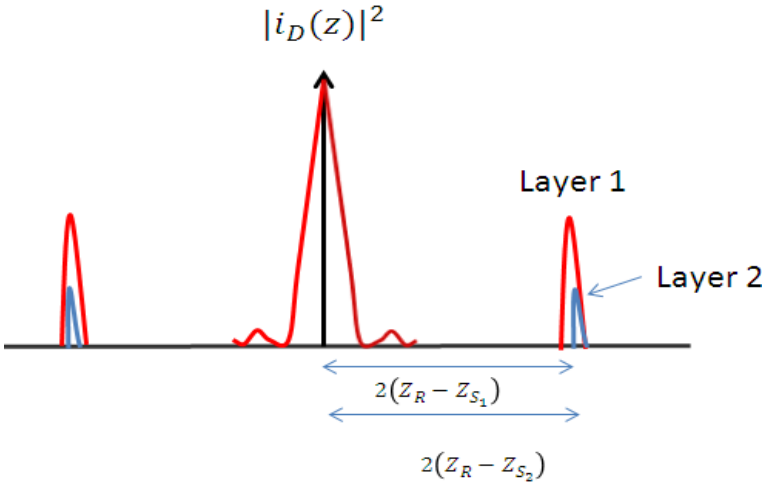

Figure 1-4 Intensity versus depth, the distance between the two layers is smaller than the coherence length

Since the two layers are located within the coherence length, the two complex numbers described previously become a single number, so by using equation (1.12) we can write:

$$\begin{aligned}\tilde{Z}_{Layer} &= \tilde{Z}_{Layer1} + \tilde{Z}_{Layer2} = A_1 e^{j\varphi_1} + A_2 e^{j\varphi_2} \\ &= A_1 e^{j2k_0 X_1} + A_2 e^{j2k_0(X_2 + a_p sin(2\pi f_0 t))} \\ &= A_1 e^{j2k_0 X_1} + A_2 e^{2jk_0 a_p sin(2\pi f_0 t)} e^{j2k_0 X_2}\end{aligned} \tag{1.15}$$

In order to determine the phase of this expression, we suppose that the approximation $2k_0 a_p \ll 1$[1] is valid. This is justified by the fact the amplitude vibration a_p is no more than a few nanometers in our experimental setup.

We recall the definition of the n[th] order Bessel as a function of the first kind:

[1] The amplitude a_p should be lower than 260nm if the central wavelength is 1550nm.

$$e^{j\alpha\sin(2\pi f_0 t)} = \sum_{n=-\infty}^{n=\infty} J_n(\alpha) e^{j2\pi n f_0 t} \tag{1.16}$$

If $\alpha << 1$:

$$J_0(\alpha) = 1$$

$$J_1(\alpha) \approx \frac{1}{2}\alpha$$

$$J_{-1}(\alpha) \approx -\frac{1}{2}\alpha$$

By applying this definition to the expression $e^{2jk_0 a_p sin(2\pi f_0 t)}$, it becomes:

$$e^{2jk_0 a_p sin(2\pi f_0 t)} = \sum_{q=-\infty}^{+\infty} J_q\left(2k_0 a_p\right) e^{j2\pi q f_0 t} \tag{1.17}$$

By developing the Bessel function to the first order:

$$e^{2jk_0 a_p sin(2\pi f_0 t)} = 1 + k_0 a_p e^{j2\pi f_0 t} - k_0 a_p e^{-j2\pi f_0 t} \tag{1.18}$$

By combining (1.18) and (1.15) we obtain:

$$\tilde{Z}_{Layer} = A_1 e^{j2k_0 X_1} + \left[1 + k_0 a_p e^{j2\pi f_0 t} - k_0 a_p e^{-j2\pi f_0 t}\right] A_2 e^{j2k_0 X_2} \tag{1.19}$$

Now by doing the Fourier transform from time domain to frequency domain we get:

$$\begin{aligned} TF[\tilde{Z}_{Layer}] = &\left[A_1 e^{j2k_0 X_1} + A_2 e^{j2k_0 X_2}\right]\delta(f) \\ &+ A_2 k_0 a_p e^{j2k_0 X_2}\left[-\delta(f - f_0) + \delta(f + f_0)\right] \end{aligned} \tag{1.20}$$

We present in *Figure 1-5* the Fourier transform of $\tilde{Z}_{Layer}$ from time domain to frequency domain. The frequency f_0 can be determined directly from this figure by locating the red peak. $A_2 k_0 a_p$ represents the amplitude calculated at the frequency f_0 which is proportional to A_2 if the product $k_0 a_p$ is fixed. Note that the value k_0 is known and is equal to $2\pi/\lambda_0$.

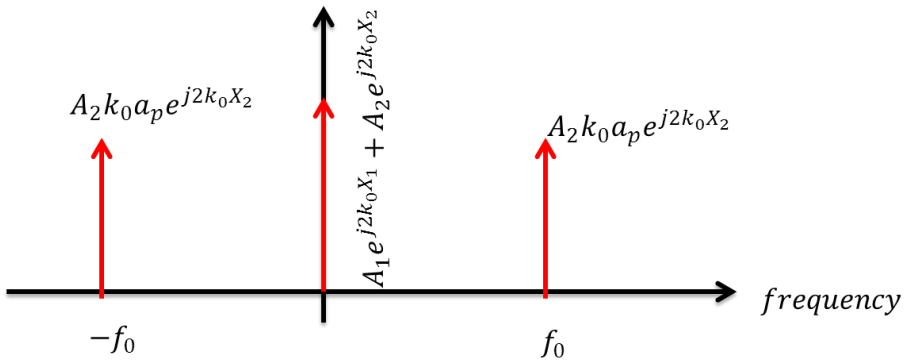

Figure 1-5 Fourier transform of the complex number resulting from the combination of the two peaks

Now by applying a band pass filter to the oscillating component, then by operating the inverse Fourier transform of equation (1.20) will get the position of the hidden layer and its reflectivity, see *Figure 1-6*. So a_p can be calculated directly by knowing the value of A_2.

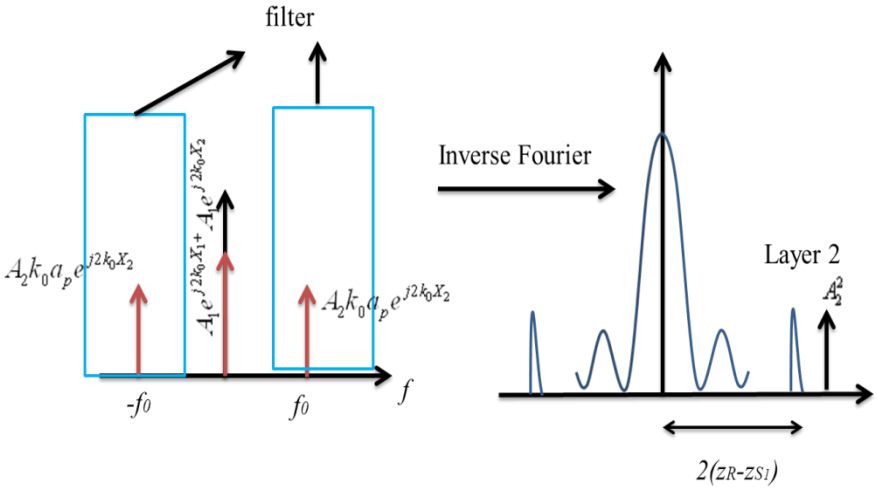

Figure 1-6 Inverse Fourier transform after applying a band-pass filter to isolate the oscillating component

1.5 Summary

In this chapter, we presented the FDOCT. We then explained the step-by-step theoretical calculation to obtain the depth intensity profile. We also showed the graph of this intensity profile vs depth and commented each part of this figure. We then described and demonstrated theoretically how to extract the frequency and the amplitude of the motion of a dynamic sample. We ended up by demonstrating how to improve the axial resolution using temporal analysis on a dynamic sample. We summarize our strategy by the following steps:

- We perform the first FT on the spectrum intensity from wavenumber domain to depth domain, to obtain the reflectivity of combined layers versus depth.
- We acquire the temporal signal from both layers versus time
- We perform the second FT on the temporal signal from time domain to frequency domain.
- We apply notch filtering to the oscillating component
- We perform inverse FT on the filtered signal to the depth domain to locate the hidden layer.

2. Experimental proof of concept of sub-axial resolution

In this chapter we describe the Fourier Domain OCT setup and we give a brief description of its essential elements. We then quantify the characteristic of this setup by determining the spatial and the axial resolutions. We then show some experimental results to validate the proof of concept using a dynamic sample consisting of a mirror mounted on a piezo actuator.

2.1 Experimental setup

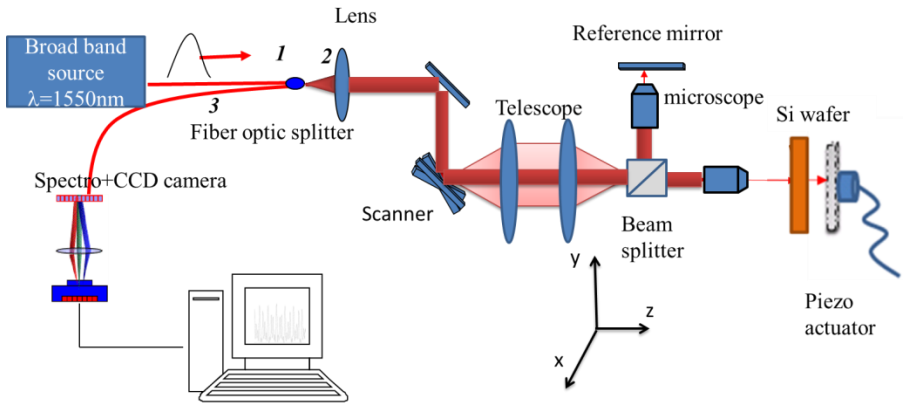

Figure 2-1 Diagram of FDOCT system. In the sample arm we have a fixed silicon wafer just before a mirror mounted on a piezo crystal

Figure 2-1 represents the schematic diagram of our Fourier-domain optical coherence tomography setup. The light from a fibred broadband laser source is sent into a Michelson interferometer through a two-way fiber optical splitter. The divergent light from the fiber optic will go from the direction 1 to 2 to pass through a biconvex lens which collimates the beam. The light is then reflected by two mirrors mounted on a galvanometric

scanner. The light continues passing a telescope and is then split into a reference and a sample beam by a beam-splitter (50/50). Both the object image and reference image are formed at the entrance slit of a broadband CCD-based spectrometer (iHR320**).** Interference occurs when both the object image and the reference image are spatially matched in size and orientation, and their optical path lengths are matched within the coherence length of the light source.

The light travels through a silicon sample of 200μm thickness with front and back polished surfaces. The light then hits a mirror attached to a piezo actuator which can be activated by a low frequency generator that acts as the vibration exciter. The reflected light from the reference arm interferes with the one from the sample arm, through the fiber-optic splitter in the direction 2 to 3. Thus a spectrometer combined with a CCD camera detects the return of the light. The acquisition is controlled using a Labview program.

We enumerate and give a brief description of the essential pieces of our setup:

- Camera

The selection criteria of the camera were: a high speed of acquisition, maximum sensitivity in the Fourier domain of our source and a high number of pixels. For this purpose, we have chosen SUI LDH NIR digital line scan camera manufactured by Goodrich Sensors Unlimited (USA)[1]. It has a high speed scanning rate (46000 A-scans/s), based on a 1024 pixels linear array, 47 kHz readout rate. The wavelength response range is from 0.8 to 1.7 microns.

[1] http://www.sensorsinc.com/downloads/SU-LDH.pdf

- Spectrometer

We have used the iHR320 Horiba[1] grating spectrometer in transmission mode. The focal length of the iHR320 is 0.32m and is designed for great image quality; it gives the spectral measurements and it can perform multi-tracking experiments with up to 20 fiber inputs. We have chosen the minimum and the maximum wavelength of our grating symmetrically around the central wavelength 1550nm of the laser source, therefore:

$$\lambda_{min} = \lambda_0 - \Delta\lambda / 2 = 1550 - 105/2 = 1497.5nm$$
$$\lambda_{max} = \lambda_0 + \Delta\lambda / 2 = 1550 + 105/2 = 1602.5nm.$$

The spectral coverage with 25.6mm CCD length is 105nm, so we have a dispersion of 105/25.6=4.10nm/mm.

- 2D scanner

We used a XY Galvanometric Motor VM500+[2] with a 4-6mm clear aperture. It offers high dynamic performance along with high accuracy and instrument grade performance. It has a maximum scan angle of 40 degrees, an offset drift with 50 μRadians/^{o}C in average and small step time around 200μs.

- Laser source:

The light source is an important part of the OCT system. OCT imaging requires a broad bandwidth and a short low-coherence length, note that the penetration depth is proportional to the wavelength. Working with Silicon requires infrared wavelengths. We have in our laboratory two broadband

[1] http://www.horiba.com/us/en/scientific/products/optical-spectroscopy/spectrometers-monochromators/ihr/ihr320-imaging-spectrometer-198/
[2] http://www.camtech.com/index.php?option=com_content&view=article&id=87&Itemid=75

sources, ASE (Amplified Spontaneous Emission) and a Fianium. Both laser systems are fiber connected.

The ASE source has a maximum power output of 37.5mW, a central wavelength 1550nm, and a full width at half maximum (FWHM) of 14nm, which is obtained after reshaping numerically the measured spectrum to a Gaussian form, see *Figure 2-2*. The magnitude versus depth is presented in the *Figure 2-3*, which is obtained by operating the Fourier transform of the reshaped Gaussian spectrum from *Figure 2-2*. We present only the part that interests us for the determination of the axial resolution $\delta_z = 76\mu m$.

The Fianium source has a maximum power output of 4 W; it is connected to a fiber Bragg grating[1] filter with multiple outputs (many central wavelengths) including 1550nm and 1370nm. For the 1550nm we have a full width at half maximum (FWHM) of 55nm which is obtained after reshaping the measured spectrum to a Gaussian form, see *Figure 2-4*. This source provides an axial resolution of $\delta_z = 19\mu m$, see *Figure 2-5*.

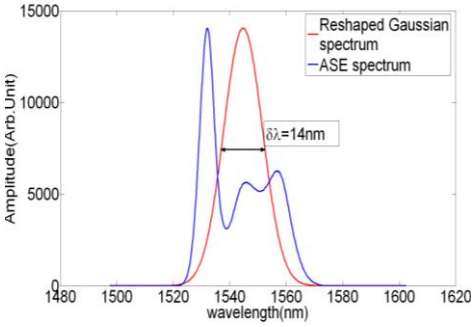

Figure 2-2 ASE amplitude spectrum versus wavelength

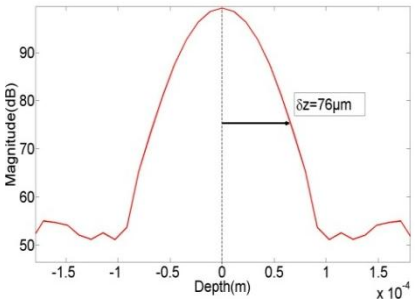

Figure 2-3 FFT of the reshaped Gaussian spectrum, magnitude versus depth

[1] A **fiber Bragg grating** (**FBG**) is a type of distributed Bragg reflector constructed in a short segment of optical fiber that reflects particular wavelengths of light and transmits all others.

We have adopted the ASE source since it has a bigger axial resolution, which is more suitable for our proof of concept.

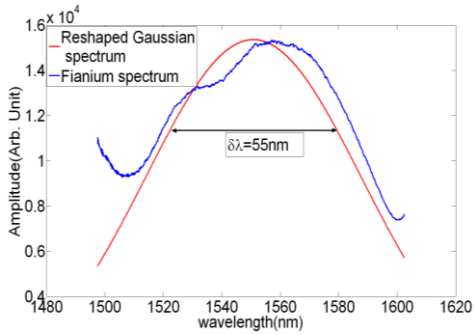

Figure 2-4 Fianium amplitude spectrum versus wavelength

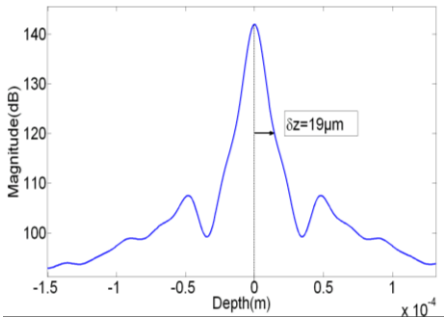

Figure 2-5 FFT of the reshaped Gaussian spectrum, magnitude versus depth

2.2 Setup characterization

2.2.1 Lateral resolution

The lateral resolution depends on the numerical aperture of the optics used in the system; it is determined by the degree of light focusing onto the sample.

The microscope objective used in our setup to acquire the images, has a numerical aperture of 0.4(20X). The theoretical transverse resolution is then 2.4μm[1]. The experimental transverse resolution can be obtained by imaging a Mire test. The USAF 1951 resolution test target[2] consists of many groups of 3 bars targets, each group has six elements; the smallest element

[1] The transverse resolution is based on the Rayleigh criterion and it can be calculated $\Delta x = \frac{0.61\lambda}{NA}$

[2] http://en.wikipedia.org/wiki/1951_USAF_resolution_test_chart

detected using the intensity profile across the 3 bars, leads us to determine the resolution using the formula:

$$resolution = 2^{group + \frac{element - 1}{6}} \tag{2.1}$$

We acquired a volume of dataset scans across the test target by using it as a sample in the setup described in *Figure 2-1*. The acquisition is realized using a Labview program. The highest frequency that could be visually resolved is in group 7 element 6, see *Figure 2-6*, and it is justified by plotting the intensity profile across the 3 bars versus pixels; the result is shown in *Figure 2-7*. By using the equation (2.1) , the minimum resolution is estimated to be 4.2 µm. Note that we have inserted a telescope to obtain this number, but we were limited by the space in our setup, the difference comes probably from not having perfect optical alignment.

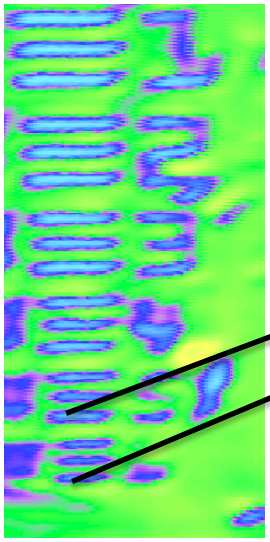

Figure 2-6 Image of the Mire captured by our setup

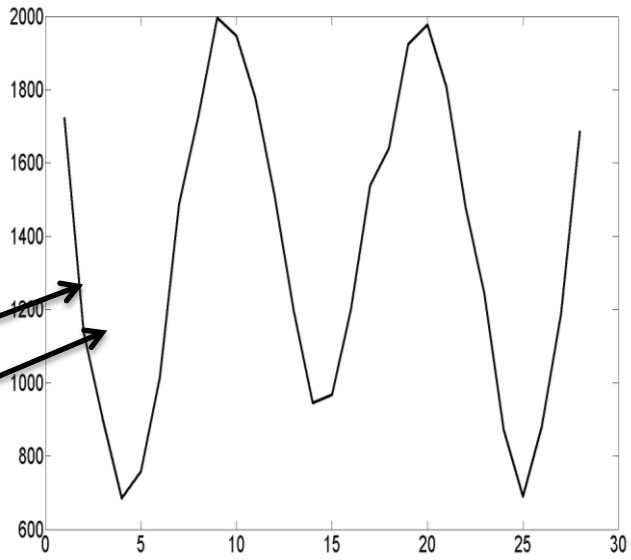

Figure 2-7 test element 7-6, intensity profile versus pixel

2.2.2 Sensitivity Fall Off

The fall off is determined by the spectral resolution of the spectrometer, it's one of the main disadvantages of FDOCT; we talked about this previously in *Figure 1-3*. By using the same power and by positioning the same reflector at different depths we get different signal magnitudes. The signal magnitude in the z space is reduced when positioning the reflector away from the zero path length difference.

This is due to the interference washout at large path length differences, and is dependent on the finite size of individual pixels and the spectrometer optics which determines the spectral sampling. We used the ASE laser presented earlier in *Figure 2-2*. We see a series of different axial profiles (A lines) versus depth which are combined in *Figure 2-8*, for which we used the classic OCT setup. For each position of the reflector we acquired the imaging depth using our FDOCT setup with the help of the CCD camera combined with the Spectrometer.

To understand why we observed this fall off in the sensitivity, we present in *Figure 2-9* , the effect of different focusing optics on the detected interference modulation resulting from different positions of the sample. On the left: we have an ideal case where the focused Gaussian beam is the smallest and is contained within one pixel (around the optical contact), so the sensitivity is high. On the right (far from the optical contact): we have a large focal spot resulting in a loss of light and spectral cross talk between pixels, in this case the sensitivity is smaller compared to the ideal case.

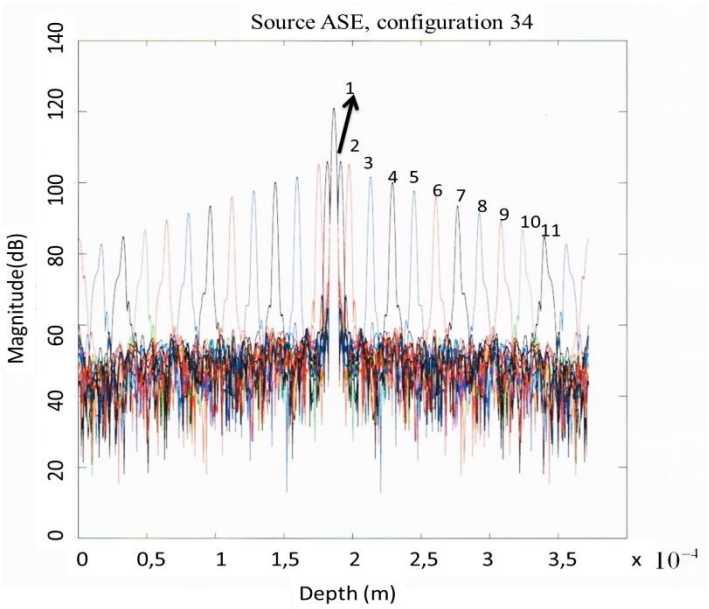

Figure 2-8 fall off curve, different magnitude from the same reflector at different position.

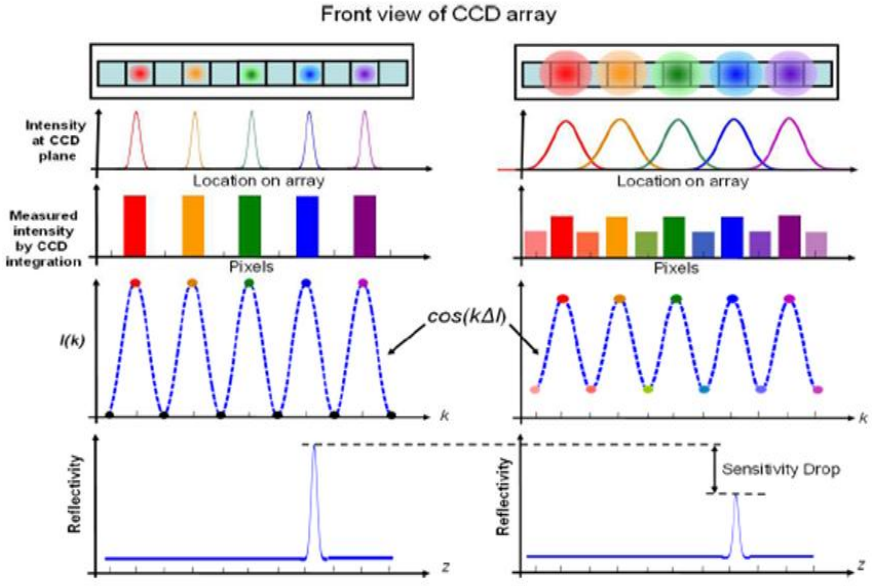

Figure 2-9 How the focusing affects the detected interference modulation. Left: the normal case where the focus is contained inside the pixel. Right: large focus results in loss of light. The choice of the spot light color is for illustration only.

This experience shows that in order to obtain maximum sensitivity we need to work with an interferometer with equal arm lengths.

2.2.3 Calibration of the piezo (electric) actuator

The piezo is an important part of our setup because it constitutes, combined with the silicon slice, our sample. The silicon slice was not used for the calibration, only the mirror that was fixed on the piezo was used. Using the same setup described in *Figure 2-1*, the reference arm is a static mirror and the mirror mounted on a piezo without the silicon slice is our new sample. The piezo is connected to a function generator with a range from 0 to 10 volt. We show in *Figure 2-10* the response of the piezo displacement versus the voltage. The piezo is calibrated by setting the frequency of the generator at 14 kHz for all the measurements; each measurement is obtained in 3 steps:

- Acquire the spectrum[1] (Intensity versus wavenumber)
- Perform the Fourier transform[2] of the spectrum in order to get the intensity versus depth.
- Locate numerically the peak[3] which corresponds to the vibrating mirror surface.

Now by calculating the Fourier transform of the phase variation of the located peak versus time, we use the equation (1.14) to extract the frequency and the amplitude.

By analyzing *Figure 2-10*, the piezo should be used between 2 and 8V, to maintain its linear response; above 8V we observe nonlinear response

[1] We use the Labview program
[2] This is done using a Matlab code applied to the extracted data
[3] In fact we will observe the DC peak at the center and the second peak that corresponds to the interference between the sample and the reference mirror

from the piezo, where we observe a maximum displacement around 66nm, and below 2V we don't have sufficient amplitude.

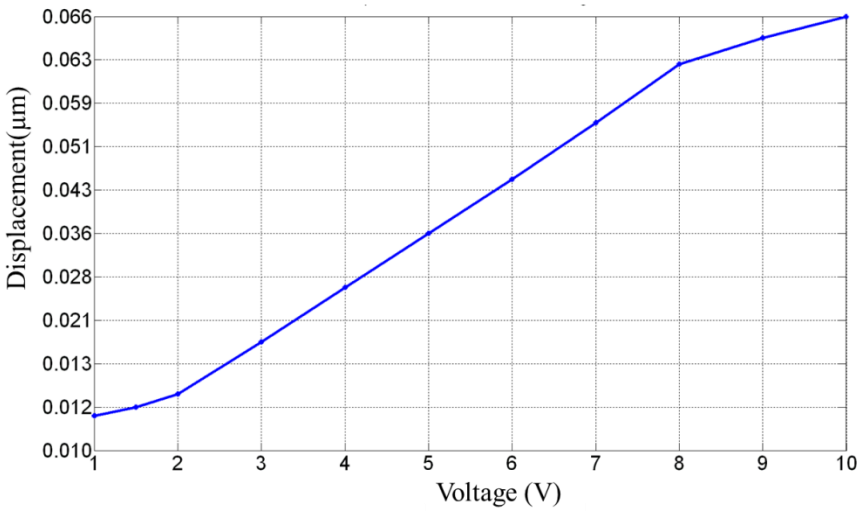

Figure 2-10 Displacement of the piezo versus voltage, the frequency was maintained at 12 kHz

2.3 Proof-of-concept experimental results

Our aim behind this setup is to validate the proof of concept of the subaxial resolution theory. So we have used the silicon wafer as the first layer and the mirror mounted on a piezo as the second layer. Then by approaching the two layers so that the distance between them becomes smaller than the coherence length of the broadband source, it will be no more possible to distinguish them in the spatial Fourier domain. Therefore by activating the piezo at given frequency we will get the axial profile as a function of time, and by using the method presented in section 1.4 we will be able to get the information about each layer.

We consider two cases:

- Large step displacement: The distance between two consecutive steps is larger than the half of the wavelength, so we cannot use the phase information. The amplitude is used in this case.
- Small step displacement: The distance between two consecutive steps is smaller of the half of the wavelength. The phase is used in this case.

2.3.1 Large step displacement

Using the sample formed by the silicon slice and the moving mirror, we now place the moving mirror close to the silicon sample at a distance smaller than the axial resolution of the source, see *Figure 2-11*. The moving mirror is oscillating continuously at 14 kHz frequency; its amplitude (peak to peak) is 63nm which has been set by applying an 8V peak to peak to the piezo. (We used the calibration curve to extract this value, see *Figure 2-10*).

We call large step a displacement between position 2 and position 1 in steps that are larger than half of the central wavelength estimated at 0.7525µm.

In order to extract the position of the hidden layer, we chose a step of 3µm. For each position we applied the method described in section 1.4 where we use the amplitude and not the phase since the step is larger than 0.7525µm, then by using a Matlab code we were able to separate the two layers numerically, see Appendix A.

Figure 2-12 shows the result obtained when applying the algorithm of reconstruction, to a situation where the distance between the two layers is within the coherence length. As we see, the maximum amplitude of the moving piezo is observed at the position 585 (in pixel unit), which corresponds to the position of the second layer which is undetectable in the spatial Fourier domain (depth profile z). In theory the form of the

reconstructed curve has to be Gaussian, but in our experiment, the reconstructed spectrum presents at some points, jumps which is probably due to the noise of our system. In fact we observed experimentally staircases (the same position) when taking steps smaller than the distance between two pixels in the spatial Fourier domain, which was estimated to be around 11.5µm[1], but if we take steps larger than 11.5µm, the staircase disappears and we will observe the red curve in *Figure 2-13*. Note that the axial resolution was estimated to be 76µm, see *Figure 2-3*. By applying our method we are able to go down to a resolution of 6µm which is approximately 13 times better than the static axial resolution.

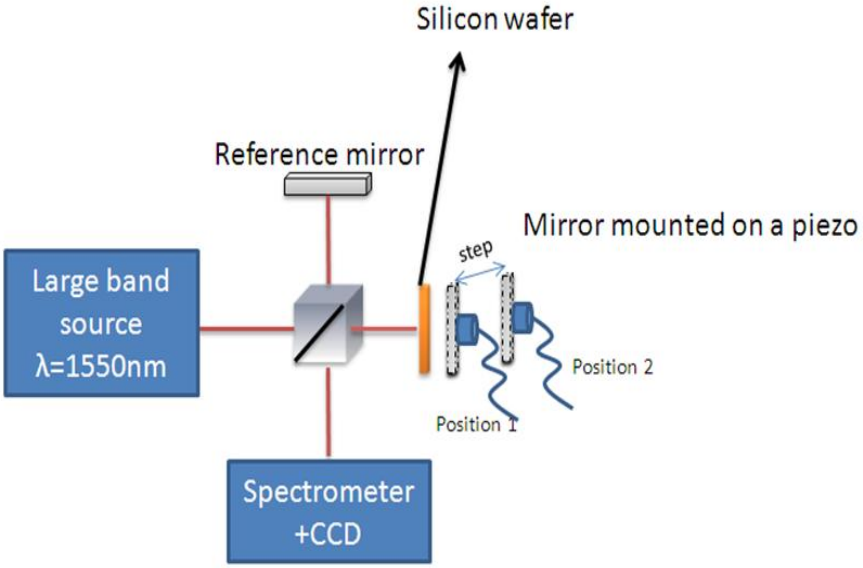

Figure 2-11 Experimental setup which shows the large steps. The system (piezo+mirror) is oscillating continuously at each position.

This method can potentially improve the axial resolution to a value equal of $\pm 6\mu m$ (the half of the distance between two pixels in the spatial

[1] $\Delta z = \pi \Big/ \left(\frac{2\pi}{\lambda_{min}} - \frac{2\pi}{\lambda_{max}}\right) = \frac{\pi}{\frac{2\pi}{1497.5} - \frac{2\pi}{1602.5}} = 11.5\mu m$

domain). This limitation cannot be avoided if we use the amplitude and not the phase, and it comes from the values of the minimal and the maximal wavelength of the spectrometer.

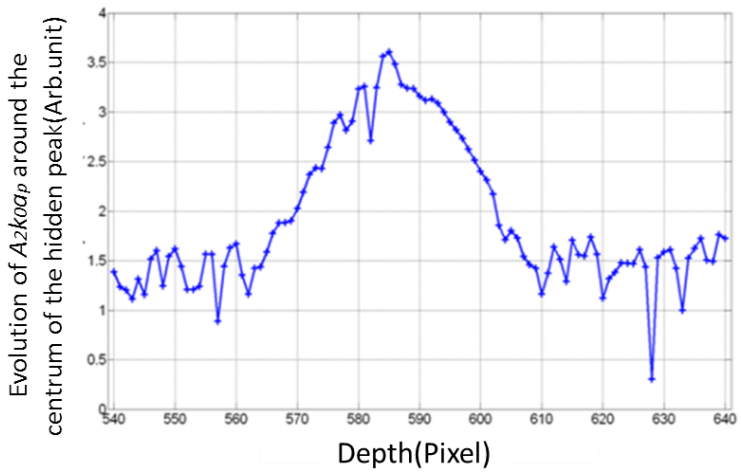

Figure 2-12 Illustration of how the reconstruction works; the maximum corresponds to the real position of the dynamic sample

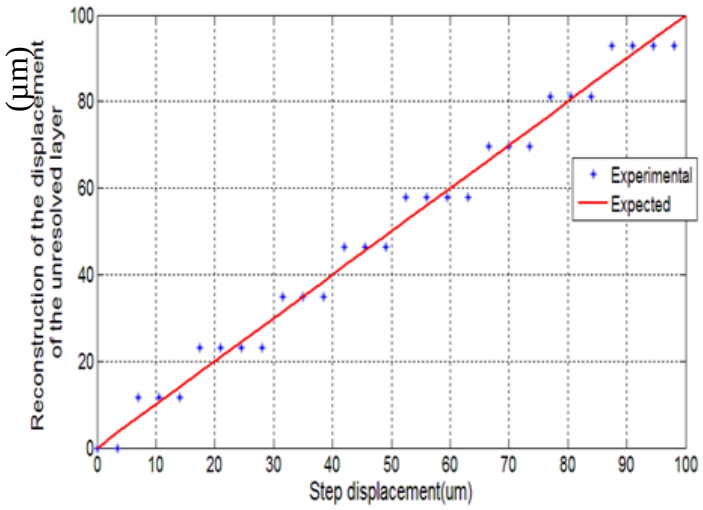

Figure 2-13 Reconstruction of the unresolved layer for many positions; the steps was 3µm which is larger than half of the wavelength, 0.7525µm

2.3.2 Small step displacement

Using the same setup, the moving mirror is oscillating at the same frequency 14 kHz, with amplitude of 63nm. We call small step a displacement in steps smaller than half of the central wavelength 0.7525µm.

We show in *Figure 2-14* the displacement of the moving mirror in real time using the phase, when we applied different small steps. Before each step we see a variation of the displacement, which is due to the fact that the piezo is oscillating, combined with the noise of our setup. Note that the true unwrapped phase is observed after a displacement of 0.7525µm.

Figure 2-15 illustrates the result of the reconstruction of the second layer at a different position; we took a step of 50nm which is lower than 0.7525µm. The red curve represents the theoretical result. The experimental data presented in blue fit correctly the expected result. The standard deviation between the measurement and the theoretical result is 65 nm.

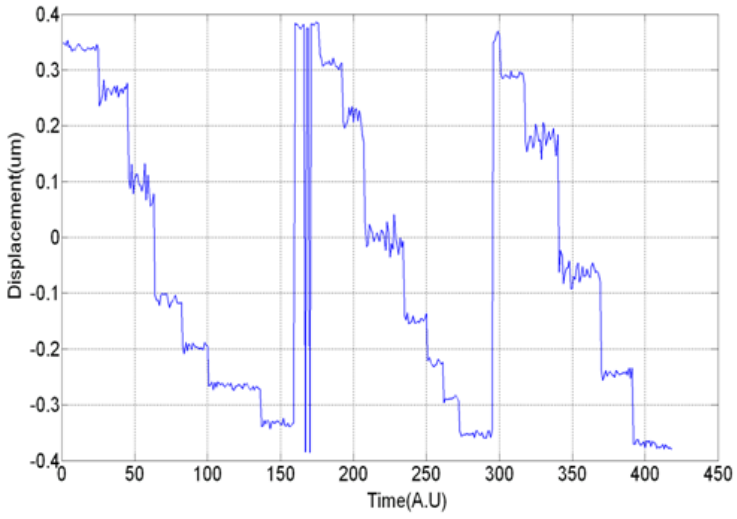

Figure 2-14 Phase shifting (displacement) versus time in real time, arbitrary step lower than half of the center wavelength, 0.7525µm

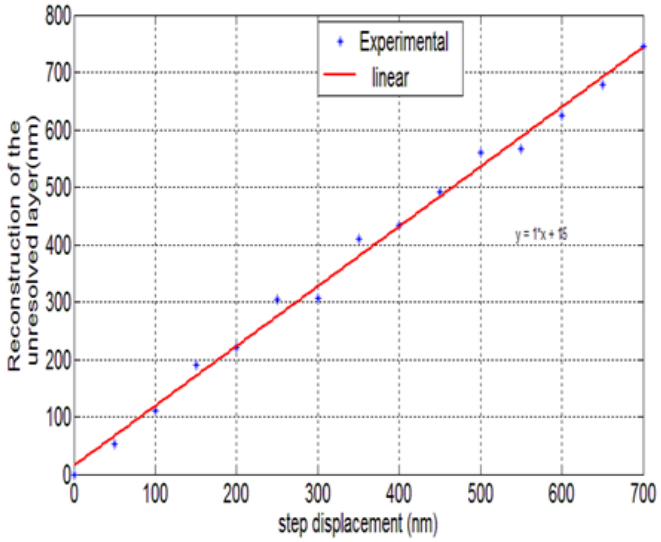

Figure 2-15 Reconstruction of the unresolved layer for many positions, the steps was 50nm which is smaller than half of the wavelength, 0.7525µm

2.4 Summary

We started this chapter by describing the FDOCT setup and its elements; we then characterized our setup by quantifying the experimental lateral resolutions, and the fall-off sensitivity. We then showed experimental results to validate the proof of concept. For large steps, we were able to reconstruct the position at a resolution of 6µm. For small steps, the resolution was 65nm.

Our IR FDOCT setup can perform also the tomography on a multilayer sample; this setup will then be used also in the second part. It will serve to compare the distance between two consecutive nodes of Fizeau fringes in both linear and nonlinear interferometry, and this will help to validate and calibrate the systems described in part II of this thesis.

Second part

Introduction

A difficulty often encountered in interferometric methods used for tomography like OCT, consists in the reflected waves at the interfaces ($z_1 \ldots z_{n-1}$) included in the signal, even if what interests us is the interface z_n. The sample is assumed to be n semi-reflective layers at the position $z_1 < z_2 \ldots < z_{n-1}$, each with a reflection coefficient for the field amplitude $\rho_1, \rho_2, \ldots \rho_n$.

The DC and the autocorrelation signal that come from these interfaces ($z_1 \ldots z_{n-1}$) contain no information about the desired interface z_n, they will reduce the sensitivity [15] and might contribute to saturate the detector.

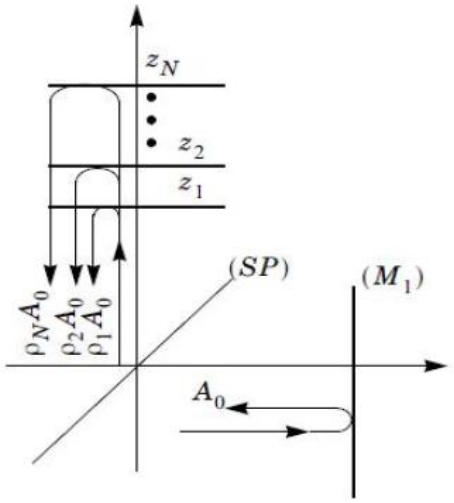

Figure 2-16 Schematic of multilayer sample in a Michelson interferometer

Many methods have been proposed to work around such problem. Wojtkowski and Leitgeb proposed algorithms that retrieve t he phase using multiple interferograms with known phase [17] or 90^o phase shift created by translating the reference mirror [18], to get complex signals which can eliminate the DC and the autocorrelation signal. But these algorithms need high stability systems and they decrease the imaging speed

due to the mechanical movement of the reference mirror. To improve this method, Sarunis *et al*. presented simultaneous access to non-complementary phase components of the complex interferometric signal using 3x3 fiber couplers [19], later Vakoc *et al*. demonstrated a method that employs polarization-based optical demodulation which allows the separation of signals from positive and negative depths to 50dB better in sensitivity [20], and not long ago a dual detection full range FDOCT was presented [21]. Alternatively, another techniques based on carrier frequency were proposed, Jun Zhang *et al*. proposed the enhancement of the signal to noise ratio by 20 dB in FDOCT using an electro optic phase modulator [22], they have used an appropriate carrier frequency that affects the signal but not the DC nor the autocorrelation term, so it is possible to separate the two terms in the final result.

Other OCT systems have been illustrated to improve the imaging capabilities, or to increase the contrast for specific applications. The polarization-sensitive OCT splits the polarization states of the detected interference to enhance the contrast in birefringence samples; it can measure the thickness of a birefringent retinal nerve fiber to diagnose glaucoma [23-24]. Another setup known as second harmonic OCT (SH-OCT) was reported, which combines the SHG nonlinear scatterings of a sample with the coherence gating of OCT to enhance the contrast of collagen [25-30].

We present in this part a novel method that can completely cancel out the DC and enhance the contrast using nonlinear optic gate. The strong sample reflection can be eliminated, and at the same time we can preserve the weaker sample reflection from sites of interest, leading to better image quality.

The nonlinear optic gate is a very popular phenomenon; it is very useful for femtosecond pulse characterization methods, like for example frequency-resolved optical gating (FROG) and second order autocorrelators

[31]. The superposition between the incident light beams for both methods generates a nonlinear signal only if the interaction in the nonlinear medium is perfectly synchronized to realize the temporal overlap of these intense pulses.

Nonlinear optic gating is widely useful in time-resolved imaging [32]. It works by filtering temporally the sample scattering light with a separate gating pulse in a non-linear medium. The time-resolved technique has been used to perform imaging through scattering media using different nonlinear phenomena [33-36].

The idea of our novel method is to mix in a nonlinear type II crystal, the laser beams from the two arms of the Michelson interferometer. By exploiting the polarization properties of the light, it is possible to make this frequency conversion efficient only to the superposition of the two beams from the reference arm and the one from the interface z_n. This can be done by realizing the optical contact, or in other words by setting the position of the reference mirror at equal distance from the beam splitter as the interface $z_{n,}$. Thus, the component of the converted signal comes only from the interference between the experimentally significant beams from the two arms of the interferometer. This allows us to isolate the useful signal component, which contains the tomographic information. Moreover, the frequency conversion permits recording the signal at a visible wavelength (650nm), while the sample is probed in the infrared (1300nm). From an experimental view, this is interesting because of the possibilities offered by sensitive detectors in the visible which exceed widely the most sensitive detectors in the infrared.

But the obtained signal contains no information about the phase because the pure type II SHG phenomenon excludes interferences; therefore we don’t observe any Michelson fringes between the reference arm and the sample arm. Nonlinear and linear fringes can be observed using the type II

SHG by turning the crystal around the light propagation axis. This will result in not eliminating completely the auto doubled signal from each arm (background noise); therefore it affects the contrast of the nonlinear fringe. The contrast can be controlled and it is a function of the rotation angle and the delay between the two arms of the interferometer.

A full description of the type II SHG phenomenon is presented, and then a detailed explanation of the theoretical model on how linear and nonlinear fringes can be obtained using second order autocorrelation interferometry, and what the parameters are that affect their contrast.

We demonstrate the dark field interferometry method in our setup; this method is based on creating fringes in the sample arm and setting the nonlinear crystal angle to zero to eliminate the undesired backscattered light. This method requires working with three waves coupling, this is why we used our FDOCT linear setup to calibrate and understand the nonlinear setup.

This part is divided into 3 chapters:

- In chapter 3 we explain the theory of the second harmonic generation; we give a full description on how to compute the effective nonlinear coefficient and the phase matching for the type II condition.

- In chapter 4 we give a novel theoretical demonstration for nonlinear interferometry using second order autocorrelation function. We illustrate using simulations for many considerations, the dependency of the fringes contrast and the DC on the angle between the ordinary or the extraordinary axis and the field's polarization at the entrance of the crystal. We conclude that in order to work with dark field background, no fringes can be observed. Therefore the necessity to create before doubling, fringes in test arm only.

- In the last chapter 5 we show the experimental setup to validate the theoretical study and the concept. We validate the dependence of nonlinear fringes on the angle and the delay between the two arms of the interferometer. Then later we switch to work in dark field where no Michelson fringes are observed, so we show the possibility to obtain fringes in black background using Fizeau fringes generated in the sample beam. We have used Fizeau fringes in our linear FDOCT and in our nonlinear setup to answer the question about the real distance between two consecutives fringes in the nonlinear setup (fundamental or second harmonic). We show a final application of a step measurement by doing nonlinear tomography with the suppression of the DC using Fizeau fringes, combined with femtosecond gate method.

3. Nonlinear optics theory for the type (II) SHG

In this chapter, we start by introducing the nonlinear optics, and then we explain the principle of type II SHG. We later present how to write and calculate the polarization components for the BBO case, and how to use the crystal orientations, the ordinary and the extraordinary axis. We then show how to calculate the nonlinear effective coefficient, and we finally end up by presenting the phase matching condition.

3.1 Overview

Nonlinear optics is an important field of optics that describes how atoms and molecules respond nonlinearly to an intense radiation field. I will explain in a few lines the difference between linear and nonlinear optics then I will switch back to nonlinear optics.

In a homogeneous medium, a monochromatic wave travels along a straight line. The propagation velocity of this wave is given by c / n, where n is the refractive index which depends on the arrangement of the atoms and the distribution of electrons in the medium. Whenever an electric field is applied to the medium, the distance that separates the electrons from the nucleus changes. If this field is oscillating (e.g. electromagnetic wave), the electrons of the medium will oscillate and will radiate another field proportional to the incident electric field; these two fields are phase shifted.

This phase shift is equivalent to a smaller propagation velocity. If the intensity of the incident beam is low, such that the electric field associated with the light beam is much smaller than the intra-atomic field, it can be shown that the phase shift is independent of the intensity of the light

beam. This is the case of the linear optics, and we enumerate some properties:

- Refractive index, absorption, refraction and transmission coefficient are independent of the incident light beam
- There is no change in frequency through the medium
- Superposition principle: harmonic waves will become independent and can be combined (their linear combinations satisfy the wave equation).

When the intensity of the electric field associated with the light wave becomes comparable to the intra-atomic electric field, the electrons distribution across the medium can be modified, this is the regime of nonlinear optics, and we enumerate some properties:

- A change in the refractive index
- The optical properties (refractive index, absorption, refraction…) depend on the magnitude of incident light
- The superposition principle is no more valid
- Changes in frequency (color) will operate through the nonlinear medium.

The first observation of the nonlinear effect was stated in 1961 when Franken observed the second harmonic generation in quartz [37], see *Figure 3-1*.

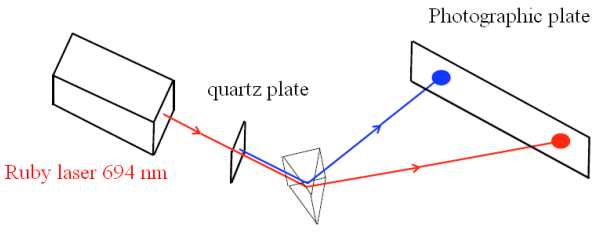

Figure 3-1 Experimental setup of Franken el al .

3.2 Polarization

The polarization is induced by an interaction between the light field and the medium, this polarization characterizes the response of the medium to the radiation excitation [38].

When the external light field intensity is sufficiently high in comparison with the intra-atomic electric field, the polarization can be written as a power series of the electric field [39]:

$$\vec{P}(t) = \varepsilon_0(\chi^{(1)}\vec{E}(t) + \chi^{(2)}\vec{E}^2(t) + \chi^{(3)}\vec{E}^3(t) + ...) \tag{3.1}$$

where ε_0 is the dielectric coefficient in vacuum, and $\chi^{(i)}$ is the tensor of the i^{th} order electric susceptibility. The components can be written:

$$P_i(t) = \varepsilon_0(\chi_{ij}^{(1)}E_j + \chi_{ijk}^{(2)}E_jE_k + \chi_{ijkl}^{(3)}E_jE_kE_l + ...) \tag{3.2}$$

In order to describe the nonlinear process, we must solve the wave propagation equation which results from the Maxwell's equations:

$$\Delta\vec{E} - \varepsilon_0\mu_0\frac{\partial^2\vec{E}}{\partial t^2} = \mu_0\frac{\partial^2\vec{P}}{\partial t^2} \tag{3.3}$$

In this inhomogeneous wave equation, the polarization $\vec{P}(t)$ produces an acceleration of the electrons which induces the emission of an electromagnetic wave field. Since $\vec{P}(t)$ contains nonlinear terms, by solving the equation above, we will be able to generate new frequencies.

Some examples of non-linear processes are shown in the next table:

Order	Tensor	Effects	Applications
1	$\chi^{(1)}$	Absorption, linear emission	Optical fiber
2	$\chi^{(2)}$	Second Harmonic Generation $2\omega;\omega,\omega$	Frequency doubling Electro-optic

		Pockels effect: $(-\omega;\omega,0)$	modulator
3	$\chi^{(3)}$	Third Harmonic Generation $3\omega;\omega,\omega,\omega$ Four-wave mixing $\omega_4;\omega_1,\omega_2,\omega_3$ Optical Kerr effect	Nonlinear spectroscopy Stimulated Raman effect Ultra-fast optical ports

3.3 Second Harmonic Generation (SHG)

Our research focuses mainly on the type II SHG phenomena; its principle is shown in *Figure 3-2*, which shows the underlying quantum process: two photons ω are absorbed and one photon 2ω is emitted. In other words,

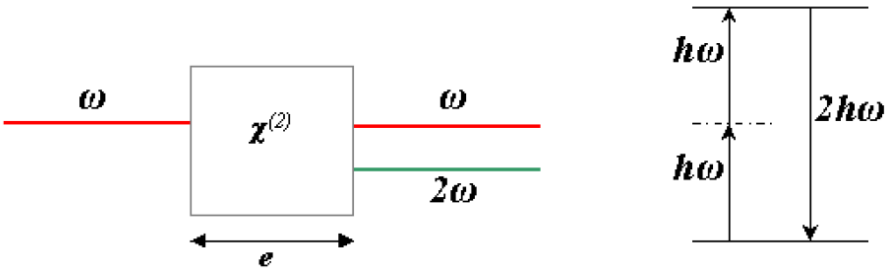

Figure 3-2 Second Harmonic Generation principle

If two orthogonal fields are applied to a type II nonlinear crystal, we will get a polarization at the doubled frequency, therefore we can write:

$$P_{NL}(2\omega) = \varepsilon_0 \chi_{ijk}^{(2)} E_1(\omega).E_2(\omega) \qquad (3.4)$$

where $\chi_{ijk}^{(2)}$ is the tensor of the second order electric susceptibility.

We define the nonlinear effective coefficient as d_{ijk} which can be calculated by: $d_{ijk} = \varepsilon_0 \chi_{ijk}^{(2)}$. The determination of the elements of the tensor d_{ijk} depends on the crystallographic structures of the materials. In centrosymmetric crystals d_{ijk}=0, and for crystals with noncentrosymmetric structures, d_{ijk} is a 3x3x3 tensor. This tensor can be reduced to a 6x3 matrix by considering *n=jk* which can take values between 1 and 6 [39]. In this case $d_{ijk} = d_{in}$, and we can write

$$n_{xx} = 1,\ n_{yy} = 2,\ n_{zz} = 3,\ n_{yz} = n_{zy} = 4,\ n_{xz} = n_{zx} = 5,\ n_{xy} = n_{yx} = 6$$

Therefore, d_{in} matrix becomes:

$$d_{in} = \begin{pmatrix} d_{11} & d_{12} & d_{13} & d_{14} & d_{15} & d_{16} \\ d_{21} & d_{22} & d_{23} & d_{24} & d_{25} & d_{26} \\ d_{31} & d_{32} & d_{33} & d_{34} & d_{35} & d_{36} \end{pmatrix}$$

Using this matrix, the polarization becomes:

$$\begin{pmatrix} P_x(2\omega) \\ P_y(2\omega) \\ P_z(2\omega) \end{pmatrix} =$$

$$\begin{pmatrix} d_{11} & d_{12} & d_{13} & d_{14} & d_{15} & d_{16} \\ d_{21} & d_{22} & d_{23} & d_{24} & d_{25} & d_{26} \\ d_{31} & d_{32} & d_{33} & d_{34} & d_{35} & d_{36} \end{pmatrix} \times \begin{pmatrix} E_{1x}(\omega)E_{2x}(\omega) \\ E_{1y}(\omega)E_{2y}(\omega) \\ E_{1z}(\omega)E_{2z}(\omega) \\ E_{1y}(\omega)E_{2z}(\omega) + E_{1z}(\omega)E_{2y}(\omega) \\ E_{1z}(\omega)E_{2x}(\omega) + E_{1x}(\omega)E_{2z}(\omega) \\ E_{1x}(\omega)E_{2y}(\omega) + E_{1y}(\omega)E_{2x}(\omega) \end{pmatrix} \quad (3.5)$$

If we develop the matrix product, the polarization components become:

$$P_x = d_{11}(E_{1x}E_{2x}) + d_{12}(E_{1y}E_{2y}) + d_{13}(E_{1z}E_{2z}) + d_{14}(E_{1y}E_{2z} + E_{1z}E_{2y}) + d_{15}(E_{1z}E_{2x} + E_{1x}E_{2z}) + d_{16}(E_{1x}E_{2y} + E_{1y}E_{2x})$$

(3.6)

$$P_y = d_{21}(E_{1x}E_{2x}) + d_{22}(E_{1y}E_{2y}) + d_{23}(E_{1z}E_{2z}) + d_{24}(E_{1y}E_{2z} + E_{1z}E_{2y}) + d_{25}(E_{1z}E_{2x} + E_{1x}E_{2z}) + d_{26}(E_{1x}E_{2y} + E_{1y}E_{2x})$$

(3.7)

$$P_z = d_{31}(E_{1x}E_{2x}) + d_{32}(E_{1y}E_{2y}) + d_{33}(E_{1z}E_{2z}) + d_{34}(E_{1y}E_{2z} + E_{1z}E_{2y}) + d_{35}(E_{1z}E_{2x} + E_{1x}E_{2z}) + d_{36}(E_{1x}E_{2y} + E_{1y}E_{2x})$$

(3.8)

In our work we used a BBO crystal with point group 3m-C_{3c} which has the following d_{in} tensor [39]:

$$d_{in} = \begin{pmatrix} 0 & 0 & 0 & 0 & d_{15} & -d_{22} \\ -d_{22} & d_{22} & 0 & d_{15} & 0 & 0 \\ d_{31} & d_{31} & d_{32} & 0 & 0 & 0 \end{pmatrix} \quad (3.9)$$

In this case we can deduce that

$$d_{11} = d_{12} = d_{13} = d_{14} = d_{23} = d_{25} = d_{26} = d_{34} = d_{35} = d_{30} = 0$$

And the non-vanishing coefficients are:

$$d_{15},\ d_{16},\ d_{21},\ d_{22},\ d_{24},\ d_{31},\ d_{32},\ d_{33}$$

The relationship between the coefficients is:

$$d_{16} = -d_{22}\ ,\ d_{21} = -d_{22}\ ,\ d_{24} = -d_{15}$$

Therefore the polarization components in this case become:

$$P_x = d_{15}(E_{1z}E_{2x} + E_{1x}E_{2z}) - d_{22}(E_{1x}E_{2y} + E_{1y}E_{2x}) \quad (3.10)$$

$$P_y = -d_{22}\left(E_{1x}E_{2x}\right) + d_{22}\left(E_{1y}E_{2y}\right) + d_{15}(E_{1y}E_{2z} + E_{1z}E_{2y}) \quad (3.11)$$

$$P_z = d_{31}\left(E_{1x}E_{2x}\right) + d_{31}\left(E_{1y}E_{2y}\right) + d_{33}(E_{1z}E_{2z}) \quad (3.12)$$

3.4 Uniaxial crystals and index ellipsoid

In an anisotropic crystal the applied electric field and the polarization direction have different directions. The displacement field can be written as a function of the external field:

$$\begin{pmatrix} D_x = \varepsilon_{11}E_x + \varepsilon_{12}E_y + \varepsilon_{13}E_z \\ D_y = \varepsilon_{21}E_x + \varepsilon_{22}E_y + \varepsilon_{23}E_z \\ D_z = \varepsilon_{31}E_x + \varepsilon_{32}E_y + \varepsilon_{33}E_z \end{pmatrix} \quad (3.13)$$

Where $\varepsilon_{ij} = \varepsilon_0(1+\chi_{ij})$ is the dielectric permeability tensor, χ_{ij} is the electric susceptibility described previously. We can write:

$$D_i = \varepsilon_{ij}E_j \quad (3.14)$$

i, j can take the values 1,2 and 3 and they stand for *x=1,y=2 and z=3.* The energy density is defined by:

$$U = \frac{1}{2}ED = \frac{1}{2}E_i\varepsilon_{ij}E_j \quad (3.15)$$

In the principal coordinate system ε_{ij} [39]:

$$\varepsilon_{ij} = \begin{pmatrix} \varepsilon_{11} & 0 & 0 \\ 0 & \varepsilon_{22} & 0 \\ 0 & 0 & \varepsilon_{33} \end{pmatrix} = \begin{pmatrix} \varepsilon_x & 0 & 0 \\ 0 & \varepsilon_y & 0 \\ 0 & 0 & \varepsilon_z \end{pmatrix} \quad (3.16)$$

Therefore we can write:

$$2U = ED = E_i \varepsilon_{ij} E_j = E_x \varepsilon_x E_x + E_y \varepsilon_y E_y + E_z \varepsilon_z E_z$$

And by replacing E_i with $D_i / \varepsilon_i \Rightarrow$

$$2U = \frac{D_x^2}{\varepsilon_x} + \frac{D_y^2}{\varepsilon_y} + \frac{D_z^2}{\varepsilon_z} \tag{3.17}$$

Nonlinear crystals are nonmagnetic materials[1]

$$\varepsilon_x = n_x^2, \varepsilon_y = n_y^2, \varepsilon_z = n_z^2 \tag{3.18}$$

n_x, n_y and n_z are the principal refraction index, we define the principal axis *x*, *y* and *z*:

$$x^2 = \frac{D_x^2}{2U}, y^2 = \frac{D_y^2}{2U}, z^2 = \frac{D_z^2}{2U} \tag{3.19}$$

Using (3.17) we get:

$$\frac{x^2}{n_x^2} + \frac{y^2}{n_y^2} + \frac{z^2}{n_z^2} = 1 \tag{3.20}$$

This relation is called the index ellipsoid equation.

Since we work with a BBO crystal, we jump directly to uniaxial crystals where there is no difference between n_x and n_y, it is called the ordinary refractive index and we write:

$$n_o = n_x = n_y \tag{3.21}$$

n_z is called the extraordinary index of refraction, we have:

$$n_e = n_z \tag{3.22}$$

In the BBO case, $n_o > n_e$ this is what we call negative biaxial crystal.

[1] $n = \sqrt{\varepsilon_r \mu_r}$, for nonmagnetic material $\mu_r = 1$

We show in *Figure 3-3* the electric field for ordinary and extraordinary waves in uniaxial crystals. Note that the extraordinary index is function of θ; on the other hand the ordinary one is constant. Using the ellipsoid equation described in (3.20) we can write [40]:

$$\frac{1}{n_e^2(\omega,\theta)} = \frac{\cos^2(\theta)}{n_o^2(\omega)} + \frac{\sin^2(\theta)}{n_e^2(\omega)} \tag{3.23}$$

For the BBO, Sellmeier relations for n_o and n_e as a function of λ (µm)[1] are:

$$\begin{aligned} n_e^2 &= 2.3753 + \frac{0.01224}{\lambda^2 - 0.01667} - 0.01516\lambda^2 \\ n_o^2 &= 2.7359 + \frac{0.01878}{\lambda^2 - 0.01822} - 0.01354\lambda^2 \end{aligned} \tag{3.24}$$

Both depend on the temperature in the case of BBO, the relations:

$$\frac{dn_o(\lambda)}{dT} = \frac{-16,6.10^{-6}}{C^\circ} \quad and \quad \frac{dn_e(\lambda)}{dT} = \frac{-9,3.10^{-6}}{C^\circ} \tag{3.25}$$

We see clearly that n_o is larger than n_e (negative uniaxial crystal)

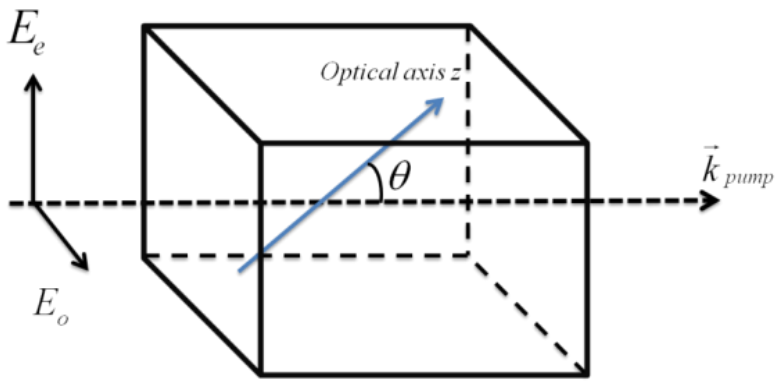

Figure 3-3 An uniaxial birefringent crystal. The principal plane of the crystal is the plane of the wave vector k and the optical axis of the crystal. An ordinary polarized wave has a polarization perpendicular to this plane and an extraordinary polarized wave has polarization in the principal plane.

[1] http://www.optical-components.com/BBO-crystal.html

3.5 The effective nonlinear coefficient

The calculation of this coefficient is made to understand what are the hypothesis and the parameters, that affect this coefficient, and to relate these to our goal to understand the effect of rotating the crystal on the contrast of the nonlinear fringes.

We start by looking at the expression of the polarization which is quite complex, if we take for example the equations (3.10) , (3.11) and (3.12), it contains a lot of summation which involve the nonzero matrix elements and the polarization components of the interacting waves. These complex equations can be simplified into a new expression:

$$P = d_{eff} E(\omega_1) E(\omega_2) \tag{3.26}$$

where d_{eff} contains all the summation that has been done for a defined crystal.

So by considering the BBO type II crystal for the second harmonic generation, we have two linearly polarized plane waves with amplitudes E^o and E^e propagating in a BBO crystal at an angle θ_m to the optical axis. We consider also that the plane formed by the optical axis and the e-ray (E^e) field makes an angle φ with the x axis, and the o-ray (E^o) is perpendicular to the e-ray. In the next paragraph we will calculate the nonlinear second order polarization for the BBO crystal type II coupling.

Figure 3-4 shows the direction of the electric fields in negative uniaxial crystals (ordinary and extraordinary waves). We can write the components of each field, we get:

$$Ordinary\begin{cases} E_x^o(\omega) = E^o(\omega).\sin(\varphi) \\ E_y^o(\omega) = -E^o(\omega).\cos(\varphi) \\ E_z^o(\omega) = 0 \end{cases} \quad (3.27)$$

$$Extraordinary\begin{cases} E_x^e(\omega) = -E^e(\omega).\cos(\theta_m)\cos(\varphi) \\ E_y^e(\omega) = -E^e(\omega).\cos(\theta_m)\sin(\varphi) \\ E_z^e(\omega) = \sin(\theta_m) \end{cases} \quad (3.28)$$

Under the phase matching condition which will be explained later, the BBO type II crystal will allow only the coupling of an ordinary wave with an extraordinary wave. Using the three components of the polarization described in equations(3.10), (3.11) and(3.12), and by considering that the field 1 is E^o and the field 2 is E^e we obtain:

$$P_x = d_{15}E^oE^e\sin\varphi\sin\theta_m + d_{22}E^oE^e(\cos\theta_m\sin^2\varphi - \cos\theta_m\cos^2\varphi) \quad (3.29)$$

$$P_y = d_{22}E^oE^e(\cos\theta_m\cos\varphi\sin\varphi + \cos\theta_m\cos\varphi\sin\varphi) - d_{15}E^oE^e\cos\varphi\sin\theta_m \quad (3.30)$$

$$P_z = d_{31}E^oE^e(-\sin\varphi\cos\theta_m\cos\varphi + \sin\varphi\cos\theta_m\cos\varphi) = 0 \quad (3.31)$$

If we rewrite the polarization components with respect to the ordinary and the extraordinary axis we get:

$$P^o = P_x\sin\varphi - P_y\cos\varphi \quad (3.32)$$

$$P^e = P_z\sin\theta_m - (P_x\cos\varphi + P_y\sin\varphi)\cos\theta_m \quad (3.33)$$

By substituting (3.29), (3.30), and (3.31) into (3.32) and (3.33) we obtain:

$$P^o = d_{15}E^oE^e(\sin^2\varphi\sin\theta_m + \sin\theta_m\cos^2\varphi) + d_{22}E^oE^e(\cos\theta_m\sin^3\varphi - 3\cos\theta_m\cos^2\varphi\sin\varphi) \quad (3.34)$$

$$P^o = (d_{15}\sin\theta_m - d_{22}\cos\theta_m\sin 3\varphi)E^oE^e \quad (3.35)$$

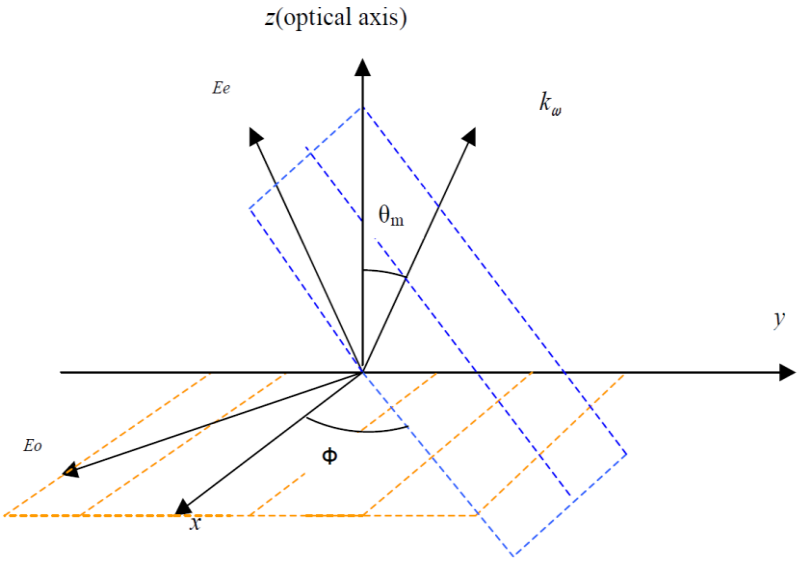

Figure 3-4 The ordinary and extraordinary electric fields in uniaxial crystals. x,y and Eo are in the orange plane, kω, z and Ee are in the blue plane

And:

$$P^e = -d_{15}E^oE^e\left(\sin\varphi\sin\theta_m\cos\varphi - \cos\varphi\sin\theta_m\sin\varphi\right)\cos\theta_m + d_{22}E^oE^e\left(3\cos\theta_m\cos\varphi\sin^2\varphi - \cos\theta_m\cos^3\varphi\right)\cos\theta_m \quad (3.36)$$

$$P^e = d_{22}E^oE^e\cos^2\theta_m\cos 3\varphi \quad (3.37)$$

Using the definition of the d_{eff} described in (3.26), the effective nonlinear coefficient for type II phase matching comes directly from (3.35) and (3.37):

Mode: $o + e \rightarrow e$

$$d_{eff} = d_{22}\cos^2(\theta_m)\cos(3\varphi) \quad (3.38)$$

Mode: $o + e \rightarrow o$

$$d_{eff} = d_{15}\sin(\theta_m) - d_{22}\cos(\theta_m)\sin(3\varphi) \tag{3.39}$$

These two expressions already exist in the literature [41]. We conclude that if we rotate the crystal around the wave direction k_{pump} (see *Figure 3-3*), the nonlinear effective coefficient will not be affected. It depends only on the two angles:

- θ the angle between the optical axis and the k_{pump}
- φ the angle between the plane (formed by the extraordinary wave and the optical axis), and the x axis.

3.6 Phase matching

There are two types of phase matching, type I and II.

Type I is the type of phase matching in which two waves with the same polarization generate a new wave of different frequency, see *Figure 3-5* (a). In type II, we combine two waves with orthogonal polarizations; see *Figure 3-5*(b). In the type I, the polarization is oriented along z and given by:

$$P(z) = d_{eff}E_1(z)E_2(z)e^{i\Delta kz} \tag{3.40}$$

Where $\Delta k = k_3 - k_1 - k_2$

The phase matching condition for type I is

$$\Delta k = 0 \Rightarrow k_3 = k_1 + k_2 \Rightarrow n_3\omega_3 = n_1\omega_1 + n_2\omega_2 \tag{3.41}$$

In the type II, the polarization is given by:

$$P_3(\vec{r}) = d_{eff}E_1(\vec{r})E_2(\vec{r})e^{i\Delta\vec{k}.\vec{r}} \tag{3.42}$$

Where $\Delta\vec{k} = \overrightarrow{k_3} - \overrightarrow{k_1} - \overrightarrow{k_2}$

The phase matching condition for type II:

$$\Delta\vec{k} = \vec{0} \Rightarrow \overrightarrow{k_3} = \overrightarrow{k_1} + \overrightarrow{k_2} \Rightarrow n_3\omega_3\overrightarrow{u_3} = n_1\omega_1\overrightarrow{u_1} + n_2\omega_2\overrightarrow{u_2} \qquad (3.43)$$

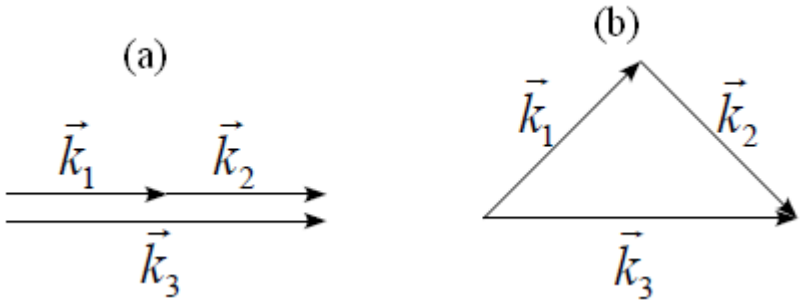

Figure 3-5 Phase matching, (a) type I-(b) type II

3.6.1 Type II phase matching $o+e \xrightarrow{SHG} e$

We are interested in the phase matching for the type (II) BBO, where we have the coupling of two polarizations to the ordinary and the extraordinary axis. The output generated is oriented in this case along the extraordinary axis ($o+e \rightarrow e$), we recall the phase matching condition [40]:

$$n_e(2\omega,\theta_m) = \frac{1}{2}\left[n_e^{\omega}(\omega,\theta_m) + n_o(\omega)\right] \qquad (3.44)$$

Using equation (3.23) we can write

$$\begin{aligned} \frac{1}{n_e^2(2\omega,\theta_m)} &= \frac{\cos^2(\theta_m)}{n_o^2(2\omega)} + \frac{\sin^2(\theta_m)}{n_e^2(2\omega)}; \\ \frac{1}{n_e^2(\omega,\theta_m)} &= \frac{\cos^2(\theta_m)}{n_o^2(\omega)} + \frac{\sin^2(\theta_m)}{n_e^2(\omega)} \end{aligned} \qquad (3.45)$$

Combining equation (3.44) and (3.45) we get:

$$\left(\frac{\cos^2(\theta_m)}{n_o^2(2\omega)}+\frac{\sin^2(\theta_m)}{n_e^2(2\omega)}\right)^{-1/2}=\frac{1}{2}\left[n_o(\omega)+\left(\frac{\cos^2(\theta_m)}{n_o^2(\omega)}+\frac{\sin^2(\theta_m)}{n_e^2(\omega)}\right)^{-1/2}\right]$$

(3.46)

There is no analytical expression for the angle θ, only a numerical solution can be found using this relation.

3.6.2 Type II phase matching $o+e \xrightarrow{SHG} o$

The polarization at the output of the crystal is oriented with respect to the ordinary axis. In this case the phase matching condition is :

$$n_o(2\omega)=\frac{1}{2}\left[n_e^{\omega}(\theta_m)+n_o(\omega)\right] \tag{3.47}$$

Using equation (3.45) we get

$$2n_o(2\omega)-n_o(\omega)=n_e(\omega,\theta_m)=\left(\frac{\cos^2(\theta_m)}{n_o^2(\omega)}+\frac{\sin^2(\theta_m)}{n_e^2(\omega)}\right)^{-1/2} \tag{3.48}$$

The solution is

$$\sin^2(\theta_m)=\frac{\dfrac{n_o^2(\omega)}{\left(2n_o(2\omega)-n_o(\omega)\right)^2}-1}{\dfrac{n_o^2(\omega)}{n_e^2(\omega)}-1} \tag{3.49}$$

3.7 Summary

We introduced the nonlinear optic by comparing its property to the linear optic. Then we explained the Second Harmonic Generation phenomena and we illustrated the expression of the components of the polarization in this case. We later showed for the type II coupling using the

BBO crystal how to calculate the nonlinear effective coefficient; this coefficient does not depend on the rotational angle of the crystal around the wave direction. We finally discussed the phase matching condition for the two possibilities in the type II.

4. Nonlinear interferometry-Theory and simulation

In this chapter, we first introduce the autocorrelation technique and we explain its use for pulse characterization [42-44]. Then we show that it is possible to create nonlinear fringes using the second order autocorrelation interferometry technique. Measurements with nonlinear fringes were already presented in the literature, for example *Santran et.al* determined the nonlinear refractive index of photo-thermo refractive glass using collinear-orthogonal-polarization-pump-probe (COP3)[45]. By measuring the signal at the doubled frequency (nonlinear term) they estimated the refractive index n_2. *Diels et.al* used the interferometric second order autocorrelations to control and measure ultrashort pulse shapes (amplitude and phase) [46]. We describe in this chapter the orthogonal polarization second order interferometry for shape and displacement measurements; we give new analytical expression for the autocorrelation function for different situations, such as unbalanced return fields, balanced return fields, dispersion in one arm, asymmetry of the envelope and the mix between these previous case.

Then we analyze using simulations the dependency between the crystal angle and the contrast of the fringes. We later discuss the different parameters that affect the contrast of both linear and nonlinear fringes, such as the delay, the balancing coefficient of the return fields, the group velocity dispersion and the degree of asymmetry of the pulse envelope.

4.1 Introduction to the autocorrelation technique for fast pulses characterization

A photo-detector cannot have access to the temporal profile of a femtosecond pulse; it can only detect the energy. The time response of the

detector is always much longer than the pulse duration, for this reason another method is required to determine the substructure of the pulses (arrival time and phase), in order to reconstruct completely *E (t)*.

The basic method consists of measuring the autocorrelation-function of the pulse, which can be acquired using a Michelson interferometer (see *Figure 4-1*).

A 0.1 μm displacement of the moving mirror produces a temporal displacement of 0.33fs (0.67fs if we consider the round trip in the Michelson interferometer).

At the first order autocorrelation, the detected intensity is given by:

$$I_1(\tau) = \int_{-\infty}^{+\infty} \left(E_t + E_{t-\tau}\right)\left(E_t + E_{t-\tau}\right)^* dt \qquad (4.1)$$

where *E (t)* is the complex electric field emitted by the laser, and τ is the time delay between the two arms of the interferometer.

We see that the domain of the integral is $\pm\infty$ because in the case of femtosecond phenomena the time response of the detector is much slower (*μs- ns*), allowing extension of the integration to infinity. By developing (4.1) we obtain:

$$\begin{aligned} I_1(\tau) &= 2\int_{-\infty}^{+\infty} I_t\, dt + 2\int_{-\infty}^{+\infty} E_{t-\tau}\, \overset{*}{E}_t\, dt \\ &= 2\int_{-\infty}^{+\infty} I_t\, dt + 2G_1(\tau) \end{aligned} \qquad (4.2)$$

where $G_1(\tau)$ is the first order autocorrelation as a function of the field. By using the Fourier transform of this function we get the spectral power distribution (spectral intensity):

$$\mathbb{F}\left[G_1(\tau)\right] = \left|E(\omega)\right|^2 \qquad (4.3)$$

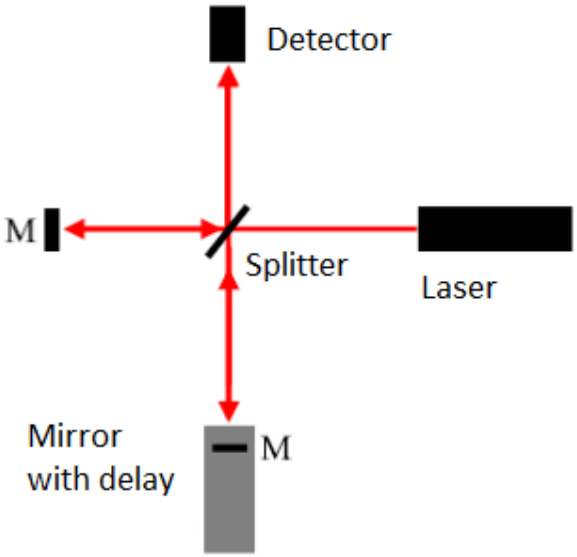

Figure 4-1 Michelson interferometer with delay

But this is not enough to determine the pulse duration. Knowing the width of the spectral intensity will only give a minimum limit of the pulse duration Δt :

$$\Delta t.\Delta\omega \geq K \qquad (4.4)$$

where the value of K depends on the shape of the envelope [47-48] (see *Table 1*).

Note that the minimum of this inequality is reached when the spectral phase of the pulse is constant. An example of a first order autocorrelation signal is presented in *Figure* 4-2.

Shape	$E(t)$	K
Gaussian	$\exp\left\{-\left(\frac{t}{t_0}\right)^2 \Big/ 2\right\}$	0.441
Exponential	$\exp\left\{-\frac{\lvert t\rvert}{t_0} \Big/ 2\right\}$	0.142
Hyperbolic	$1 \Big/ \cosh\left(t \Big/ t_0\right)$	0.315
Square	$rect\left(\frac{t}{t_0}\right)$	0.886
Cardinal Sinus	$\frac{\sin^2\left(t/t_0\right)}{\left(t/t_0\right)^2}$	0.374
Lorentzian	$\left[1+\left(\frac{t}{t_0}\right)^2\right]^{-1}$	0.142

Table 1different values of K for different pulse shapes. t_0 represents a fixed duration parameter. Criterion of full width at half maximum has been employed

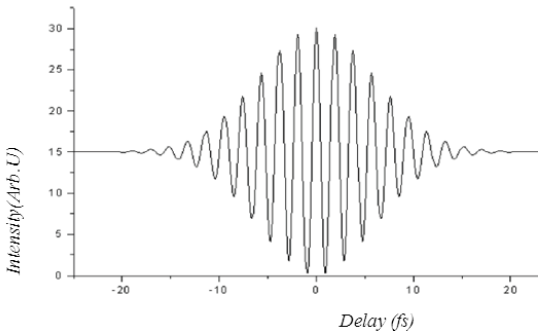

Figure 4-2 First order autocorrelation signal

The interferometric signal detected by the photodiode can have a resolution of the order of femtosecond; therefore we are able to have indirect observation of the ultrafast phenomena.

In order to characterize completely the pulse, we need to have access to all the other orders of the autocorrelation signal $G_n(\tau)$. At the second

order, it is the square of the field that is autocorrelated and then detected as intensity. We distinguish two types: Collinear polarization autocorrelation (type I) and non collinear polarization autocorrelation (orthogonal polarization type II). To obtain the second order for both methods we can use the second harmonic generation; the induced polarization can then be written:

Collinear Polarization

$$P(2\omega) = d_{eff} E_s^2 \qquad (4.5)$$

Orthogonal Polarization

$$P(2\omega) = d_{eff} E_o E_e \qquad (4.6)$$

Where E_s is the total electric field in the case of collinear polarization, in this case a nonlinear type I crystal is used. E_o, E_e are the two orthogonal fields with respect to the ordinary and the extraordinary axis, in this case a nonlinear type II crystal is used.

In the next paragraph I will explain briefly the second order autocorrelation with collinear polarization, and then I will switch to the crossed orthogonal polarization which is our main study to generate nonlinear fringes.

Figure 4-3 illustrates the experimental scheme of the collinear polarization autocorrelation. The input pulse is divided through a beam splitter into two fields where one of them is progressively delayed. The recombined field from the two arms is then focused into a type I nonlinear crystal where SHG will take place, therefore we get a field proportional to $\left[E_t + E_{t-\tau}\right]^2$ and then a photodiode will detect the intensity at the doubled frequency. We write the intensity as:

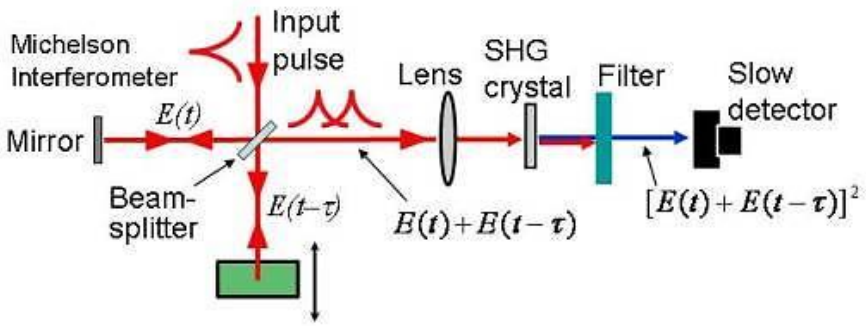

Figure 4-3Experimental layout for collinear autocorrelation

$$I_2(\tau) \propto \int_{-\infty}^{+\infty} \left| \left(E_t + E_{t-\tau} \right)^2 \right|^2 dt \qquad (4.7)$$

Let's assume that the complex field can be written as follows, described by an amplitude A_t and a phase φ:

$$E_t = A_t e^{j(\omega t+\varphi)} \qquad (4.8)$$

By developing $I_2(\tau)$ we get:

$$I_2(\tau) \propto \int_{-\infty}^{+\infty} \left| \left(A_t e^{j(\omega t+\varphi)} + A_{t-\tau} e^{j(\omega(t-\tau)+\varphi)} \right)^2 \right|^2 dt$$

$$I_2(\tau) \propto \int_{-\infty}^{+\infty} \begin{bmatrix} A_t^4 + A_{t-\tau}^4 & "Pedestal" \\ +4A_t^2 A_{t-\tau}^2 & "Envelope" \\ +4A_t A_{t-\tau}\left(A_t^2 + A_{t-\tau}^2\right)\cos(\omega\tau) & "Linear\ fringe" \\ +2A_t^2 A_{t-\tau}^2 \cos(2\omega\tau) & "Nonlinear\ fringe" \end{bmatrix} dt$$

(4.9)

We can divide this expression into two parts: the interferometric part, which contains a coherence term oscillating at ω (linear fringes), and a coherence term oscillating at 2ω (nonlinear fringes), and the non

interferometric part (background) which is determined by the pedestal and the envelope.

If $\tau \to 0$ we obtain the maximum intensity:

$$Max = 16\int_{-\infty}^{+\infty} A_t^4 dt$$

If $\tau \to \infty$ we obtain the minimum intensity:

$$Min = 2\int_{-\infty}^{+\infty} A_t^4 dt$$

The contrast of the collinear second order autocorrelation is therefore 8:1. This form is quite general; it is used to ensure the proper functioning of a second order autocorrelator.

To determine the duration of the pulse through the interferometric second order autocorrelation signal, we can apply a low-pass frequency filter to remove the interferometric part. The filtered signal is called the **second order autocorrelation intensity signal.**

4.2 Crossed orthogonal polarization autocorrelation

We present in this section the interferometric method to generate nonlinear fringes in an original manner. The reason we want to generate fringes is to have access to the phase information and to be able to make tomographic measurements to characterize samples like MEMS.

The theoretical model is demonstrated and explained in details. New analytical expressions are presented for the first time. These analytical expressions combined with simulations will serve to analyze the contrast of the fringes and identify the parameters that can be used to control it.

4.2.1 Theoretical demonstration of linear and nonlinear fringes in the case of orthogonal polarizations

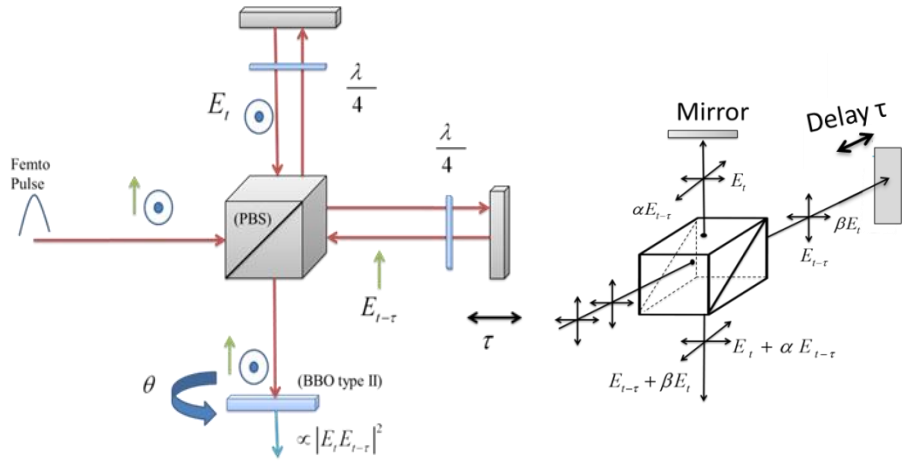

Figure 4-4 crossed orthogonally polarized autocorrelationdiagram

Figure 4-4 shows the setup for the crossed orthogonal polarized autocorrelation. We combine two orthogonal fields in a classic interferometer with a polarizing beam splitter (PBS). The PBS will separate the two orthogonal polarizations so that each polarization will probe an arm of the interferometer. At the output of the nonlinear crystal we get a field proportional to the product of these orthogonal fields, see equation(4.6). Knowing that the photodiode will then detect the energy, therefore we get the second order autocorrelation function as:

$$G(\tau) \propto d_{eff} \int_{-\infty}^{+\infty} \left| E_o E_e \right|^2 dt \qquad (4.10)$$

In order to observe fringes in this case, we need to rotate the crystal around the axis which corresponds to the direction of the laser; this will be explained hereunder.

If we turn the crystal around the laser propagating axis, we have to rewrite the components of the field with respect to the ordinary (o) and the extraordinary (e) axis, because the type II crystal allows only the coupling of an ordinary wave and extraordinary wave that arrive synchronously on the crystal, so we get:

$$E_0 = E_t cos\theta + E_{t-\tau} sin\theta$$
$$E_e = E_t sin\theta - E_{t-\tau} cos\theta \qquad (4.11)$$

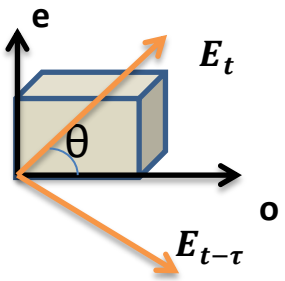

By injecting E_o and E_e in the equation (4.10) we obtain $G(\tau)$

$$\propto d_{eff} \int_{-\infty}^{+\infty} \left|E_o E_e\right|^2 dt \propto d_{eff} \int_{-\infty}^{+\infty} \left|(E_t cos\theta + E_{t-\tau} sin\theta)(E_t sin\theta - E_{t-\tau} cos\theta)\right|^2 dt$$

$$\propto d_{eff} \int_{-\infty}^{+\infty} \left| E_t^2 \cos\theta \sin\theta - E_t E_{t-\tau} \cos^2\theta + E_t E_{t-\tau} \sin^2\theta - E_{t-\tau}^2 \sin\theta \cos\theta \right|^2 dt$$

$$\propto \frac{d_{eff}}{2} \int_{-\infty}^{+\infty} \left| E_t^2 \sin 2\theta - E_{t-\tau}^2 \sin 2\theta - E_t E_{t-\tau} \cos^2\theta \right|^2 dt$$

$$\propto \frac{d_{eff}}{2} \int_{-\infty}^{+\infty} \left(E_t^2 \sin 2\theta - E_{t-\tau}^2 \sin 2\theta - E_t E_{t-\tau} \cos^2\theta \right) \begin{pmatrix} E_t^{*2} \sin 2\theta - E_{t-\tau}^{*2} \sin 2\theta \\ - E_t^{*} E_{t-\tau}^{*} \cos^2\theta \end{pmatrix} dt$$

$$\propto \frac{d_{eff}}{2} \int_{-\infty}^{+\infty} \begin{pmatrix} \left|E_t\right|^4 \sin^2 2\theta - E_t^2 E_{t-\tau}^{*2} \sin^2 2\theta - 2\left|E_t\right|^2 E_t E_{t-\tau}^{*} \sin 2\theta \cos 2\theta \\ - E_t^{*2} E_{t-\tau}^2 \sin^2 2\theta + \left|E_{t-\tau}\right|^2 \sin 2\theta + 2 E_t^{*} E_{t-\tau} \left|E_{t-\tau}\right|^2 \sin 2\theta \cos 2\theta \\ -2 E_t^{*} \left|E_t\right|^2 E_{t-\tau} \cos 2\theta \sin 2\theta + 2 E_t E_{t-\tau}^{*} \left|E_{t-\tau}\right|^2 \cos 2\theta \sin 2\theta \\ +4 \left|E_t\right|^2 \left|E_{t-\tau}\right|^2 \cos^2 2\theta \end{pmatrix} dt \qquad (4.12)$$

We define the complex electric field:

$$E_t = A_t e^{j\omega t}$$
$$E_{t-\tau} = A_{t-\tau} e^{j(\omega t+\phi)} \qquad (4.13)$$

Where A_t is the envelope (amplitude) of the pulse and $\phi = -\omega\tau$

By replacing these parameters in the previous equation (4.12) we get:

$$G(\tau) \propto \frac{d_{eff}}{2} \int_{-\infty}^{+\infty} \begin{pmatrix} (A_t^4 + A_{t-\tau}^4)\sin^2 2\theta - 2A_t^2 A_{t-\tau}^2(\cos 2\phi \sin^2 2\theta - 2\cos^2 2\theta) \\ -2A_t A_{t-\tau} \sin 4\theta \cos\phi (A_t^2 - A_{t-\tau}^2) \end{pmatrix} dt \qquad (4.14)$$

This relation [49] constitutes the principal equation for the type II autocorrelation interferometry. It can be divided into 3 parts:

- $DC \propto \int_{-\infty}^{+\infty} \left[(A_t^4 + A_{t-\tau}^4)\sin^2 2\theta + 4A_t^2 A_{t-\tau}^2 2\cos^2 2\theta \right] dt$
- $Nonlinear\ term \propto \int_{-\infty}^{+\infty} -2A_t^2 A_{t-\tau}^2 \cos 2\phi \sin^2 2\theta dt$
- $Linear\ term \propto \int_{-\infty}^{+\infty} -2A_t A_{t-\tau} \sin 4\theta \cos\phi (A_t^2 - A_{t-\tau}^2) dt$

The DC, the coherence term oscillating at ω (Linear term or linear fringes) and the coherence term oscillating at 2ω (Nonlinear term or nonlinear fringes) depend on the rotation angle of the crystal around the field direction.

Note that the equation (4.14) already exists in the literature [49], but it has not been demonstrated nor proven experimentally, and only a special case of a balanced return field was explained, i.e $A_t = A_{t-\tau}$, in which case the linear term vanishes. We added previously the full demonstration, and then we will be adding in the next section the metrology using nonlinear fringes by introducing new other cases such as: unbalanced return fields, dispersion

in the sample arm and non-symmetric pulse. Then later we will show experimental results which validate these cases.

4.2.2 Unbalanced return field case

In this consideration we suppose that we have

- Symmetrical Gaussian pulse envelope
- **Unbalanced** return field
- No dispersion

A Gaussian envelope can be written as:

$$A_t = a_1 e^{-t^2/u^2}$$
$$A_{t-\tau} = a_2 e^{-(t-\tau)^2/u^2} \tag{4.15}$$

Where a_1 and a_2 are two coefficients that multiply the two orthogonal fields, they give unbalanced control of the return fields from each arm and u corresponds to 0.601*FWHM of the time pulse. By putting these parameters in (4.14) we get $G(\tau)$:

$$\propto \frac{d_{eff}}{2}\int_{-\infty}^{+\infty}\left(\begin{array}{l}\left(a_1^4 e^{-\frac{4t^2}{u^2}} + a_2^4 e^{\frac{-4(t-\tau)^2}{u^2}}\right)\sin^2(2\theta) \quad (a)\\ -2a_1^2 a_2^2 e^{-2\left(\frac{t^2+(t-\tau)^2}{u^2}\right)}\left(\cos(2\omega\tau)\sin^2(2\theta) - 2\cos^2(2\theta)\right) \ (b)\\ -2a_1 a_2 \sin(4\theta)\cos(\omega\tau) e^{-\left(\frac{t^2+(t-\tau)^2}{u^2}\right)}\left(a_1^2 e^{-2\frac{t^2}{u^2}} - a_2^2 e^{-2\frac{(t-\tau)^2}{u^2}}\right)(c)\end{array}\right) dt \tag{4.16}$$

Knowing that $\int_{-\infty}^{+\infty} e^{-t^2/u^2} dt = u\sqrt{\pi}$. The first integral *(a):*

$$\left(a_1^4 + a_2^4\right)\frac{u\sqrt{\pi}}{2}\sin^2(2\theta)$$

The second integral (*b)*:

$$-2a_1^2a_2^2\frac{u\sqrt{\pi}}{2}e^{-\tau^2/u^2}\left(\cos(2\omega\tau)\sin^2(2\theta)-2\cos^2(2\theta)\right)$$

The third integral (*c*)[1]:

$$-2a_1a_2\sin(4\theta)\cos(\omega\tau)\frac{u\sqrt{\pi}}{2}\left(a_1^2-a_2^2\right)e^{-3\tau^2/4u^2}$$

Therefore the autocorrelation function becomes:

$$G(\tau)\propto d_{eff}\frac{u\sqrt{\pi}}{2}\begin{pmatrix}\left(a_1^4+a_2^4\right)\sin^2(2\theta)-\\ 2a_1^2a_2^2e^{-\tau^2/u^2}\left(\cos(2\omega\tau)\sin^2(2\theta)-2\cos^2(2\theta)\right)\\ -2a_1a_2\sin(4\theta)\cos(\omega\tau)\left(a_1^2-a_2^2\right)e^{-3\tau^2/4u^2}\end{pmatrix} \quad (4.17)$$

We can divide equation (4.17) into 3 terms

- Linear term: $-2a_1a_2\sin(4\theta)\cos(\omega\tau)\left(a_1^2-a_2^2\right)e^{-3\tau^2/4u^2}$
- DC: $\left(a_1^4+a_2^4\right)\sin^2(2\theta)+4a_1^2a_2^2e^{-\tau^2/u^2}\cos^2(2\theta)$
- Nonlinear term: $2a_1^2a_2^2e^{-\tau^2/u^2}\cos(2\omega\tau)\sin^2(2\theta)$

We illustrate in *Figure 4-5* the linear term as a function of the delay and the angle (a_1*=1* and a_2*=3*). We do not observe linear fringes if the angle is equal to *0*^{o} or *45*^{o}, and the maximum contrast is observed when the angle is *22.5*^{o}.

[1] $e^{-\left(\frac{t^2+(t-\tau)^2}{u^2}\right)}.e^{-2\frac{t^2}{u^2}}=e^{-\frac{4}{u^2}\left[\left(t-\frac{\tau}{4}\right)^2+\frac{3\tau^2}{16}\right]}$ and $e^{-\left(\frac{t^2+(t-\tau)^2}{u^2}\right)}.e^{-2\frac{(t-\tau)^2}{u^2}}=e^{-\frac{4}{u^2}\left[\left(t-3\frac{\tau}{4}\right)^2+\frac{3\tau^2}{16}\right]}$

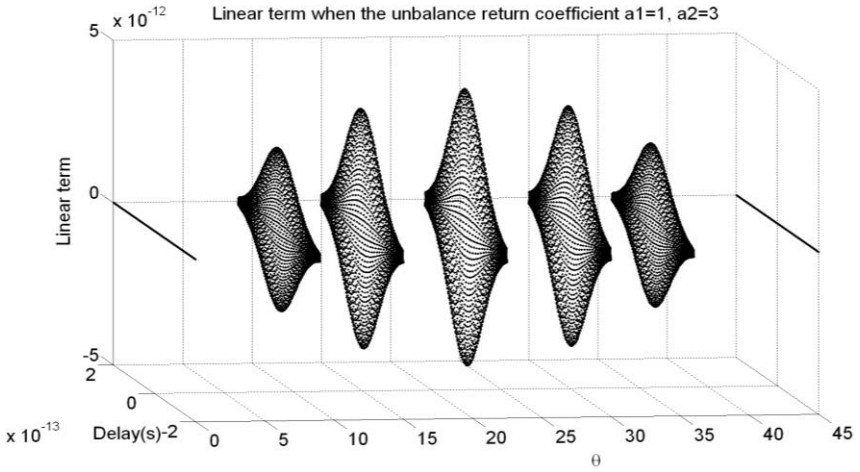

Figure 4-5 Linear term as function of the delay and the angle. a_1=1, a_2=3

Figure 4-6 illustrates the nonlinear term as a function of the delay and the angle. We see that nonlinear fringes disappear at the angle zero, then it rise to reach the maximum contrast when the angle is 45^o.

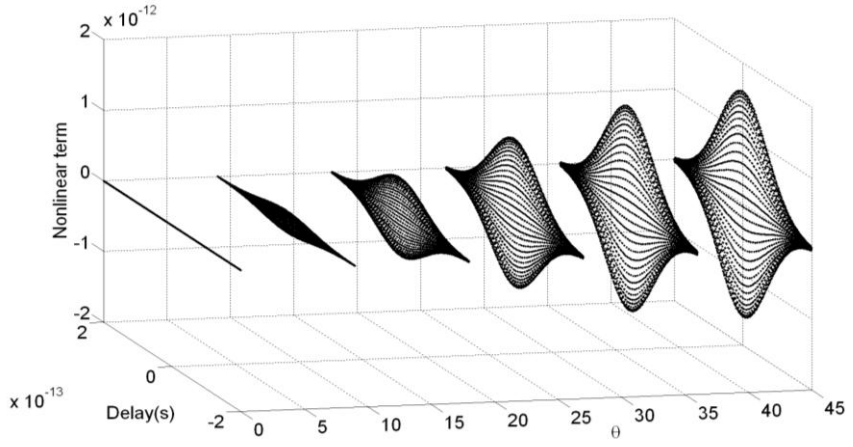

Figure 4-6 Nonlinear term as a function of the delay and the angle

Figure 4-7 illustrates the DC term as a function of the delay and the angle. We see that the DC is minimum when the angle is zero and reaches its maximum when the angle is 45^o.

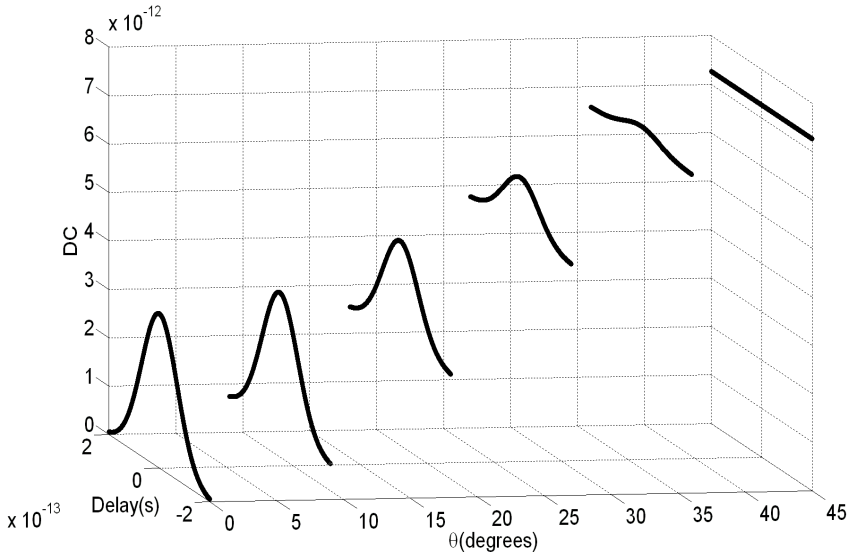

Figure 4-7 DC term as a function of the delay and the angle

By using $TF[e^{-\alpha t^2}] = \sqrt{\pi/\alpha}\, e^{-\pi^2 f^2/\alpha}$, the Fourier transform of the autocorrelation function $G(f)$ can be written:

$$\propto \frac{d_{eff} u\sqrt{\pi}}{2}\left(\begin{array}{l} -2a_1^{\,2}a_2^{\,2}u\sqrt{\pi}e^{-u^2\pi^2 f^2} \otimes \left(\begin{array}{l}\left(\dfrac{\delta(f-2f_0)+\delta(f+2f_0)}{2}\right)\times \\ \sin^2(2\theta)-2\cos^2(2\theta)\delta(f)\end{array}\right)+ \\ \left(a_1^{\,4}+a_2^{\,4}\right)\sin^2(2\theta)\delta(f)-2a_1a_2\sin(4\theta)\times \\ \left(\dfrac{\delta(f-f_0)+\delta(f+f_0)}{2}\right)\left(a_1^{\,2}-a_2^{\,2}\right)\otimes 2u\sqrt{\dfrac{\pi}{3}}e^{-\frac{4u^2\pi^2 f^2}{3}} \end{array}\right) \tag{4.18}$$

Where f_0 is the central frequency of the laser beam.

And finally we get:

$$G(f) \propto \left(a_1^4 + a_2^4\right)\sin^2(2\theta)\,\delta(f) + 4a_1^2 a_2^2 u\sqrt{\pi}\, e^{\frac{-u^2 f^2}{4}} \cos^2(2\theta) \quad DC$$

$$-a_1^2 a_2^2 u\sqrt{\pi}\sin^2(2\theta)\left(e^{-u^2\pi^2(f+2f_0)^2} + e^{-u^2\pi^2(f-2f_0)^2}\right) \quad 2f_0$$

$$-a_1 a_2 (a_1^2 - a_2^2)\sin(4\theta)\, 2u\sqrt{\pi/3}\left(e^{\frac{-4u^2\pi^2(f-f_0)^2}{3}} + e^{\frac{-4u^2\pi^2(f+f_0)^2}{3}}\right) \quad f_0 \qquad (4.19)$$

By comparing the maximum amplitude $A(f_0)$ at the frequency f_0 and the maximum amplitude $A(2f_0)$ at the frequency $2f_0$, we get:

$$\left|\frac{A(f_0)}{A(2f_0)}\right| = \frac{a_1 a_2 \left|a_1^2 - a_2^2\right|\sin(4\theta)\, 2u\sqrt{\pi}}{\sqrt{3}a_1^2 a_2^2 u\sqrt{\pi}\sin^2(2\theta)} = \frac{4\sin(2\theta)\cos(2\theta)\left|a_1^2 - a_2^2\right|}{a_1 a_2\sqrt{3}\sin^2(2\theta)}$$

$$\left|\frac{A(f_0)}{A(2f_0)}\right| = \frac{4}{\sqrt{3}\tan(2\theta)}\left|\frac{a_1}{a_2} - \frac{a_2}{a_1}\right| \qquad (4.20)$$

We define the balance coefficient $r = \frac{a_1}{a_2} \le 1$, therefore we get

$$\left|\frac{A(f_0)}{A(2f_0)}\right| = \frac{4}{\sqrt{3}\tan(2\theta)}\left|\frac{r^2 - 1}{r}\right| \qquad (4.21)$$

In *Figure 4-8*, we represent the maximum ratio of the linear fringes over the nonlinear fringes, when the rotation angle of the crystal is equal to 33^o. If the balance coefficient r is equal to 1 (balanced return field) the linear fringes vanish completely, but when we unbalance the two fields, the linear fringes rise and dominate over the nonlinear fringes. For example when r is equal to 0.4 this ratio is equal to 2.

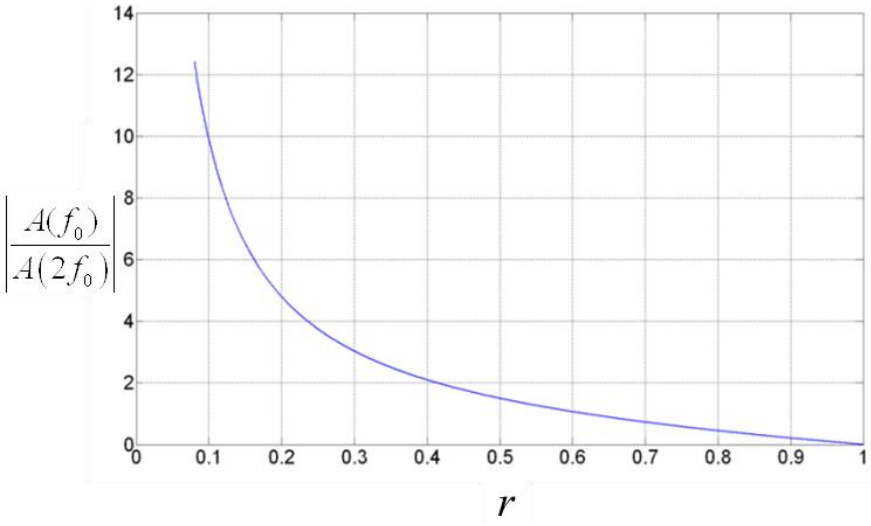

Figure 4-8 Ratio between linear and nonlinear fringes, where $\tan(\theta) = {}^{4}/_{\sqrt{3}}$ *or θ=33*

We can conclude also that:

If $\theta=0^0$ *or* 90^0:

$$G(f) \propto 4a_1^{\,2}a_2^{\,2}u\sqrt{\pi}e^{\frac{-u^2f^2}{4}}$$

both linear and nonlinear fringes vanish.

If $\theta=45^0$:

$$G(f) \propto \left(a_1^{\,4}+a_2^{\,4}\right)\delta(f) - a_1^{\,2}a_2^{\,2}u\sqrt{\pi}\left(e^{\frac{-u^2(f+2f_0)}{4}} + e^{\frac{-u^2(f-2f_0)}{4}}\right)$$

we observe only nonlinear fringes at the doubled frequency $2f_0$.

In fact the angle 45^o is very critical, that's why further calculation was made for this specific angle, by considering that the beam splitter polarizer has some imperfection in its extinction ratio[1].

[1] The extinction ratio (ER) is the ratio of the maximum transmission of a linear polarized signal when the polarizer's axis is aligned with the signal to the minimum transmission when the polarizer is rotated by 90°

- **Beam splitter polarizer with imperfect polarizations**

Let's consider an imperfect polarization in the polarized beam splitter, see *Figure 4-9*. Each field at the entrance of the crystal consists of the desired field with the strong value and a small part of the undesired field, so we can write:

$$E_1 = E_t + \alpha E_{t-\tau}$$
$$E_2 = E_{t-\tau} + \beta E_t \qquad (4.22)$$

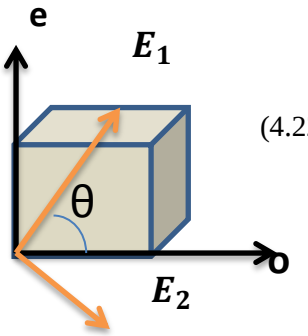

Where α and β correspond to the extinction ratio of the beam splitter.

If the crystal is turned at 45^o we rewrite the fields with respect to the ordinary and the extraordinary axis:

$$E^e = \frac{\sqrt{2}}{2}\left(E_1 - E_2\right) = \frac{\sqrt{2}}{2}\left(E_t\left(1-\beta\right) + E_{t-\tau}\left(\alpha - 1\right)\right) \qquad (4.23)$$

$$E^o = \frac{\sqrt{2}}{2}\left(E_1 + E_2\right) = \frac{\sqrt{2}}{2}\left(E_t\left(1+\beta\right) + E_{t-\tau}\left(\alpha + 1\right)\right) \qquad (4.24)$$

The nonlinear polarization is calculated in this case:

$$E^e.\mathrm{E}^o = \frac{1}{2}\left[E_t^2\left(1-\beta^2\right) + E_{t-\tau}^2\left(\alpha^2 - 1\right) + 2E_t E_{t-\tau}\left(\alpha - \beta\right)\right] \qquad (4.25)$$

The autocorrelation function:

$$G \propto \int_{-\infty}^{+\infty} \left|E^o.E^e\right|^2 dt = \int_{-\infty}^{+\infty} \left|E_t\right|^4 \left(1-\beta^2\right)^2 + \left(E_t^2 \overset{*}{E}_{t-\tau}^2 + E_{t-\tau}^2 \overset{*}{E}_t^2 \right)\left(\alpha^2-1\right)\left(1-\beta^2\right)$$
$$+2\left(E_t^2 \overset{*}{E}_t \overset{*}{E}_{t-\tau} + \overset{*}{E}_t^2 E_t E_{t-\tau} \right)\left(1-\beta^2\right)\left(\alpha-\beta\right) + \left|E_{t-\tau}\right|^4 \left(\alpha^2-1\right)^2 dt$$
$$+2\left(\alpha^2-1\right)\left(\alpha-\beta\right)\left(\overset{*}{E}_t \overset{*}{E}_{t-\tau} E_{t-\tau}^2 + E_t^2 E_{t-\tau} \overset{*}{E}_{t-\tau}^2 \right) + 4\left|E_t\right|^2 \left|E_{t-\tau}\right|^2 \left(\alpha-\beta\right)^2$$

(4.26)

By replacing the two complex fields with the expressions defined in (4.13) we obtain:

$$G \propto \left[a_1^4 \left(1-\beta^2\right)^2 + a_2^4 \left(\alpha^2-1\right)^2 \right] u \frac{\sqrt{\pi}}{2}$$
$$+ 2a_1^2 a_2^2 u \frac{\sqrt{\pi}}{2} e^{-\tau^2/u^2} \left[\left(\alpha^2-1\right)\left(1-\beta^2\right)\cos\left(2\omega\tau\right) + 2\left(\alpha-\beta\right)^2 \right]$$
$$+ 4a_1 a_2 \left(\alpha-\beta\right) e^{-3\tau^2/u^2} \left[a_1^2 \left(1-\beta^2\right) - a_2^2 \left(1-\alpha^2\right) \right] \cos\left(\omega\tau\right)$$

(4.27)

From this last equation, we see that the linear fringes are still present even if the angle is 45^o. A simulation will come later to illustrate the sensitivity of this imperfect polarization.

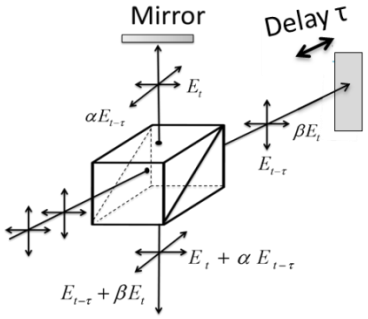

Figure 4-9 Schematic of the polarizations after passage through the PBS with non-optimal extinction ratio

4.2.3 Balanced return field case

- Symmetrical Gaussian envelope
- Balanced return field
- No dispersion is taken into consideration

By considering a balanced return field ($a_1 = a_2$) the expression of $G(\tau)$ calculated previously in equation (4.17) becomes [49]:

$$G(\tau) \propto d_{eff} u\sqrt{\pi}\, a_1^4 \left(\sin^2 2\theta - e^{-\tau^2/u^2}(-2\cos^2 2\theta + \cos 2w\tau \sin^2 2\theta) \right) \quad (4.28)$$

We see clearly that the third part (linear term) vanishes completely from the equation(4.28), which means that we will observe only nonlinear fringes at the frequency $2f_0$.

4.2.4 Dispersion in one arm

Since we are interested to work with Silicon, we considered now:

- Symmetrical Gaussian envelope
- Balanced return field
- Dispersion is taken into consideration in one of the two arms (propagation through silicon).

In these conditions we can write:

- The non-dispersive arm:

$$E_t = A_t e^{j\omega t},\ where\ A_t = a_1 e^{-\frac{t^2}{u^2}} \quad (4.29)$$

- We used for the dispersive arm the definition and method from Siegman [50]:

$$E_{t-\tau} = A_{t-\tau} e^{j(\omega t+\phi)} = a_2 e^{j(\omega(t-\tau)-\beta z)} . e^{-\Gamma(z)\left(t-\tau-\beta' z\right)^2} \quad (4.30)$$

We recall the propagation constant β as a function of the frequency and its first and second derivatives:

$$\beta = k = n(\omega)\frac{\omega}{c};\ \beta' = \frac{dk}{d\omega}\ and\ \beta'' = \frac{d^2k}{d\omega^2} = \frac{\lambda^3}{2\pi c^2}\frac{\partial^2 n}{\partial \lambda^2}$$

And the altered Gaussian pulse parameter after traveling a distance *z*:

$$\Gamma(z) = \left(u^2 + 2j\beta'' z\right)^{-1}$$

We rewrite $\Gamma(z)$ as: $\Gamma(z) = \dfrac{1}{u^2 + 2j\beta'' z} = \dfrac{u^2}{u^4 + 4\beta''^2 z^2} - \dfrac{2j\beta'' z}{u^4 + 4\beta''^2 z^2}$

For simplification we define:

$$\frac{1}{h^2} = \frac{u^2}{u^4 + 4\beta''^2 z^2}$$

$$\alpha = \frac{2\beta'' z}{u^4 + 4\beta''^2 z^2} \qquad (4.31)$$

$$m_1 = \tau + \beta' z$$

h can be seen as the new $FWHM \times 0.601$ under dispersion, α(alpha) is the parameter responsible for the dispersion or the chirp effect, and *z* is the thickness of silicon. Using equation (4.30) we can write:

$$\begin{aligned} A_{t-\tau} &= a_2 e^{-\frac{(t-m_1)^2}{h^2}} \\ \phi &= -\omega\tau - \beta z + \alpha(t-m_1)^2 \end{aligned} \qquad (4.32)$$

We note $m_2 = -\omega\tau - \beta z \Rightarrow \phi = m_2 + \alpha(t-m_1)^2$

By using all these previous assumptions, we inject the equations (4.29) and (4.30) in the previous equation (4.14) , we get $G(\tau)$:

$$\propto \int_{-\infty}^{+\infty} \begin{pmatrix} \left(a_1^4 e^{-\frac{4t^2}{u^2}} + a_2^4 e^{\frac{-4(t-m_1)^2}{h^2}} \right) \sin^2(2\theta) \qquad (I) \\ -2a_1^2 a_2^2 e^{-2\left(\frac{t^2}{u^2}+\frac{(t-m_1)^2}{h^2}\right)} \begin{pmatrix} \cos(2m_2 + 2\alpha(t-m_1)^2)\sin^2(2\theta) \\ -2\cos^2(2\theta) \end{pmatrix} (II) \\ -2a_1 a_2 \sin(4\theta)\cos(m_2 + \alpha(t-m_1)^2) e^{-\left(\frac{t^2}{u^2}+\frac{(t-m_1)^2}{h^2}\right)}. \\ \left(a_1^2 e^{-2\frac{t^2}{u^2}} - a_2^2 e^{-2\frac{(t-m_1)^2}{h^2}} \right) \quad (III) \end{pmatrix} dt$$

(4.33)

To compute analytically this integral, a lot of notations were taken into consideration. See details in Appendix B. The final expression is given by:

$$G(\tau) \propto \sqrt{\frac{\pi}{2}} \left(a_1^4 u + a_2^4 h \right) \sin^2(2\theta)$$

$$+2a_1 a_2 \sin(4\theta) \begin{pmatrix} a_1^2 e^{-\frac{3m_1^2}{u^2+3h^2}} \frac{g_2\sqrt{\pi}}{f_2} e^{-\frac{\alpha^2 g_2^2 l_2^2}{f_2^2}} \begin{pmatrix} \cos\left(m_2 + \frac{\alpha l_2^2}{f_2^2} \right) \sqrt{\frac{f_2+1}{2}} - \\ \sin\left(m_2 + \frac{\alpha l_2^2}{f_2^2} \right) \sqrt{\frac{f_2-1}{2}} \end{pmatrix} \\ -a_2^2 e^{-\frac{3m_1^2}{3u^2+h^2}} \frac{g_3\sqrt{\pi}}{f_3} e^{-\frac{\alpha^2 g_3^2 l_3^2}{f_3^2}} \begin{pmatrix} \cos\left(m_2 + \frac{\alpha l_3^2}{f_3^2} \right) \sqrt{\frac{f_3+1}{2}} - \\ \sin\left(m_2 + \frac{\alpha l_3^2}{f_3^2} \right) \sqrt{\frac{f_3-1}{2}} \end{pmatrix} \end{pmatrix}$$

$$-2a_1^{\,2}\sqrt{\pi}a_2^{\,2}g_1 e^{-\frac{2m_1^{\,2}}{u^2+h^2}}\left(\begin{array}{l}\dfrac{e^{-\frac{4\alpha^2 g_1^{\,2}l_1^{\,2}}{f_1^{\,2}}}}{f_{1`}}\left(\left(\begin{array}{l}\cos\left(2m_2+\dfrac{2\alpha l_1^{\,2}}{f_1^{\,2}}\right)\sqrt{\dfrac{f_1+1}{2}}-\\ \sin\left(2m_2+\dfrac{2\alpha l_1^{\,2}}{f_1^{\,2}}\right)\sqrt{\dfrac{f_1-1}{2}}\end{array}\right)\sin^2(2\theta)\right)\\ -2\cos^2(2\theta)\end{array}\right)$$

(4.34)

We recall the expressions of all the symbols:

$$\alpha=\frac{2\beta'' z}{u^4+4\beta''^2 z^2};\frac{1}{h^2}=\frac{u^2}{u^4+4\beta''^2 z^2}$$

$$m_1=\tau+\beta' z;m_2=-\omega\tau-\beta z$$

$$\frac{1}{g_1^{\,2}}=\frac{2(h^2+u^2)}{u^2h^2};\frac{1}{g_2^{\,2}}=\frac{3h^2+u^2}{u^2h^2};\frac{1}{g_3^{\,2}}=\frac{h^2+3u^2}{u^2h^2}$$

$$n_1=\frac{m_1u^2}{h^2+u^2};n_2=\frac{m_1u^2}{3h^2+u^2};n_3=\frac{3m_1u^2}{h^2+3u^2}$$

$$l_1=n_1-m_1;l_2=n_2-m_1;l_3=n_3-m_1$$

$$f_1=\sqrt{1+4\alpha^2 g_1^{\,4}};\ f_2=\sqrt{1+\alpha^2 g_2^{\,4}};\ f_3=\sqrt{1+\alpha^2 g_3^{\,4}}\quad(4.35)$$

4.3 Simulations

Some simulations of the previous sections were done based on the parameters of our setup; the wavelength of the femtosecond laser is *1300nm* and the parameter *u* is *60fs* (*FWHM=100fs*). Note that in all the following graphs, the vertical axis has an arbitrary unit.

The goal behind the simulations is to give a full understanding of the nonlinear fringes' theory and metrology, to give a prediction on how the fringes will look like in experiment, and to show what affects the contrast of the fringes, which is our goal after all, to enhance the quality of the images in tomographic measurements.

4.3.1 Unbalanced return field

We present in *Figure 4-10* the second order autocorrelation signal for different rotation angle, see equation(4.17). We considered an unbalanced return field with a *10%* difference ($a_2=1.1*a_1$). As we see when the angle is set to zero we do not observe any fringe, and the FWHM can be estimated to *100fs*. By changing the angle to 15^o we observe both linear and nonlinear fringes, the nonlinear fringes are observed as a dense pattern on top, while linear fringes produce the lighter pattern below it; this comes from the fact that the nonlinear fringes have the double frequency of linear fringes. We see that for an angle of 30^o the contrast of these fringes becomes bigger, and the maximum contrast is observed when the angle is set to 45^o, where we observe only nonlinear fringes.

In order to compare the contrast of both linear and nonlinear fringes, we illustrated in *Figure 4-11* the fast Fourier transform using *Matlab* of all the 4 cases plotted in *Figure 4-10,* and we plotted the same graph using the analytical formula in equation (4.18) (see graphs in Appendix E). As we see

when the angle is set to 15^0 or 30^0 we observe two peaks, one at the frequency f_0 and the second at the doubled frequency $2f_0$. We zoomed on both[1]: the linear peak when the angle is 15^0 and the nonlinear peak when the angle is 30^0. The nonlinear peak has a wider Gaussian envelope in the Fourier domain compared to the linear peak; this comes directly from the equation (4.17) . The envelope of the linear peak can be written:

$$e^{\frac{-4u^2\pi^2(f-f_0)^2}{3}}$$

The corresponding $FHWM = \frac{\sqrt{3\ln 2}}{\pi u} = \frac{0.459}{u}$

And the envelope of the nonlinear peak is:

$$e^{-u^2\pi^2(f-f_0)^2}$$

The corresponding $FHWM = \frac{2\sqrt{\ln 2}}{\pi u} = \frac{0.53}{u}$

The contrast of nonlinear fringes is more important compared to linear fringes for the configuration $a_2=1.1*a_1$, and this contrast becomes more important when the angle rises. The maximum of the linear peak is reduced when we switch from the angle 15^o *to* 30^o; this result comes directly from equation(4.21). Notice that when the angle is 45^o the linear fringes vanish completely.

[1] The Gaussian envelope does not depend on the angle; we chose a different angle in the envelope comparison to have better observation since we are limited by the space in each graph.

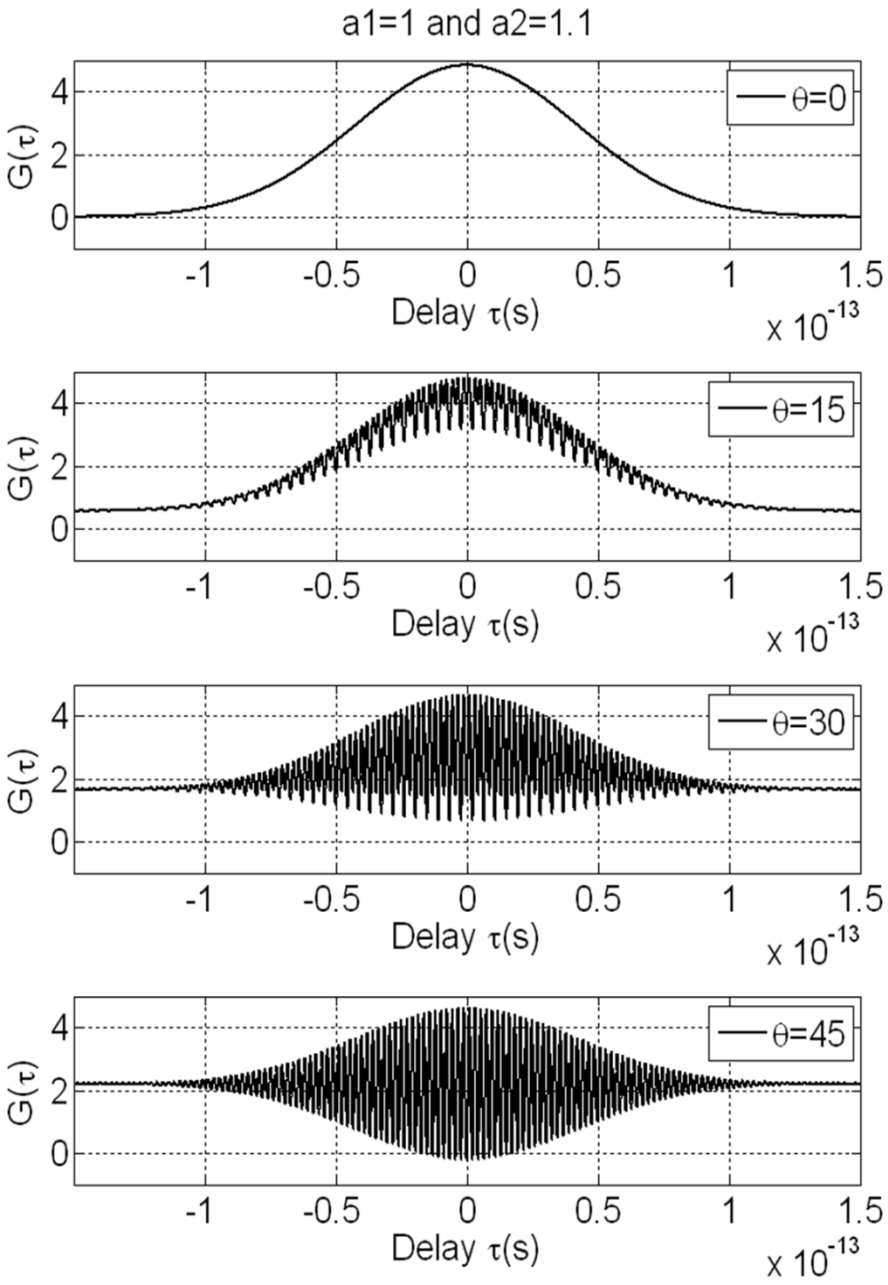

Figure 4-10 Autocorrelation function for different rotation angle .

Unbalanced return field a_1=1 and a_2=1.1

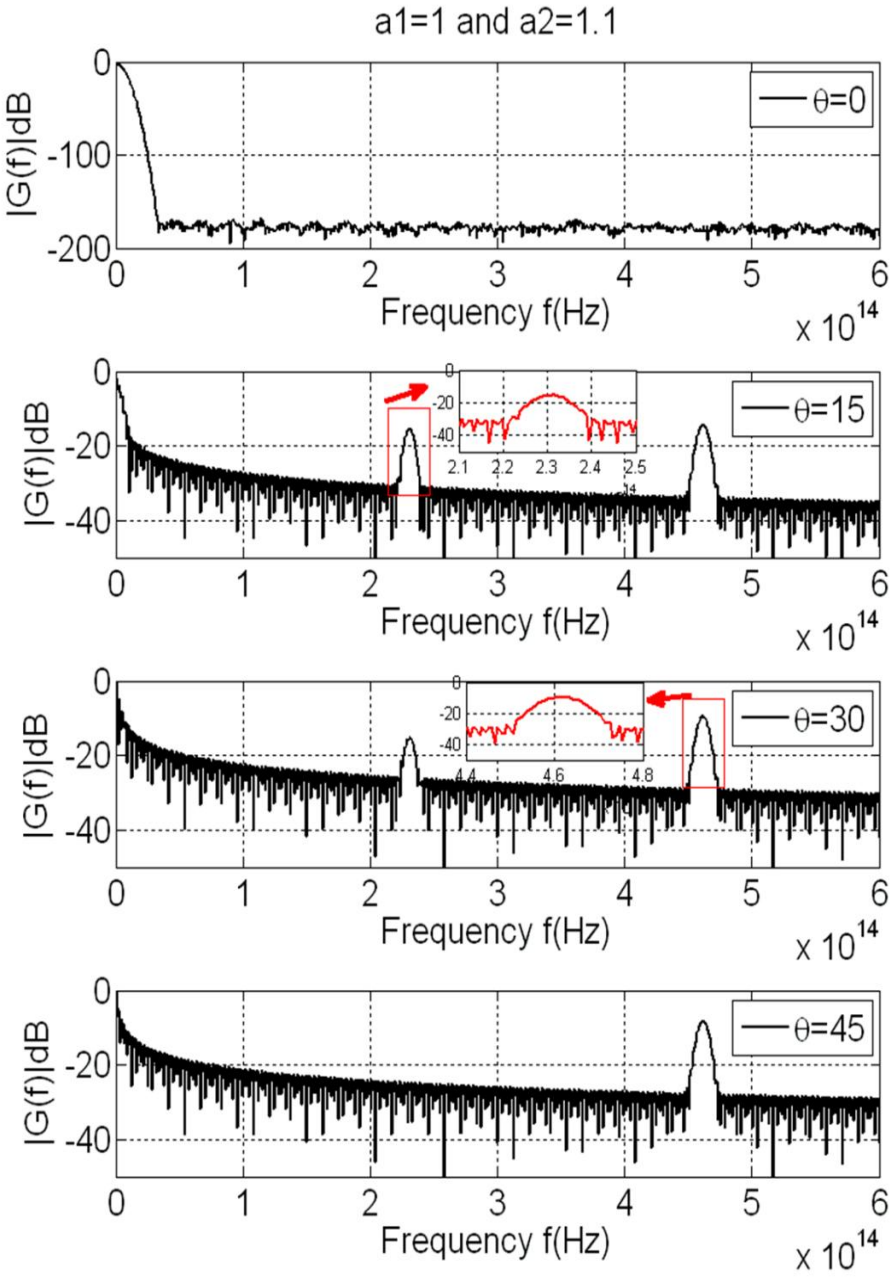

Figure 4-11 Fourier transform of the autocorrelation function for different rotation angle. a1=1 and a2=1.1.

In *Figure* 4-12 we demonstrate how fringes will look like when both linear and nonlinear fringes are present. We chose the angle 30^o and then we converted the simulation of the autocorrelation function to a bitmap image using *Matlab*. Knowing that the nonlinear fringes have the double frequency of the linear ones, we conclude that each vertical line corresponds to a nonlinear fringe, and when the line becomes darker[1] this means that we have the coincidence of linear and nonlinear fringes, which add up at this position.

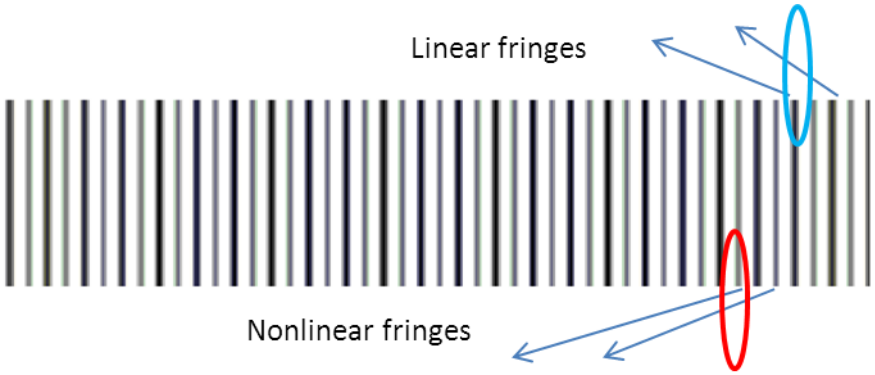

Figure 4-12 prediction of the form of fringes when the angle is 30. $a_1=1$ *and* $a_2=1.1$

Another simulation was made by changing the coefficient $a_2=1.3a_1$. We see clearly in *Figure 4-13*, that the contrast of the linear fringes becomes important compared to nonlinear fringes. The Fourier transform of the autocorrelation function is shown in *Figure 4-14* where we see that the contrast of linear fringes is more important when the angle is 15^o, thus when the angle is 30^o both linear and nonlinear fringes have almost the same contrast, and same as before the linear fringe vanishes when the angle is 45^o.

[1] The nonlinear fringes are repeated two times compared to the linear one.

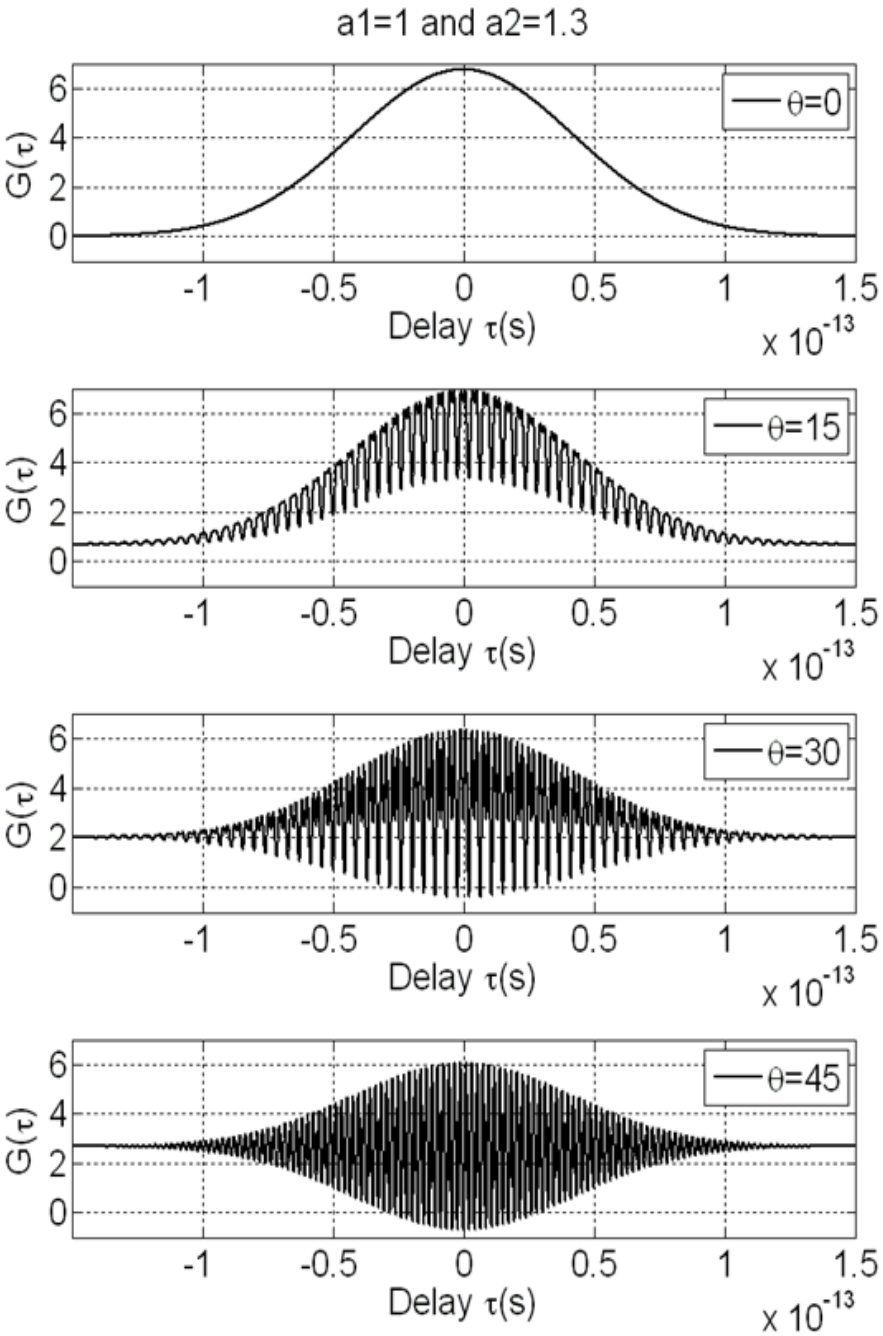

Figure 4-13 Autocorrelation function for different rotation angle for unbalanced return field a_1=1 and a_2=1.3

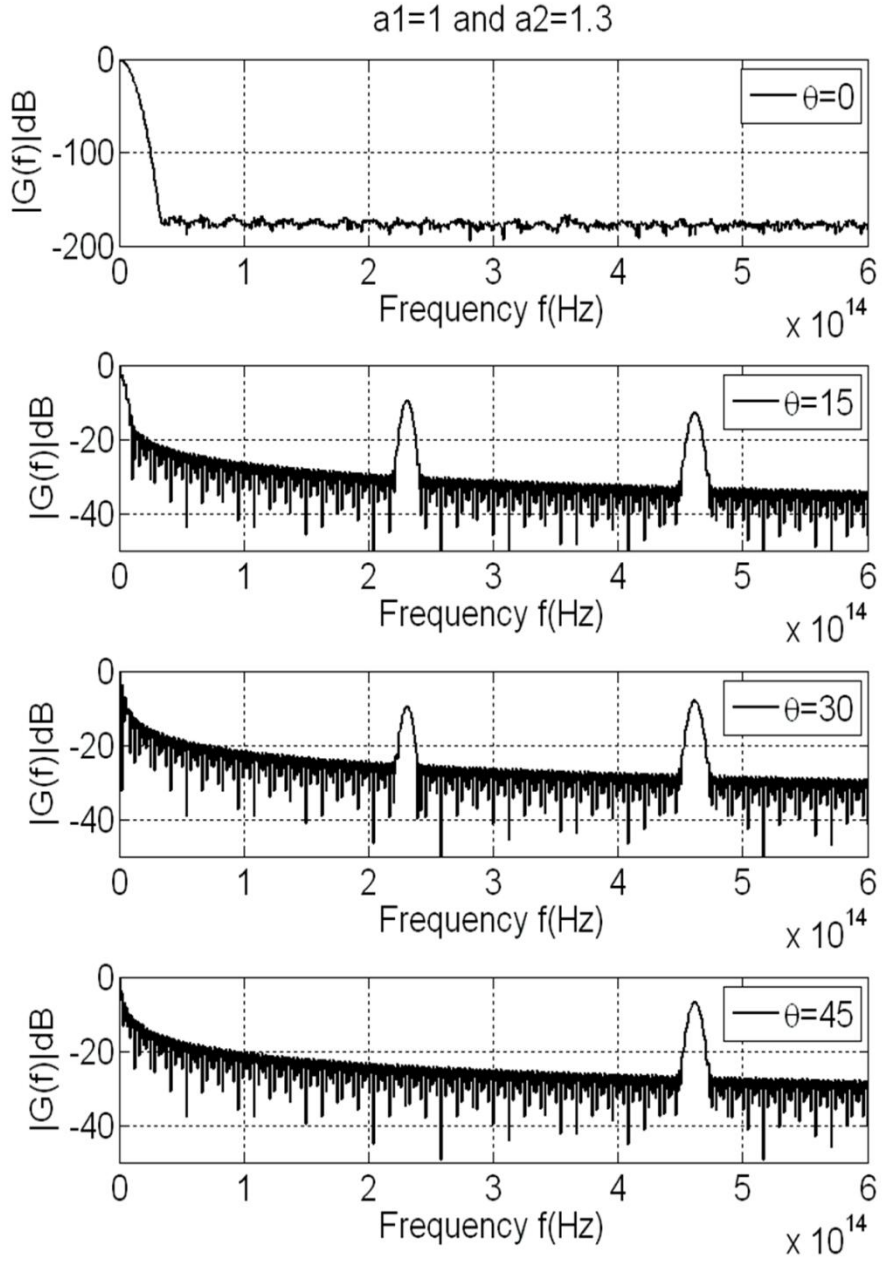

Figure 4-14 Fourier transform of the autocorrelation function for different angles. a1=1 and a2=1.3.

We illustrate in *Figure* 4-15 the prediction of the fringes when $a_2=1.3a_1$ and the angle is set to 30^o. The red ellipse corresponds to the nonlinear fringes only and the blue ellipse corresponds to the mixing of linear and nonlinear fringes. Since the linear term this time is slightly equal to the nonlinear term, it explains why the sum of linear and nonlinear term (blue ellipse) is dominant and quite darker over the nonlinear term only (red ellipse) which is almost invisible.

Figure 4-15prediction of the form of the fringes when the angle is 30. a1=1 and a2=1.3

<u>Further analysis when the angle is around 45^o (Near maximum doubling) and the effect of the delay</u>

If we look back at the equation(4.17), it can be divided into 3 terms:

- DC term :

$$G_1(\tau)=\left(a_1^{\,4}+a_2^{\,4}\right)\frac{u\sqrt{\pi}}{2}\sin^2(2\theta)+4a_1^{\,2}a_2^{\,2}\frac{u\sqrt{\pi}}{2}e^{-\tau^2/u^2}\cos^2(2\theta) \tag{4.36}$$

- Nonlinear term:

$$G_2(\tau)=-2a_1^{\,2}a_2^{\,2}\frac{u\sqrt{\pi}}{2}e^{-\tau^2/u^2}\cos(2\omega\tau)\sin^2(2\theta) \tag{4.37}$$

- Linear term:

$$G_3(\tau) = -2a_1a_2\sin(4\theta)\cos(\omega\tau)\frac{u\sqrt{\pi}}{2}\left(a_1^{\,2} - a_2^{\,2}\right)e^{-3\tau^2/4u^2} \qquad (4.38)$$

We take for example $\theta=44^0$, $a_1=1$ *and* $a_2=3$, in other words we are at the near maximum self-doubling with unbalanced return field. *Figure 4-16* shows that the linear term presented in the red curve is almost negligible when comparing it to the nonlinear term presented in the blue curve, this is true when we work around the optical contact (delay=0s). But when we are far from the optical contact the two terms become almost the same, which is due to the fact that the two terms have different exponential envelopes, the nonlinear envelope $e^{-\tau^2/u^2}$ is more decreasing than the linear envelope $e^{-0.75\tau^2/u^2}$.

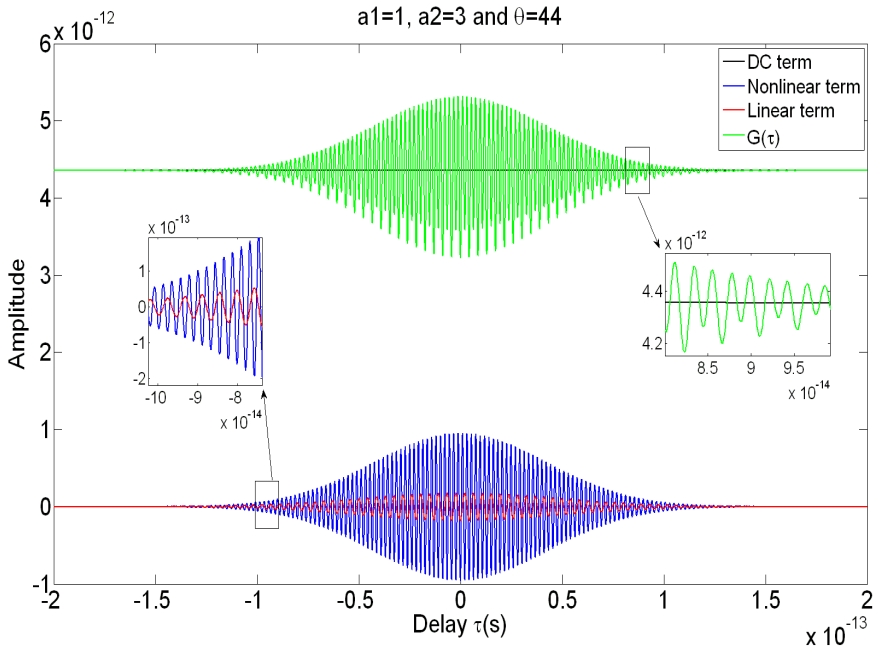

Figure 4-16 Autocorrelation function at the near maximum self-doubling vs the delay $\theta=44^0$, $a_1=1$ *and* $a_2=3$

Figure 4-17 illustrates the prediction of the fringes in this case, we see at the center of the image that the nonlinear fringes are dominant, because each vertical line corresponds to a nonlinear fringe and all these lines have nearly the same contrast, but at the right of the image far from the optical contact we see that the contrast becomes different, where we observe linear and nonlinear fringes. If the vertical line is very intense it means linear + nonlinear fringes, and if it is less intense it means only nonlinear fringe, this is explained as before by the difference between the two exponential envelopes.

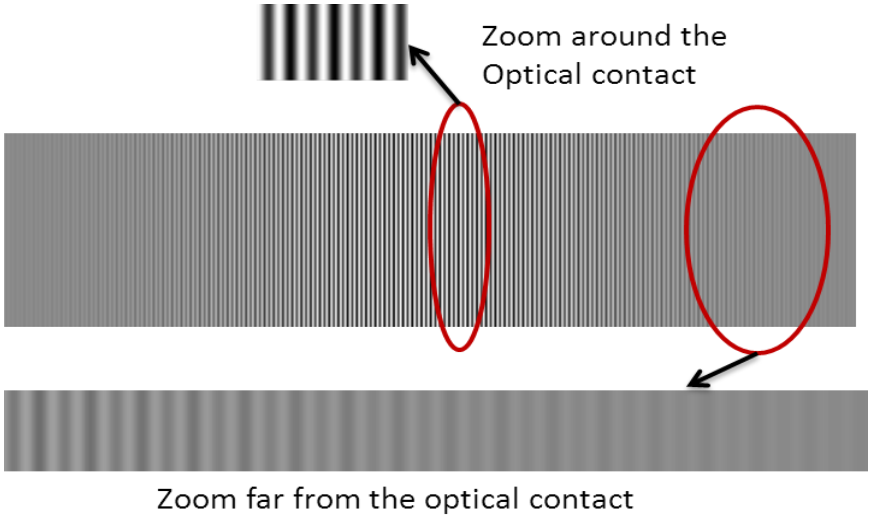

Figure 4-17 Prediction of the form of fringes in the case of $\theta=44^0$, $a_1=1$ and $a_2=3$

By setting this time $\theta=42^0$, $a_1=1$ *and* $a_2=3$, we observe in *Figure 4-18* a major difference compared to the previous case: the linear term presented in the red curve is quite comparable to the nonlinear term presented in the blue curve. When the delay is around zero the nonlinear term is slightly larger than the linear one, but when it is far from zero the two terms are equal.

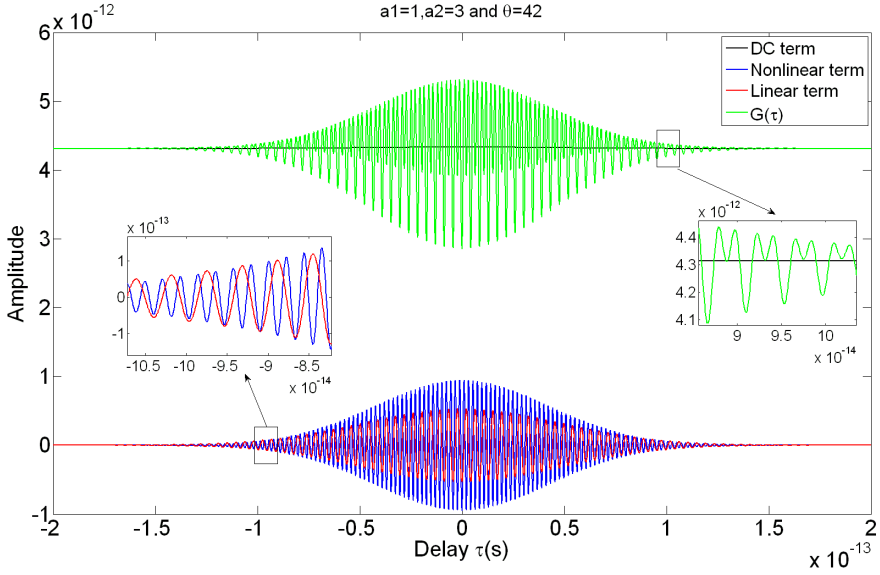

Figure 4-18 Autocorrelation function at the near maximum self-doubling vs the delay .$\theta=42^0$, $a_1=1$ and $a_2=3$

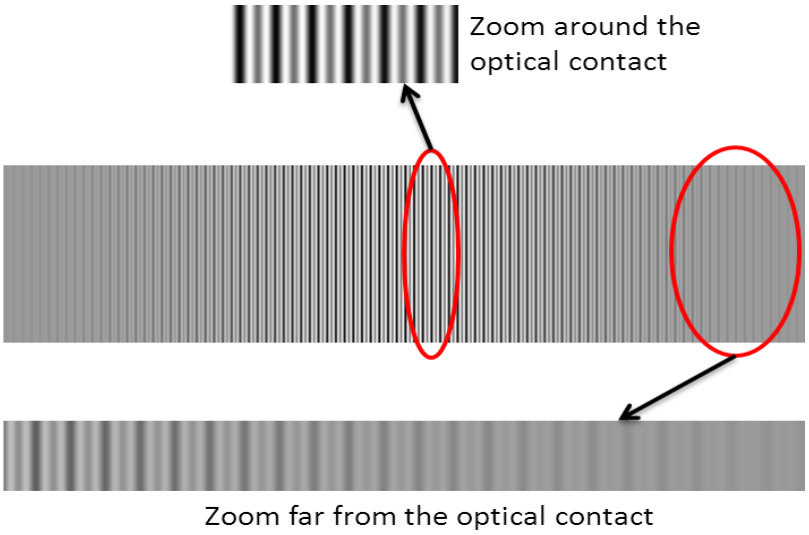

Figure 4-19 Prediction of the form of fringes in the case of $\theta=42^0$, $a_1=1$ and $a_2=3$

Figure 4-19 illustrates the prediction of the fringes in this case ($\theta=42^0$, $a_1=1$ *and* $a_2=3$). Around the optical contact, the most intense line corresponds to

linear + nonlinear fringes, and the line with less intensity corresponds to nonlinear term only. The difference in contrast comes from the presence of the linear term with a large value.

Imperfect polarization in the polarizer beam splitter extinction ratio

We illustrate in this paragraph the effect of having imperfect polarization in the beam splitter extinction ratio. This default will lead to observe linear fringes even if the angle is 45^0. The simulations are based on the equation derived in(4.27).

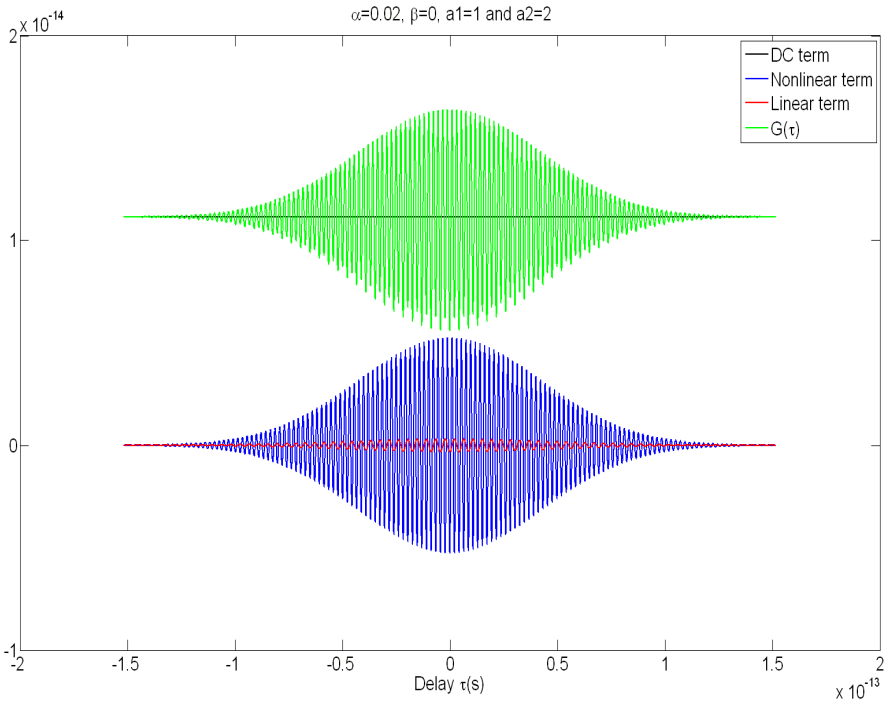

Figure 4-20 the effect of the extinction ratio in the PBS on the presence of linear fringes even when the angle is 45^0.α=0.02 and β=0

Figure 4-20 shows a comparison between the linear term and the nonlinear term if the coefficient α is equal to *0.02* and the balance coefficients are equal to 1 and 2. We see that the linear term in the red curve is nearly negligible when it is compared to the nonlinear term in the blue curve; the autocorrelation function is presented in the green curve.

Another simulation was made by changing only the coefficient α to 0.06. It is shown in *Figure* 4-21 that the linear term becomes comparable to the nonlinear term. Note that if $\alpha=\beta$ the linear term will vanish at the angle 45^0. In other words if the default appears in each arm equally the linear term will not be present when the angle is 45^0.

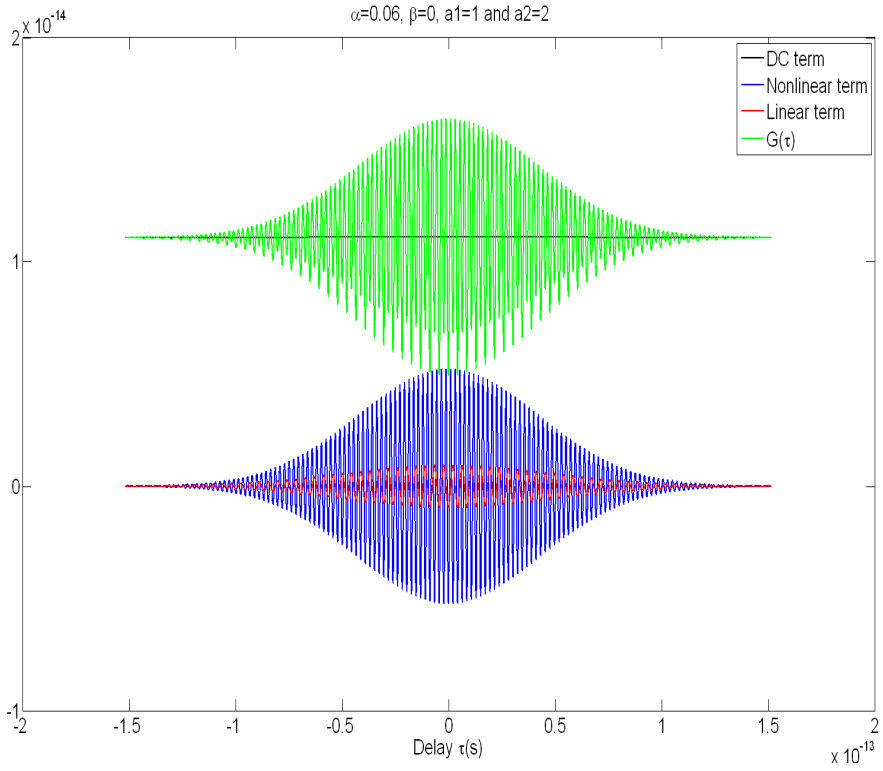

Figure 4-21 the effect of the extinction ratio in the PBS on the presence of linear fringes even when the angle is 45^0.α=0.06 and β=0

4.3.2 Balanced return fields

This consideration consists of setting the two coefficients a_1 and a_2 equal to 1, which means that the fields returning from each arm are equal. We recall the expression of the autocorrelation function:

$$G(\tau) \propto 2\left(\sin^2 2\theta - e^{-\tau^2/u^2}(-2\cos^2 2\theta + \cos 2w\tau \sin^2 2\theta) \right)$$

The maximum of *G (τ) at* zero delay*:*

$$\max(G) = 4$$

The minimum of *G(τ)* at zero delay:

$$min\left(G\right) = 2 + 2cos\left(4\theta\right)$$

The pedestal of *G(τ)* when the delay is large enough:

$$DC = ped\left(G\right) = 2\sin^2\left(2\theta\right)$$

The contrast of the nonlinear fringes for zero delay is:

$$Contrast = \frac{\max(G) - \min(G)}{\max(G) + \min(G)} = \frac{1 - \cos\left(4\theta\right)}{3 + \cos\left(4\theta\right)}$$

It can be easily demonstrated [1] that the maximum contrast is obtained when the angle is 45^0.

We presented in *Figure 4-22* the contrast of the nonlinear fringes as a function of the delay and the angle, we see that the maximum contrast is obtained when the delay is zero and the angle is 45^o.

From these equations we see that the pedestal is proportional to the square of the sinus of twice the angle, the maximum pedestal and the

[1] By deriving the contrast: $\frac{d\left(contrast\right)}{d\theta} = 0$ we obtain $\theta=45^0$ and the contrast is therefore equal to 1

maximum contrast are obtained when the angle is 45^o. By looking at the *Figure 4-23* and *Figure 4-24*, we only observe nonlinear fringes in this case.

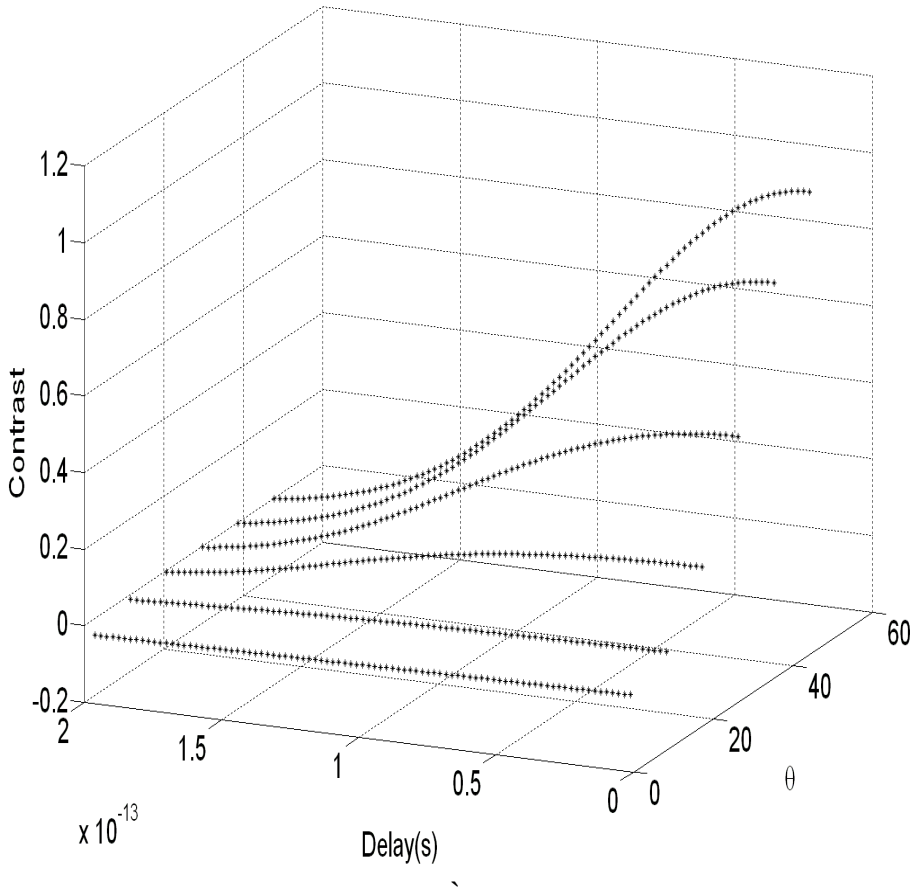

Figure 4-22 Contrast of the nonlinear fringes as a function of the delay and the angle

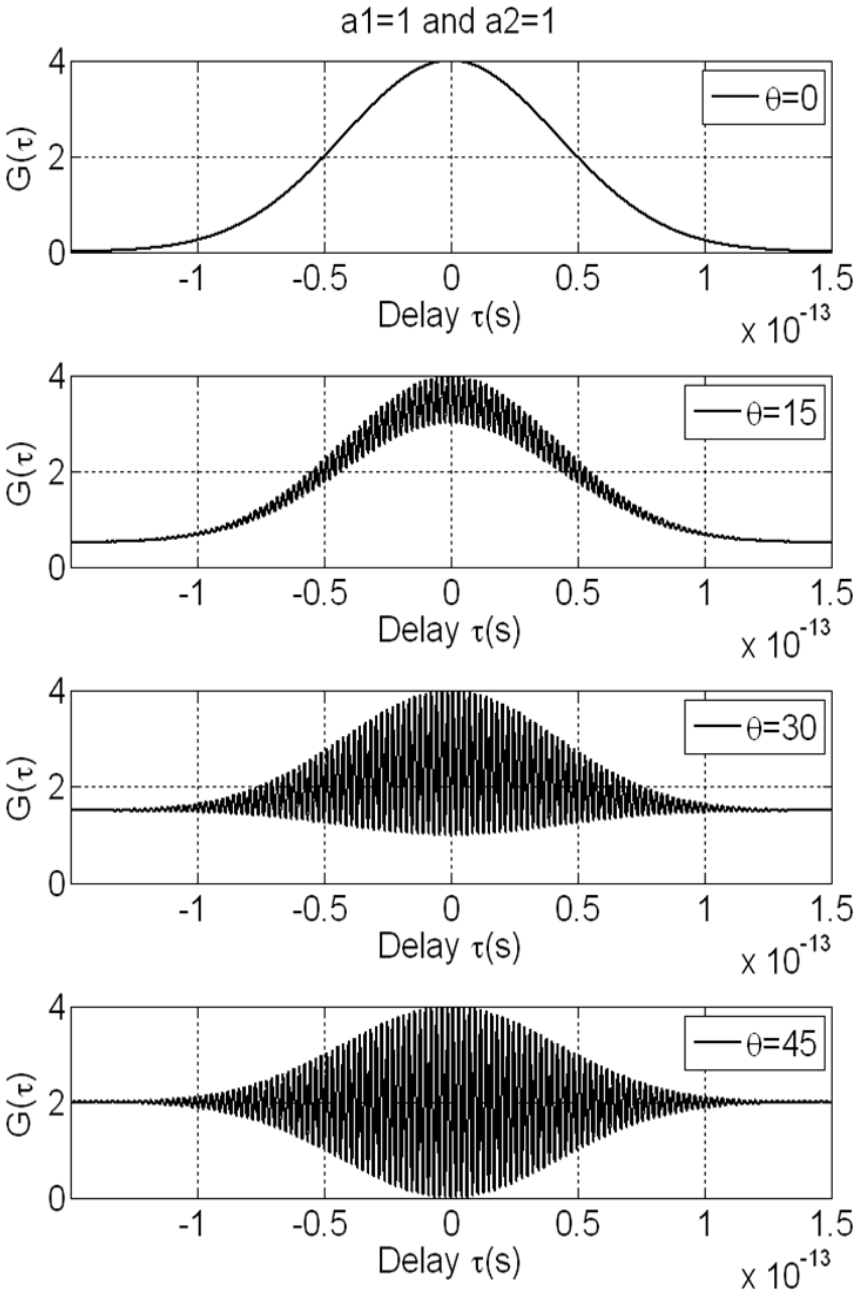

Figure 4-23 Autocorrelation function for different angles of rotation.

Balanced return field

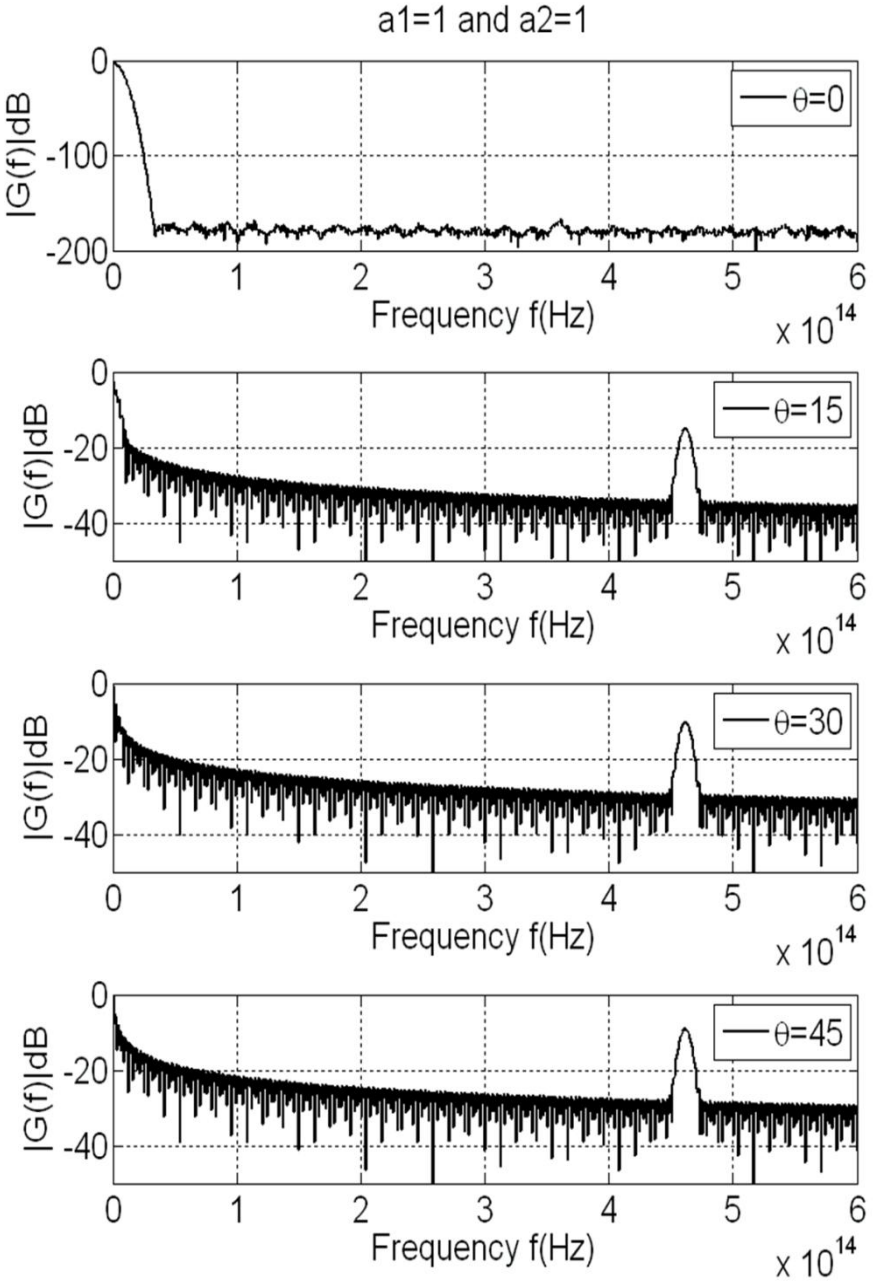

Figure 4-24 Fourier transform of the autocorrelation function for different angle. Balanced return field

In *Figure 4-25* we show the form of the fringes in this case; we observe only nonlinear fringes. Each vertical line corresponds to a nonlinear fringe with equal intensity.

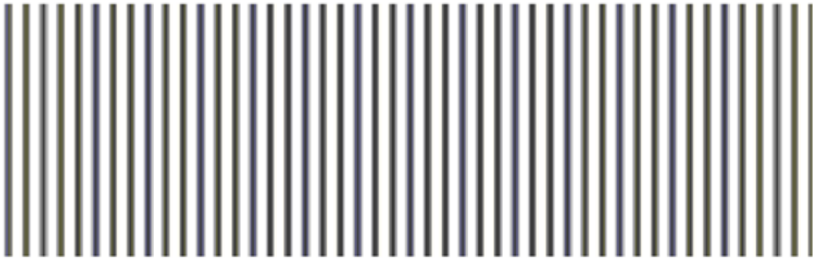

Figure 4-25 Prediction of the form of fringes for the case of balanced return field

4.3.3 Dispersion in one arm

The simulation for this consideration was based on the equation (4.34). We considered the dispersion parameters of Silicon at 1300nm wavelength [51], we have chosen a sample with a thickness $z=400\mu m$. Then we vary the dispersion coefficients h and α determined by the term $d^2n/d\lambda^2$ defined in the equation(4.31).

Figure 4-26 illustrates the second order autocorrelation function for different rotation angles when the coefficient $d^2n/d\lambda^2$ is set to $1.95*10^{12}\mu m^{-2}$. We observe a shift to the left which is due to the thickness z of the sample.

The FWHM of the autocorrelation function is now wider than before and it is estimated to 150fs; the new value depends on the parameter h defined in the equation(4.31). Note that we considered a balanced return field ($a_1=a_2=1$). Same as before, if the angle is set to zero we do not observe any fringes, and when the angle is set to 45^o we only observe nonlinear fringes with a maximum contrast. But when the angle is set to 15^o or 30^o we observe linear and nonlinear fringes.

Figure 4-27 shows the Fourier transform of the autocorrelation function presented in *Figure 4-26*. We observe only one peak when the angle is 45^o which corresponds to the nonlinear fringes. When the angle is 15^o or 30^o we observe both linear and nonlinear fringes, note that the height of the linear fringes peak is inversely related to the angle. We showed a zoom of the linear fringes peak when the angle is 15^o; we observe 3 smaller peaks which form this large peak. This is due to the mathematical expression found in (4.34) which has many envelopes, and because of the dissymmetry that comes from the presence of the dispersion in one arm only.

Nevertheless the presence of a positive chirp in the field of the sample arm, mixed with the chirp-chirp field from the reference arm was not observed in the autocorrelation function. To understand this let us look back to the first part of the linear term which contains linear fringes from the equation (4.34):

$$e^{-\frac{\alpha^2 g_2^2 l_2^2}{1+\alpha^2 g_2^4}}\left(\cos\left(m_2+\frac{\alpha l_2^2}{f_2^2}\right)\sqrt{\frac{f_2+1}{2}}-\sin\left(m_2+\frac{\alpha l_2^2}{f_2^2}\right)\sqrt{\frac{f_2-1}{2}}\right)$$

by splitting it into two factors:

- Envelope: $A=e^{\frac{-\alpha^2 g_2^2 l_2^2}{1+\alpha^2 g_2^4}}$
- Linear fringes with chirp effect:

$$B=\cos\left(m_2+\frac{\alpha l_2^2}{f_2^2}\right)\sqrt{\frac{f_2+1}{2}}-\sin\left(m_2+\frac{\alpha l_2^2}{f_2^2}\right)\sqrt{\frac{f_2-1}{2}}$$

Figure 4-28 illustrates how the modulus of these two terms looks like in the Fourier domain. The red curve corresponds to the modulus of the Fourier transform of the linear term with chirp effect (B), the black curve corresponds to the modulus of the Fourier transform of the envelope (A) and

the green one represents the modulus of the Fourier transform of the product (A.B). The chirp has disappeared in the final result.

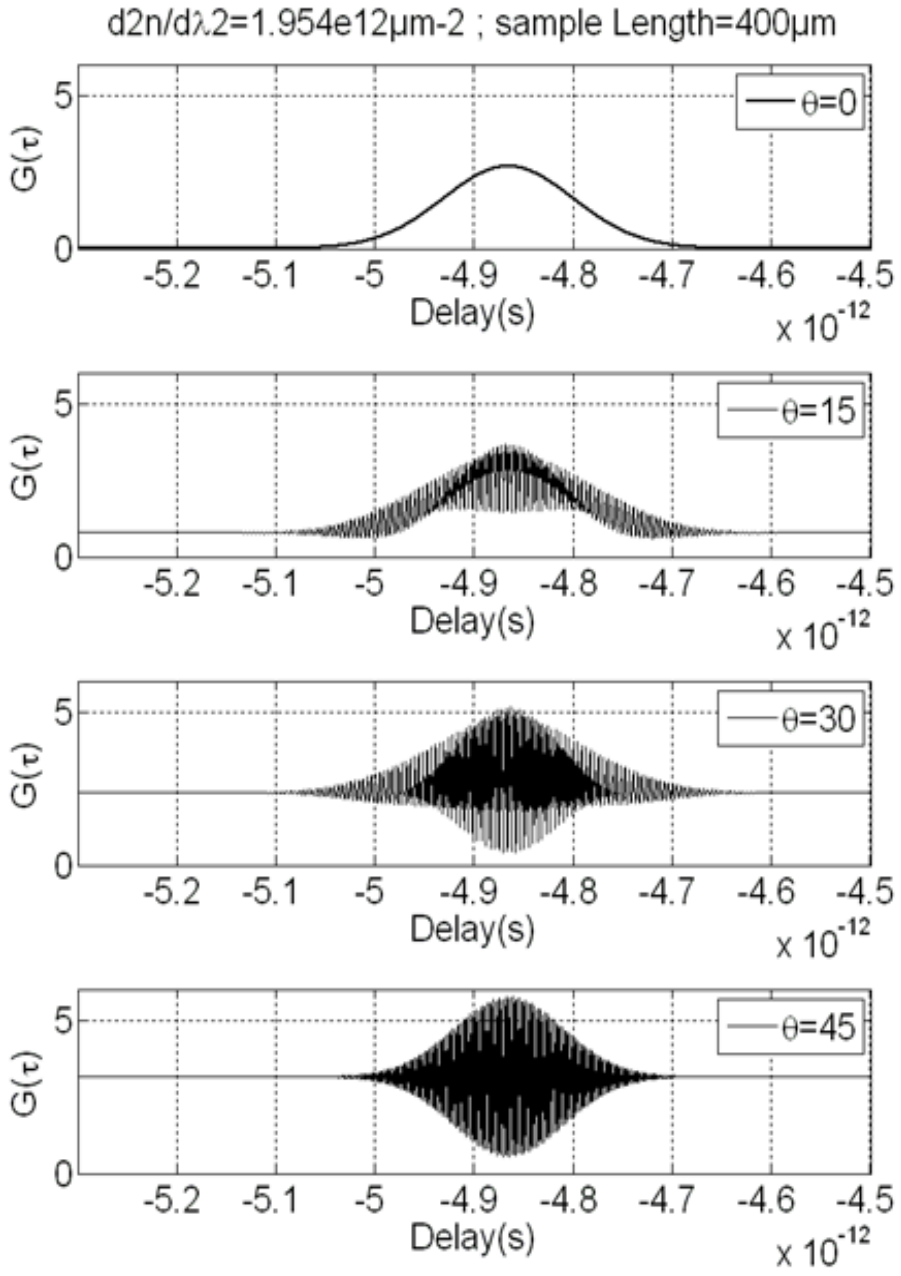

Figure 4-26 Autocorrelation function when dispersion is taken into consideration. $d^2n/d\lambda^2 = 1.95x10^{12}\mu m^{-2}$

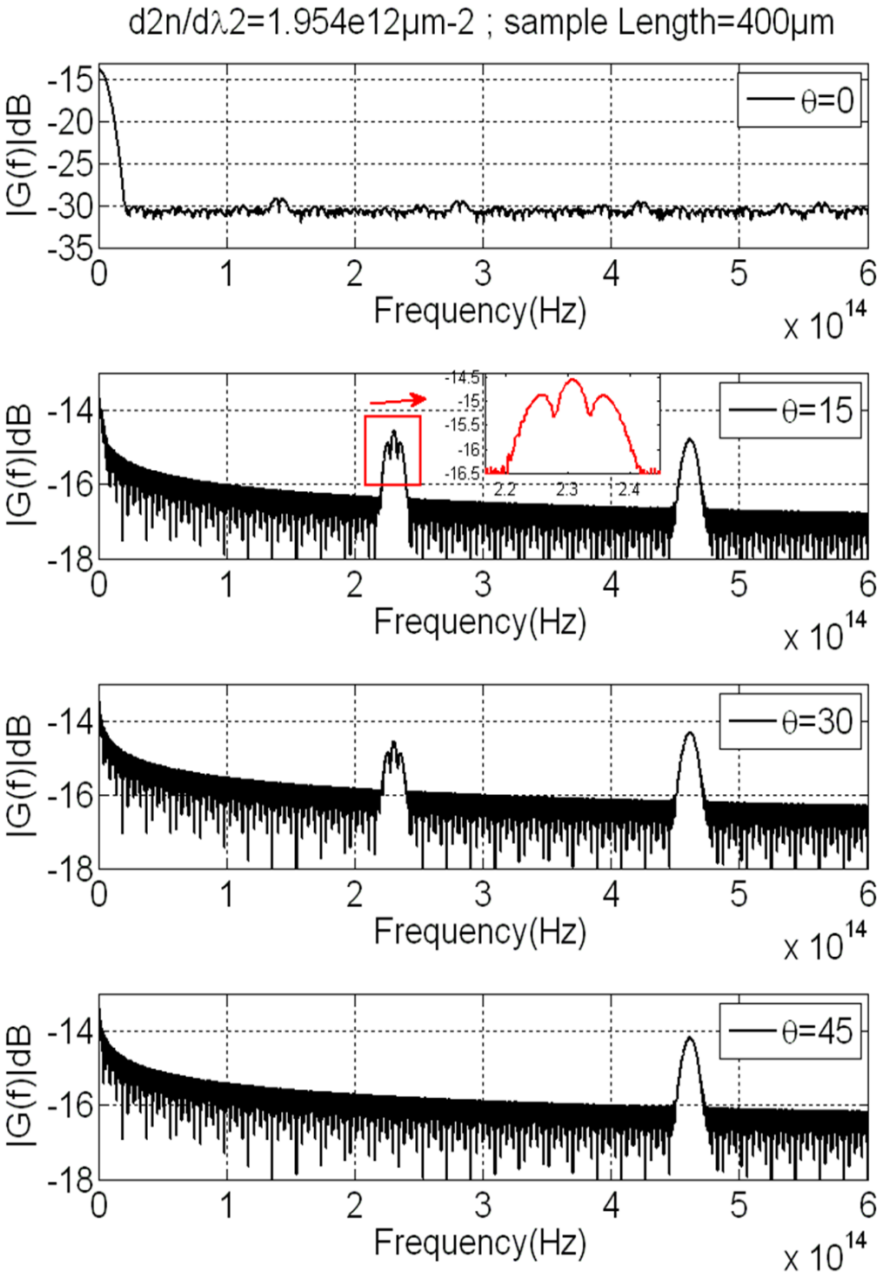

Figure 4-27 Fourier transform of the autocorrelation function when the dispersion is taken into account $d^2n/d\lambda^2 = 1.95x10^{12}\mu m^{-2}$

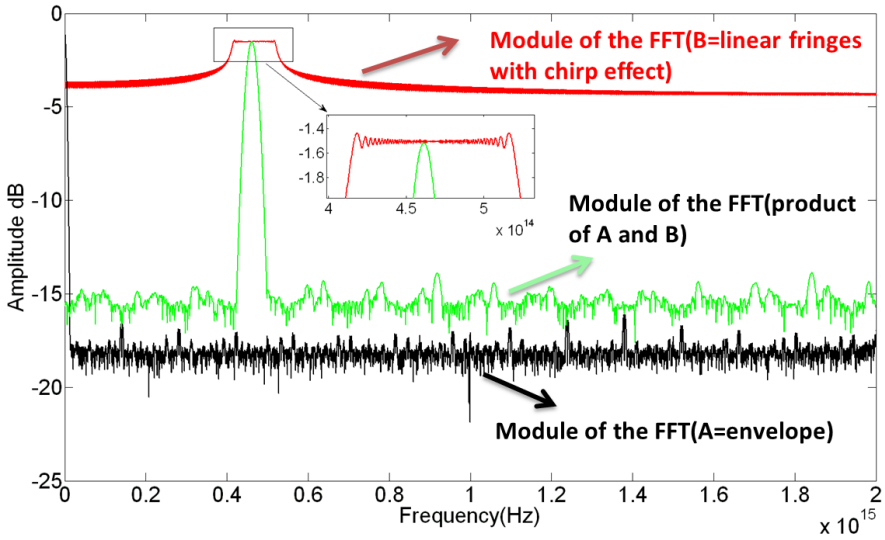

Figure 4-28 explanation of the concealing of the chirp effect.

Another simulation was made by multiplying the coefficient $d^2n/d\lambda^2$ with a factor of 10, the new $d^2n/d\lambda^2 = 1.95x10^{13}\mu m^{-2}$ μm^{-2}. In *Figure 4-29* and *Figure 4-30* we observe that the autocorrelation function becomes wider. In the previous case the FWHM was estimated around 150fs, thus now the new value is around 1200fs. The contrast of the linear fringes dominates on the nonlinear fringes presented in dB scale when the angle is 15^0 or 30^0 .We see clearly that no chirp is observed in our autocorrelation function.

We show at the end in Appendix C, an example when both unbalanced return field and dispersion are considered at the same time. The unbalanced return field will enhance the contrast of the linear fringes, see *Figure 5-46* and *Figure 5-47*.

We can conclude from above that the presence of group velocity dispersion in the sample arm is not a real issue; it will influence the presence of linear fringes even if we set the return field coefficient a_1 and a_2 to one. The contrast of linear fringes varies as a function of the rotation angle of the crystal and the dispersion coefficient.

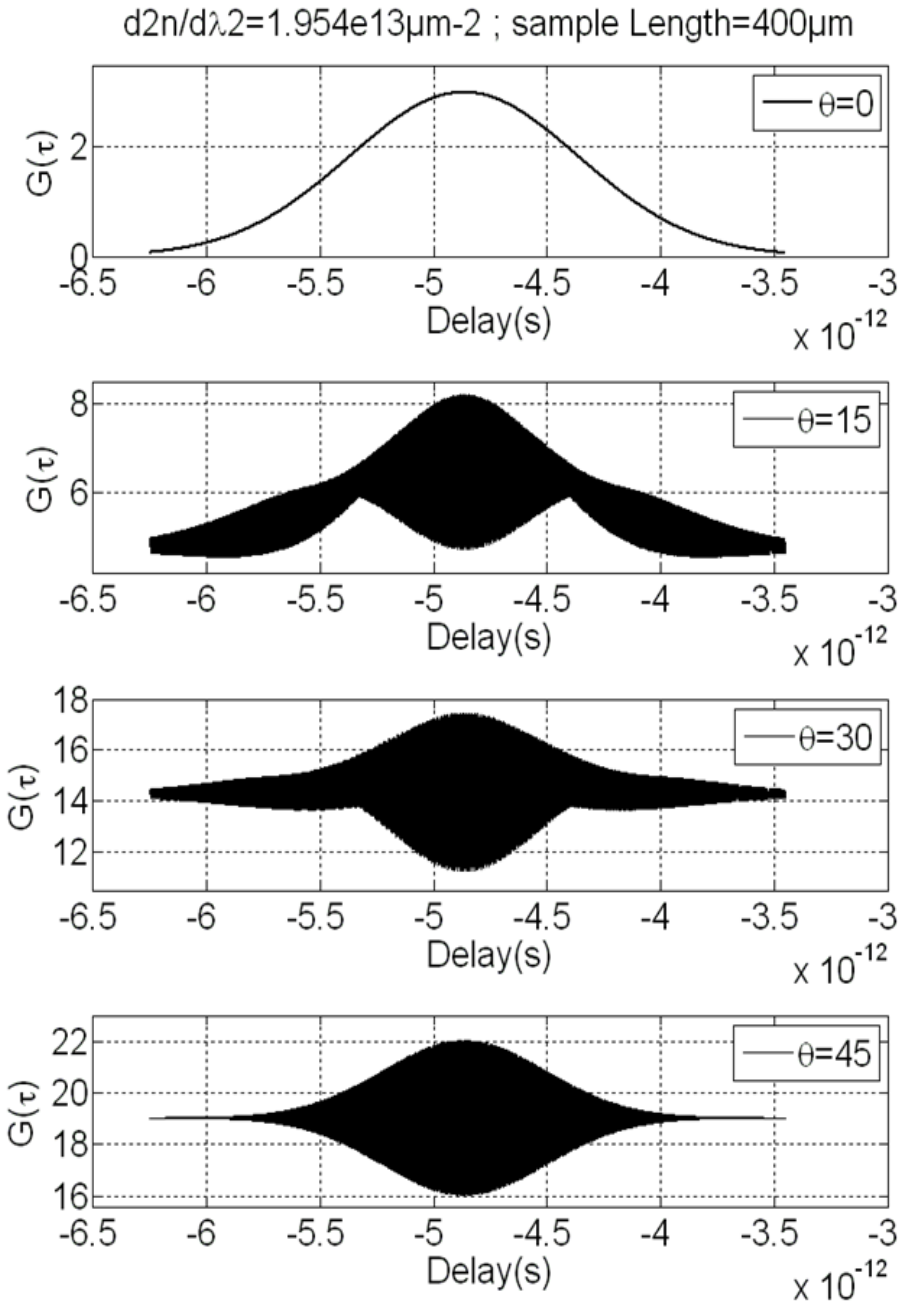

Figure 4-29Autocorrelation function when dispersion is taken into consideration.

$d^2n/d\lambda^2 = 1.95x10^{13}\mu m^{-2}$

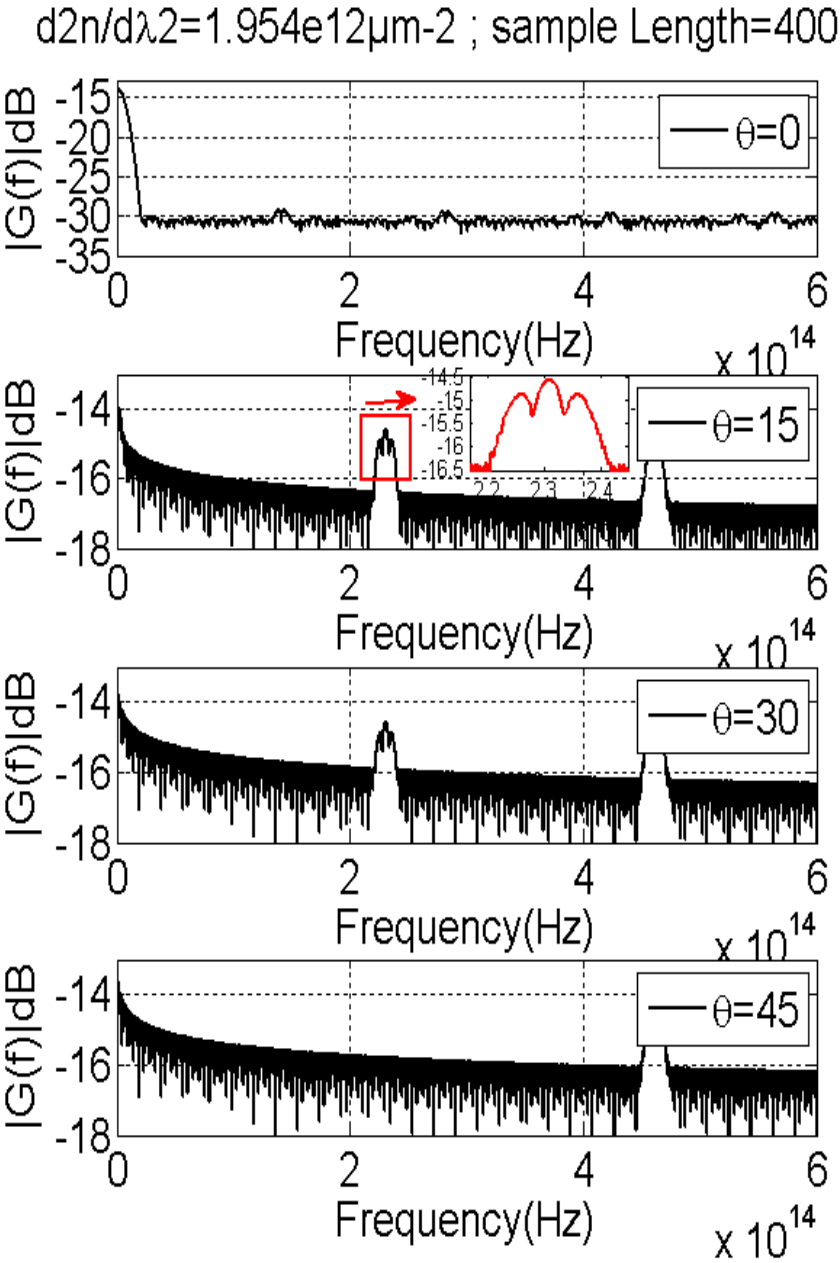

Figure 4-30 Fourier transform of the autocorrelation function when the dispersion is taken into account. $d^2n/d\lambda^2 = 1.95x10^{13}\mu m^{-2}\ \mu m^{-2}$

4.3.3 Asymmetric Gaussian pulse envelope

We define an asymmetric Gaussian [52] envelope by the following expression:

$$A_t = e^{-\frac{2t^2}{\left(\sigma+d+(d-\sigma)\tanh(t)\right)^2}} \quad (4.39)$$

Where σ and d determine the asymmetry level. Note that we have considered the approximation that the sum $\sigma + d \approx FWHM$.
Hereafter we define the level of asymmetry by

$$r_s = \frac{\sigma}{FWHM} = 1 - \frac{d}{FWHM}$$

This coefficient is always less than one, and when it is equal to 0.5 the envelope becomes symmetric, i.e. $\sigma = d$

Note that in this consideration we have performed a numerical integration based on the expression derived in(4.14).

- Balanced return fields

In this part no dispersion was taken into account; the two balance coefficients are equal to 1.

The autocorrelation function was calculated as a function of the rotation angle of the crystal and the level of asymmetry.

We started our simulation by taking the level of asymmetry equal to 0.4, we present in *Figure 4-31* the amplitude of the time pulse in this case, where we see clearly that the envelope is dissymmetric.

Figure 4-32 shows that the second autocorrelation function is symmetric, despite the asymmetry of the envelope; this is well known as a property of autocorrelations. The same conclusion stands as before, we observe a maximum contrast when the angle is 45^o and no fringes are observed when the angle is zero.

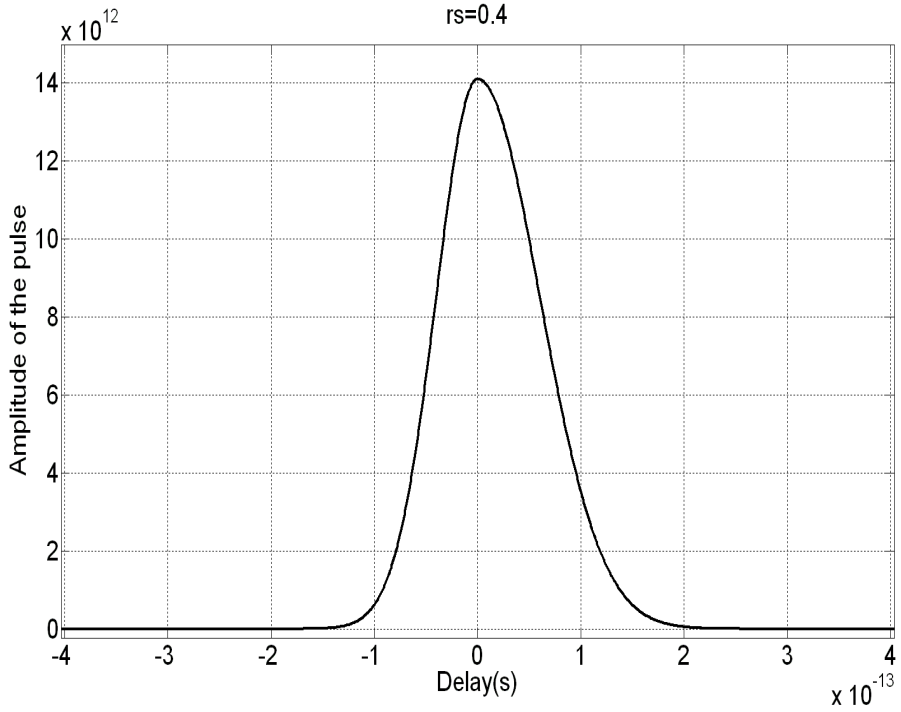

Figure 4-31 Amplitude of the field in the case of asymmetric Gaussian. The level of asymmetry is set to 0.4

Figure 4-33 illustrates the Fourier transform of the autocorrelation function in this case, we see that the linear fringes are present but not so important compared to the nonlinear one, and the amplitude decreases with the angle. When the angle is 45^{o}, we observe one peak only which corresponds to the nonlinear fringes.

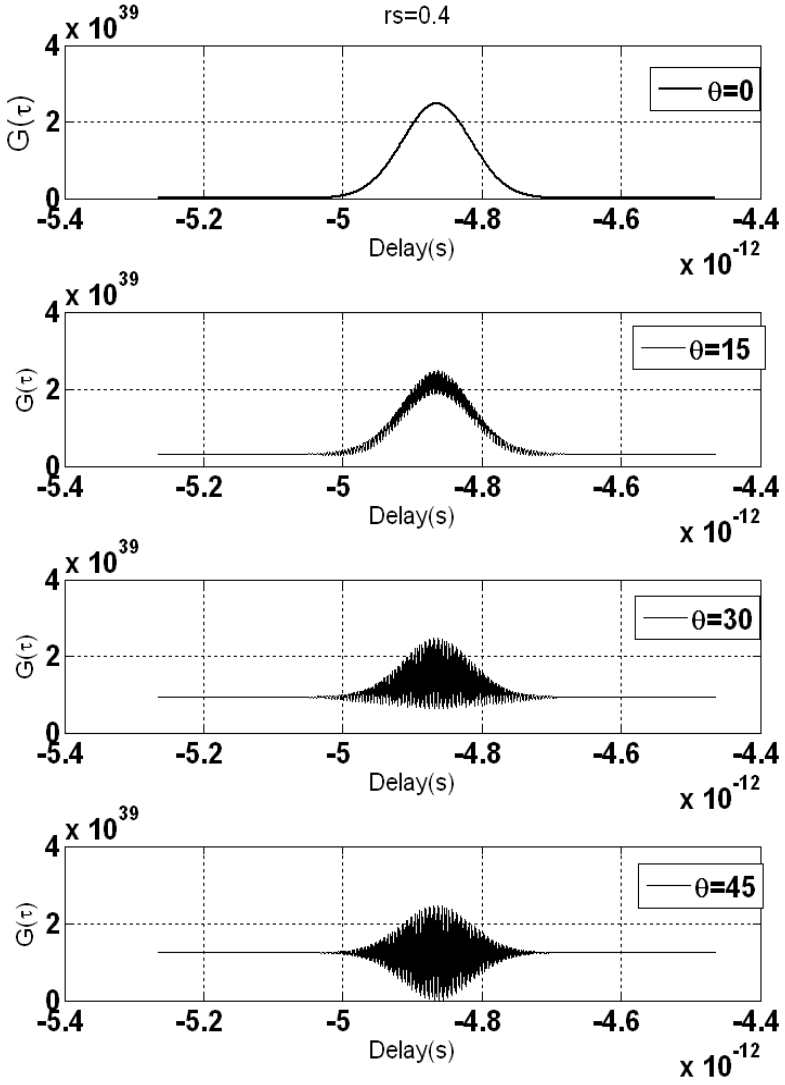

Figure 4-32 Autocorrelation function for asymmetric Gaussian envelope. r_s=0.4

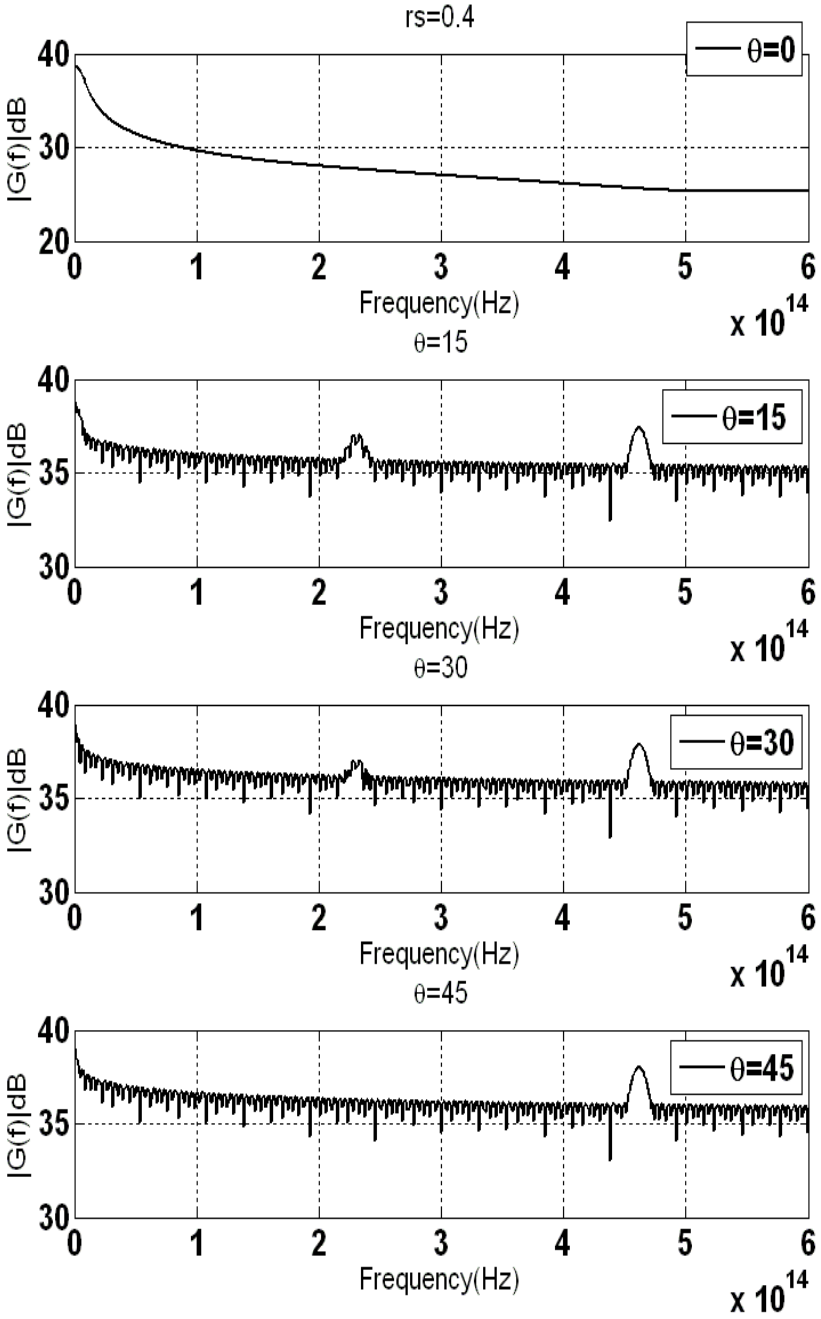

Figure 4-33 Fourier transform of the autocorrelation function, for the asymmetric envelope. r_s=0.4

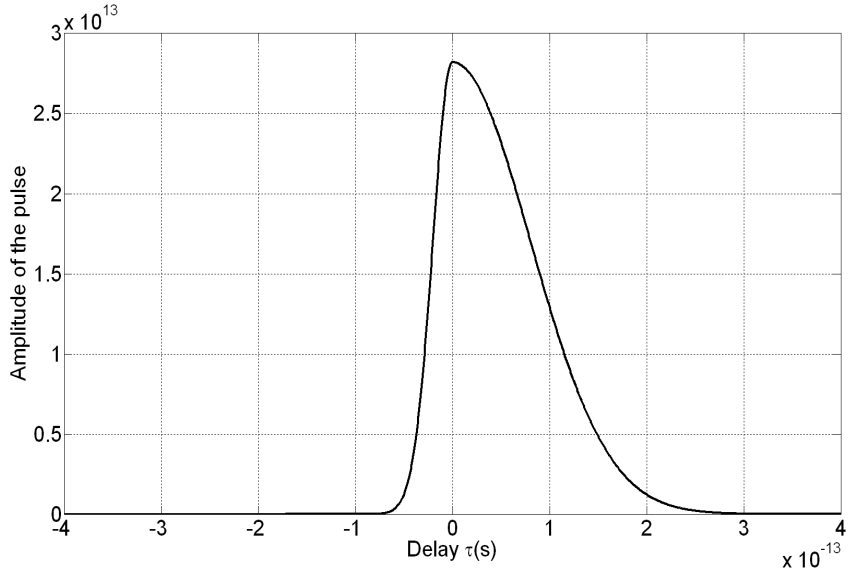

Figure 4-34 Amplitude of the field in the case of asymmetric Gaussian. The level of asymmetry is set to 0.2

Another simulation was done by changing the asymmetry coefficient *rs=0.2,* the new envelope in shown in *Figure 4-34*. We see that we have more weight on the right compared to the left; the left part is almost linear, and thus the right part appears to be the right hand side of a Gaussian.

We see in *Figure 4-35* that the autocorrelation function remains symmetric; the amplitude of the autocorrelation function at the angle zero has doubled compared to the situation when the asymmetry coefficient was 0.4. When the angle is set to 15^o or 30^o, the shape is different compared to the previous case. We see here more weight (more contrast) at the minimum level of the autocorrelation function, which is due to the presence of linear fringes with increased intensity. By looking to its Fourier transform presented in *Figure 4-36*, we see that the linear fringe peak is bigger than before, and it decreases with the angle and it vanishes completely when the angle is 45^0.

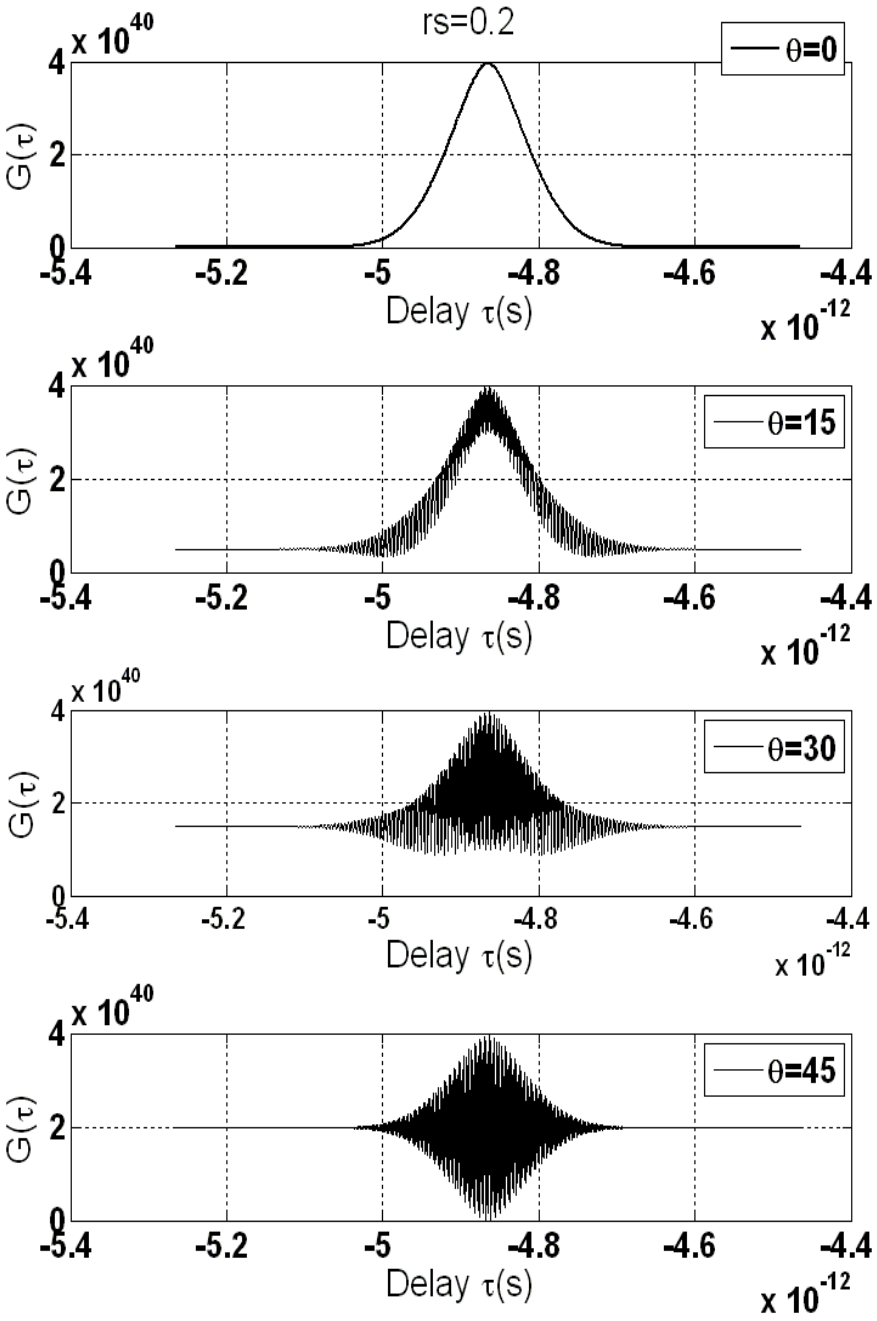

Figure 4-35 Autocorrelation function for asymmetric Gaussian envelope. r_s=0.2

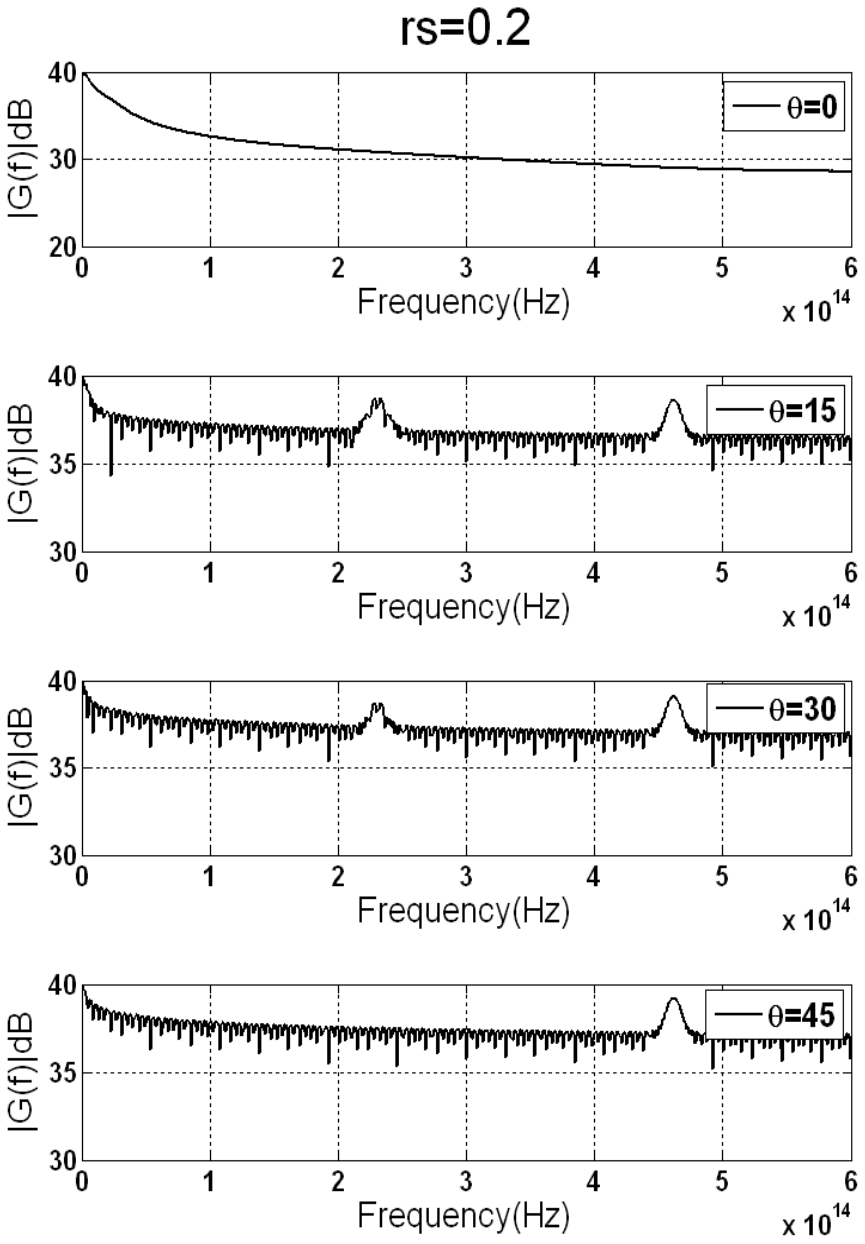

Figure 4-36 Fourier transform of the autocorrelation function for asymmetric envelope. r_s=0.2

To confirm the previous analysis, we plotted the ratio between linear and nonlinear fringes versus the level of asymmetry when the angle of the crystal is 15^o; the result is presented in *Figure 4-37*. We see that when $r_s=0.5$ we do not observe linear fringes and the ratio is zero, this is due to the fact that the envelope is symmetric for this value. But when we choose a value far from *0.5*, this ratio becomes more important, e.g. the ratio is equal to one when the level of asymmetry is set to 0.22

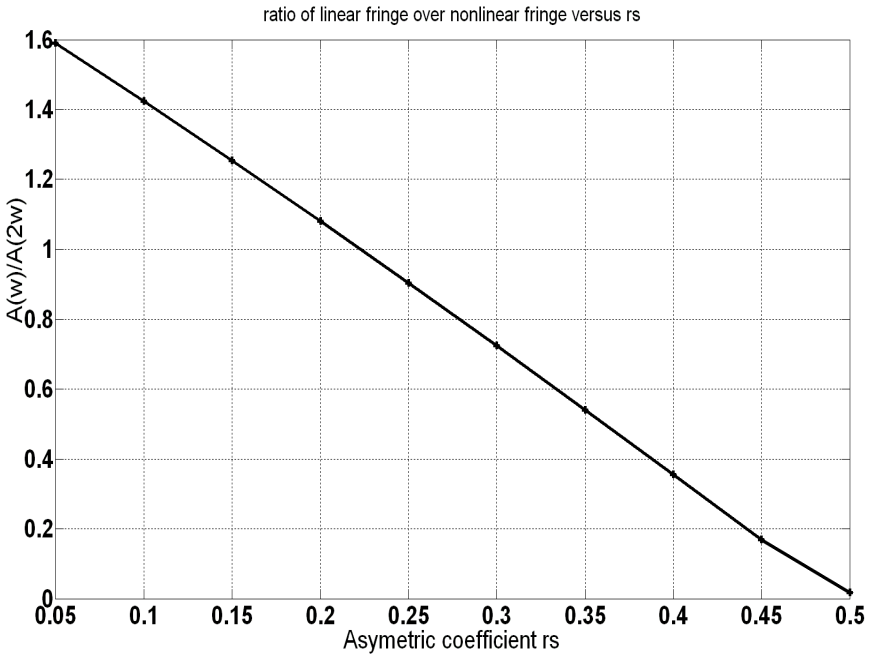

Figure 4-37 Ratio between linear and nonlinear fringes as a function of the level of asymmetry

- Dispersion is taken into account in the sample arm

The asymmetry level of the envelope was set to $r_s=0.2$, and the dispersion parameter $d^2n/d\lambda^2=1.95e12$. The results are shown in *Figure 4-38* and *Figure 4-39.*

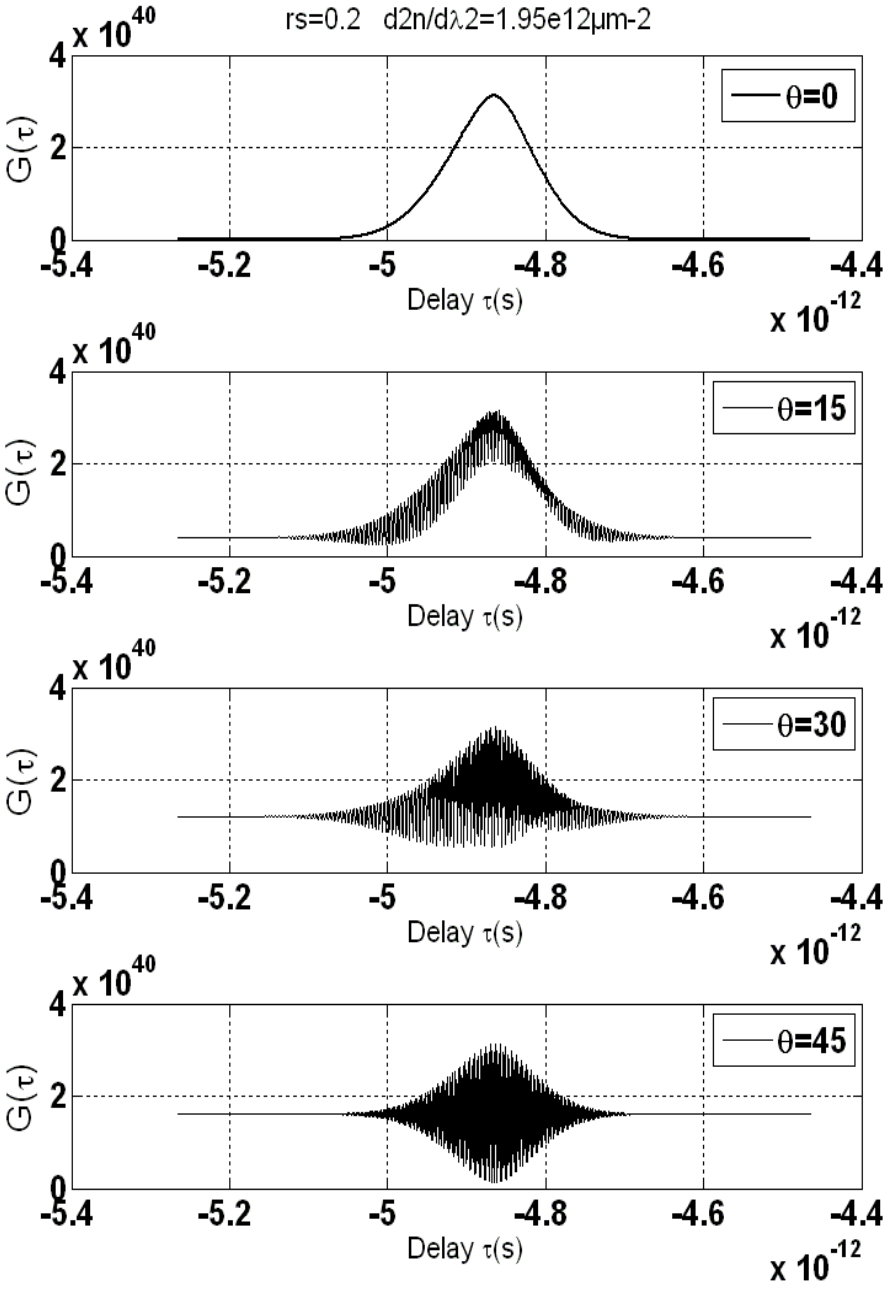

Figure 4-38 Cross-correlation function for asymmetric envelope and dispersion is taken into consideration in the sample arm.

Figure 4-38 shows that the autocorrelation function is no more symmetric compared to the previous case when no dispersion was included. By looking to its Fourier transform in *Figure 4-39* we do not see a major difference in both linear and nonlinear peak compared to the situation without dispersion in *Figure 4-36*.

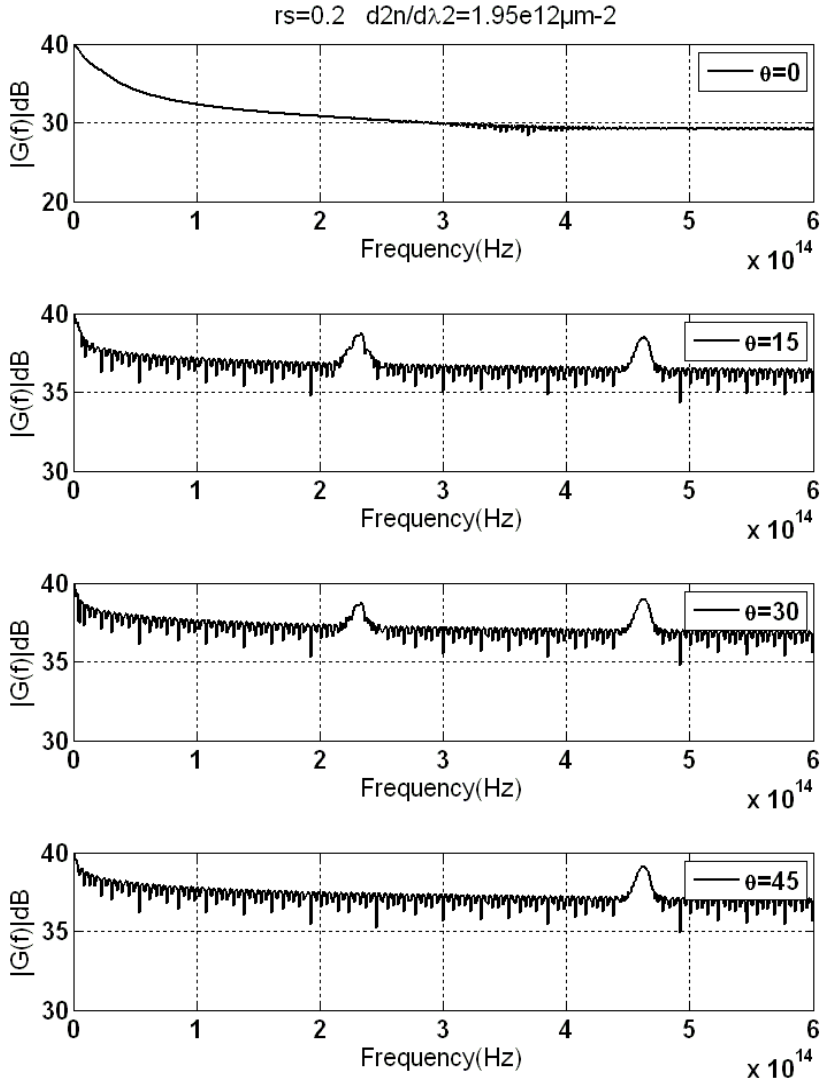

Figure 4-39 Fourier transform of the autocorrelation function for different angles. Asymmetric Gaussian + dispersion

Figure 4-40 illustrates the ratio of linear over nonlinear fringes versus the dispersion coefficient; this ratio is linearly proportional to the dispersion coefficient, e.g. this ratio is equal to one when $d^2n/d\lambda^2=6e12\mu m^{-2}$.

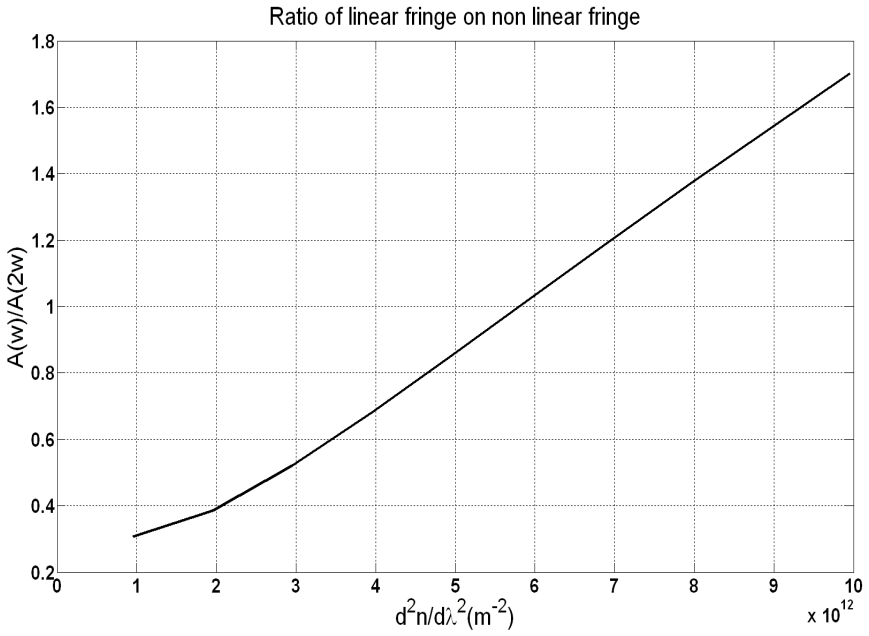

Figure 4-40 ratio between linear and nonlinear fringes versus the dispersion coefficient. Asymmetry level $r_s=0.2$

4.6 Summary

As a conclusion to this chapter, we have given a full analysis of the second harmonic generation type II interferometry using the autocorrelation technique. We have shown that in order to eliminate the DC which contributes to saturate the detector, the type II crystal must be set at the angle zero, when the two orthogonal fields which come from each arm coincide with the ordinary and the extraordinary axis. By doing so, no fringes are observed; so if we turn the crystal around the field direction we can generate

both linear and nonlinear fringes, but the DC will come back again. Linear fringe's contrast can be controlled using the balance coefficients a_1 and a_2, and it can be eliminated when these coefficients are equal. We then showed that the presence of group velocity dispersion in the sample arm or having non symmetric pulses will lead to observing linear fringes regardless of the balance coefficient. The contrast of these fringes is proportional on the dispersion coefficient and the level of asymmetry. We showed also that if we set the angle to 45^o, the linear fringes will vanish no matter what other effects are considered, while we observe the maximum self-doubling and the maximum contrast of nonlinear fringes. Nevertheless if we consider that the polarizer beam splitter has imperfect polarizations and that the extinction ratio value is not negligible it will lead to having linear fringes at the angle 45^0.

Since eliminating the DC will eliminate the fringes, alternative methods like shearing or Fizeau interferometry [53] combined with the femtosecond gated method can generate fringes and eliminate the DC at the same time. This can be done by realizing the shearing or the Fizeau fringes in the sample arm before doubling. The shearing method consists in interfering two superposed images of the object, shifted spatially. A Fizeau interferometer consists in placing two reflecting surfaces facing each other. The reflected light from the rear-surface of the transparent first reflector is combined with that reflected by the front surface of the second reflector to form interference fringes.

In the next chapter, we will show that we have adopted the Fizeau fringes in our setup for simplicity, and because our goal is to prove the feasibility of the femtosecond gated method for interferometric measurements.

5. Experimental setup and results

In this chapter, we first introduce the experimental setup used for the proof of concept, and then we describe its important elements. One of the important elements of the setup is the femtosecond laser [54-58] source, which is why the laser chain components are described briefly. We then explain the Fizeau interferometry principle [53] and we describe the sample used to generate Fizeau fringes. We later present the experimental results; some of the results concern the autocorrelation function, these results validate the dependency of the contrast of the linear or nonlinear fringes, with the rotation angle of crystal and the delay created between the two arms of the interferometer. The second part of the results concerns the metrology with the nonlinear fringes, which are generated from the Fizeau interferometer combined with the femtosecond gated method. Generating Fizeau fringes in the sample arm requires us to deal with three-wave coupling in nonlinear fringes. This why The FDOCT setup imaging system described in the first part has been used as a reference to make a comparison between fringes in linear and nonlinear optics, and verify the theory about the fringes' periodicity.

We finally present an application to measure the edge of a Nickel layer using linear FDOCT Fizeau fringes and nonlinear gating method. This application is a test of feasibility of this novel method.

5.1 Setup

We assembled a second order crossed polarized autocorrelator. A schematic of the experimental setup is shown in *Figure 5-1*. The

femtosecond pulsed laser beam passes through a half-wave plate, which will rotate its linear polarization and thereby control the two coefficients a_1 and a_2 of the field in each arm. The beam is then separated in the two arms of the interferometer by a polarizing beam splitter (PBS). At the exit of the PBS, the two beams will pass through a quarter-wave plate. The initial linear polarization becomes circular at the exit of the plate.

The first beam will then probe the sample (mirror mounted on a piezo) with a circular polarization; when it travels back through the quarter wave plate, its polarization becomes linear and orthogonal to the incoming polarization. The PBS will work like a mirror (while it was a transmitter at the entrance). In the other arm, we have the same phenomenon where the beam is reflected by a fixed mirror, and after its second passage through the quarter wave plate, the polarization becomes orthogonal to the incoming polarization and the PBS will therefore act like a transmitter (while it was mirror at the entrance).

The two beams are then recombined and, cross a biconvex lens. This lens focuses the photons on the BBO doubling crystal. The light comes in at 800nm (resp. 1300nm) wavelength, thus the light will exit the crystal at 400nm (resp. 650nm) wavelength. There will be second harmonic generation only if the two pulses arrive synchronously on the BBO type II crystal. This beam passes through an infrared-blocking filter which transmits only the doubled radiation and is then captured by a photo detector.

Two types of femtosecond lasers have been used in our experiments. The reason is that the laser at our disposal in UCL has *800 nm* wavelength and the autocorrelation experiment did not require the *1300 nm* wavelength. The experiments with silicon using Fizeau fringes had to be done in the University of Vigo in Spain where a *1300 nm* fs laser was available.

In order to observe the autocorrelation function we used a modular piezoelectric actuator (Thorlabs DRV181) with a resolution of *20 nm* and a

travel distance of 80 microns. We acquired the data using a digital oscilloscope (Tektronix DSO X 3104), which can export up to 65000 points. And we used the nonlinear BBO type II crystal with the following tensor:

$$d = \begin{pmatrix} 0 & 0 & 0 & 0 & 0.08 & 2.2 \\ 2.2 & -2.2 & 0 & 0.08 & 0 & 0 \\ 0.08 & 0.08 & 0 & 0 & 0 & 0 \end{pmatrix}$$

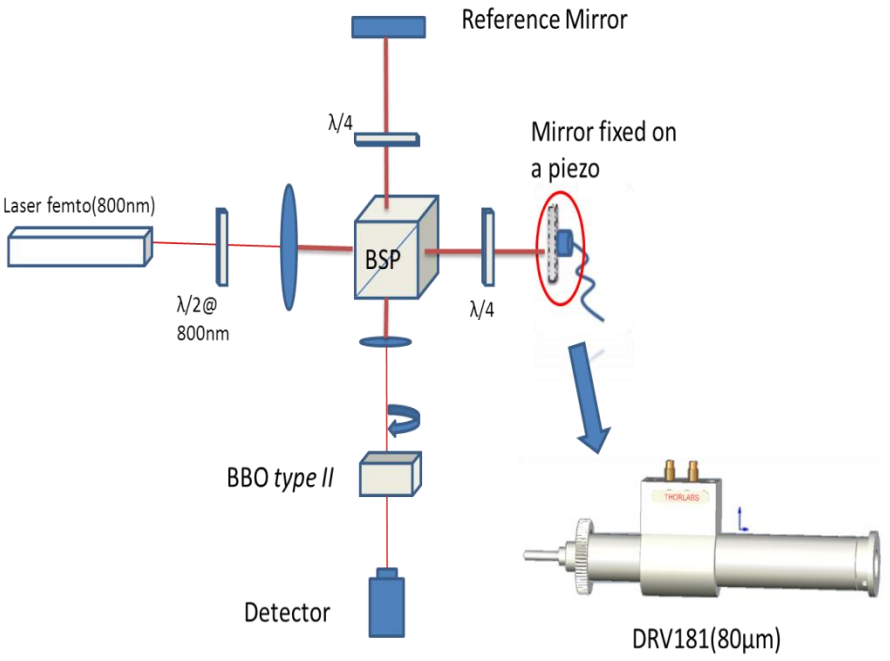

Figure 5-1Experimental setup for nonlinear fringe measurements as a function of the rotation angle of the crystal

5.2 Femtosecond laser

The mechanism of a laser is based on stimulated emission. The

interaction between a photon with an atom in an excited state results in creating a new photon after de-excitation of the atom. This new photon has the same frequency, phase, polarization and direction as the incident photon. In the presence of an active medium for the stimulated emission, a pumping process to favor a population inversion inside an optical cavity, will generate lasing if the gain of the active medium resulting from the round trip is larger than the round-trip losses of the cavity.

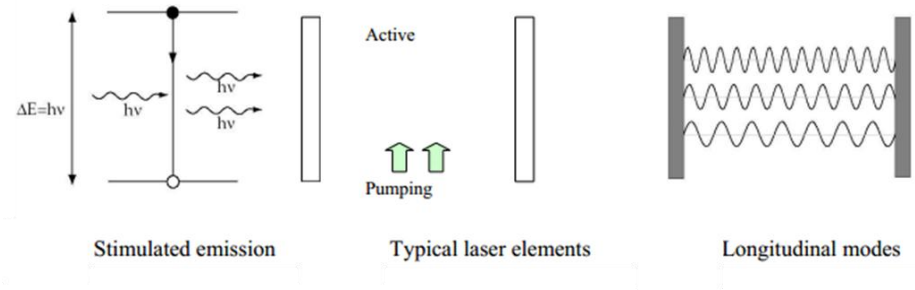

Figure 5-2 On the left: The stimulated emission principle. On the right: The different modes in a laser cavity

The oscillation of the laser may result in more than one longitudinal mode at the same time, in other words the output of the laser contains then a number of frequencies, see *Figure 5-2*. These frequencies verify the boundary condition where the cavity length is an integer multiple of half wavelength. We can write:

$$f_m = m.\frac{c}{2L} \tag{4.40}$$

Where *m* is an integer, L is the cavity length, and c is the speed of the light. In common multi-mode lasers, each mode has a random phase and will oscillate regardless of the others. The resulting fields of each oscillating mode gives rise to a noise-like output, due to constructive and destructive interference between these modes, see *Figure 5-3*. On the other hand if we

control the phases of these modes, we can obtain a more effective output; this technique is called the mode-locking.

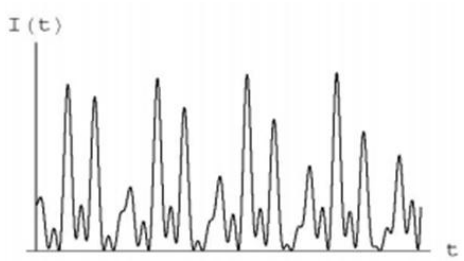

Figure 5-3 Fluctuating output of a multi-mode laser.

5.2.2 Mode locking

When the phases of the multi-mode laser are chosen to be fixed in a way to obtain a constructive interference at a specific moment and a destructive interference at other moments, the laser output will perform as a pulse train. By considering equal amplitude for each mode and locked phases, the resulting field is:

$$E(t) = \sum_{q=-N}^{N} E_0 e^{j\left[(\omega_0 + q\Delta\omega)t\right]} = E_0 e^{j\omega_0 t} \sum_{q=-N}^{N} e^{jq\Delta\omega t} \tag{4.41}$$

Where E_0 represents the amplitude of each mode, ω_0 is the angular frequency of the central mode, $\Delta\omega$ is the spacing frequency between modes, q is the order of the mode.

Note that we have a geometrical progression sum; the intensity is calculated from the electromagnetic field for *2N+1* modes in phase:

$$I(t) \propto \left|E(t)\right|^2 = E_0^2 \frac{\sin^2\left[\left(N+1/2\right)\Delta\omega t\right]}{\sin^2\left(\Delta\omega t/2\right)} \tag{4.42}$$

The intensity function is periodic, the period is given by $T = 2\pi / \Delta\omega$; the pulse duration is approximated by $\Delta t \approx 2\pi / (2N+1)\Delta\omega$. We show in *Figure 5-4* and *Figure 5-5* the output intensity versus time for different values of N.

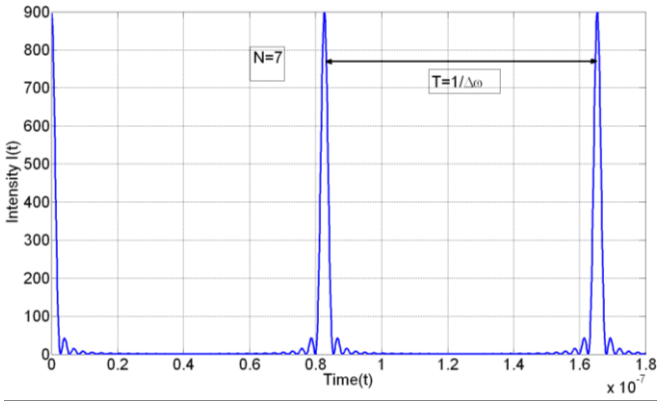

Figure 5-4 the output intensity versus time, the number of modes is 15

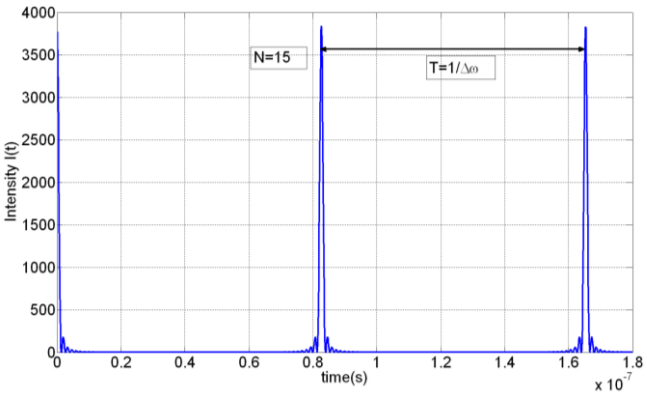

Figure 5-5 the output intensity versus time, the number of modes is 31

Let us suppose now that the oscillating modes have non-equal amplitude. It is convenient to suppose that these amplitudes have a Gaussian distribution, the resulting field expression becomes:

$$E(t) = e^{j\omega_0 t} \sum_{q=-n}^{q=n} E_q e^{jq\Delta\omega t} \qquad (4.43)$$

The sum can be calculated as an integral, we obtain:

$$E(t) = e^{j\omega_0 t} \int E_q e^{jq\Delta\omega t} dq \tag{4.44}$$

The integral in this expression is a Fourier transform. Since E_q is a Gaussian distribution, the output intensity will be also a Gaussian, and we obtain:

$$I(t) \propto \left|E(t)\right|^2 \propto \exp\left(-t^2/\Delta t^2\right) \tag{4.45}$$

where Δt represents the duration of the pulse at half maximum.

5.2.2 Laser chain

The equipment of a powerful infrared femtosecond laser is very complex. The light must travel across many optical elements before having the mid-infrared wavelength. I would give a brief description on the operation of this laser. The different modules that compose the femtosecond laser system of Vigo are presented in *Figure 5-6*.

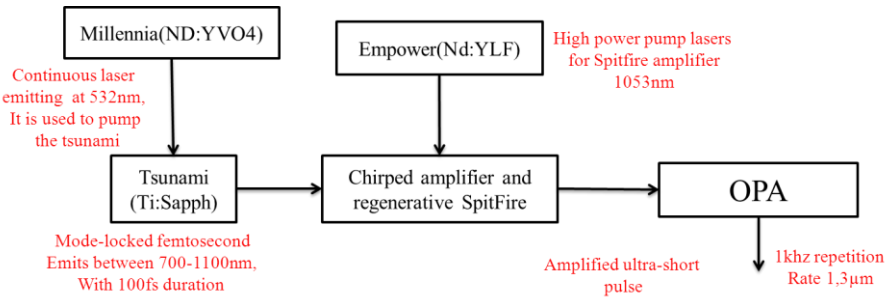

Figure 5-6 diagram of the femtosecond laser chain

- Millennia pump laser

This module includes a resonant laser cavity, a crystal doped with Nd:YVO4 and a doubling crystal (LBO). *Figure 5-7* illustrates the diagram of the inside of the pump laser. The optical source Millennia consists of diode laser arrays which penetrate in a series of fiber optics. These fibers will be combined together to be sent into the cavity. In this cavity, the laser beams are focused on the crystal Nd:YVO4 which absorbs the light of the diode laser; as a result the crystal will provide a very intense continuous radiation, and the emitted light will be amplified by the stimulated emission to generate a radiation at *1064 nm*. The LBO crystal in the upper cavity will convert this radiation into green light at *532 nm*.

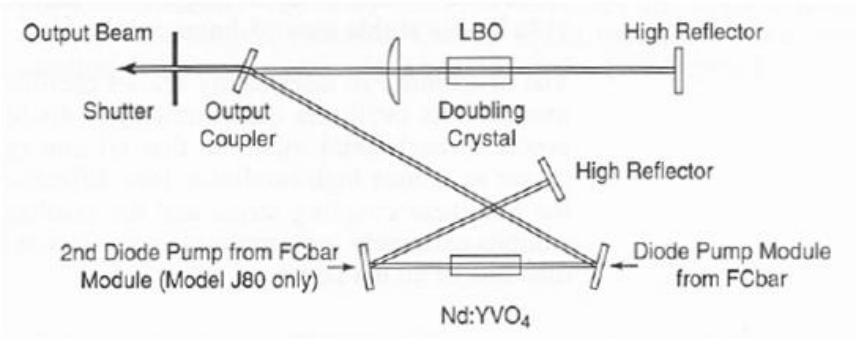

Figure 5-7 Schematic inside the unit Millennia [54]

- Tsunami laser oscillator

Titanium Sapphire crystal

The crystal used for short pulse lasers is the sapphire crystal doped with Titanium (Ti^{3+}:Al_2O_3) which has a very wide emission band between *700 nm* and *1100 nm*. It is a very solid refractory material with excellent thermal conductivity.

Mode locking

The mode locking is due to nonlinearities of Kerr effect in the laser crystal. In fact, when the power density increases in the cavity, and thus in the crystal, a nonlinear variation of its refractive index appears [55]:

$$n = n_0 + n_2 I \tag{4.46}$$

Where n_0 is the refractive index of the crystal, n_2 its nonlinear index and I is the intensity of the light pulse.

From this equation and knowing that a Gaussian beam has a non-uniform intensity distribution, the refractive index will change across the beam profile; for example it is bigger in the center of the beam than at the edge. This effect can be linked to an autofocusing convex lens which will modify the spatial profile of the beam. In other words the beam diameter is smaller in pulsed mode compared to continuous mode. If we place a collimator in the cavity whose aperture is smaller than the diameter of the continuous beam but larger than that of the pulsed beam, it will attenuate a lot the continuous mode and very little the pulsed one. So by favoring the latter regime the laser will operate in a pulsed manner. Therefore the laser can switch to a system of short pulses when the nonlinear Kerr effect is exploited.

Description of the laser cavity

Figure 5-8 represents the cavity of the laser oscillator using Kerr Lens Modelocking (KLM). The cavity consists of a crystal, four prisms, mirrors and a spatially selective collimator for the intracavity profile beam selection.

The light that comes from the pump laser Millennia enters the oscillator and is reflected by a series of mirrors through the Ti:Sapphire crystal. The emitted photons from the crystal are directed using mirrors towards the resonant cavity, and then penetrate in a series of prisms to compensate the group velocity dispersion, introduced by the passage of the pulses through refractive materials and multi-layer coatings. A tuning slit is inserted between the prisms to adjust the wavelength. To initiate the pulsed mode, the beam passes through an acousto-optical modulator to generate a temporal modulation. Just before the output, the laser beam passes through a beam splitter that sends part of the beam towards a photodiode coupled to an electronic driver, for the control of the laser. Finally, the laser beam enters a Brewster window to exit the laser cavity [57].

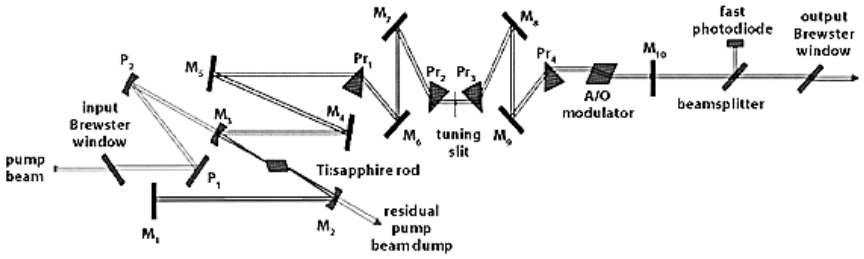

Figure 5-8 Scheme of the Tsunami [56]

- Pump Laser Empower

This laser is based on Nd: YLF crystal. Diode lasers pump the crystal; the electrons of neodymium atoms are excited and emit laser light at 1053nm. The mirrors in the laser cavity have a very high reflectivity for this wavelength. The inside of the laser Empower is shown in *Figure 5-9*.

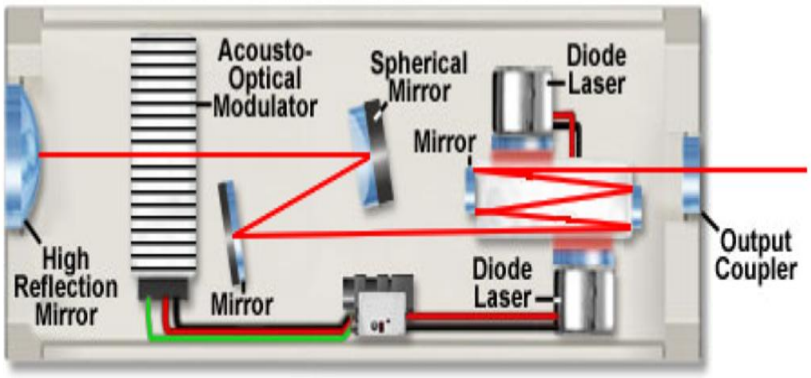

Figure 5-9 scheme of the Empower laser[58]

An acousto-optical modulator is a block of fused silica which acts as phase diffraction grating when vibrating at a frequency close to the ultrasonic. We use here the diffraction phenomena of the light by a sound wave in order to create pulses. The ultrasonic wave is generated by a piezoelectric sensor.

- Chirped amplifier and regenerative SpitFire

To amplify ultra-short laser pulses, a CPA (Chirped Pulse Amplifier) is used in general. In this type of amplifier, see *Figure 5-10*, the pulse from the oscillator is, first extended temporally using a stretcher (a combination of gratings). Then it is amplified in Ti-Sapphire power amplifier. The resulting pulse will pass through another combination of grating to be recompressed. The evolution of the pulse shape during the process is shown in *Figure 5-10.*

The reason for the temporal broadening of the pulse is to avoid nonlinear effects in the amplification, to limit excessive power and finally avoid too fast passage of the pulse in the amplifier medium that would not benefit from all the available gain therein.

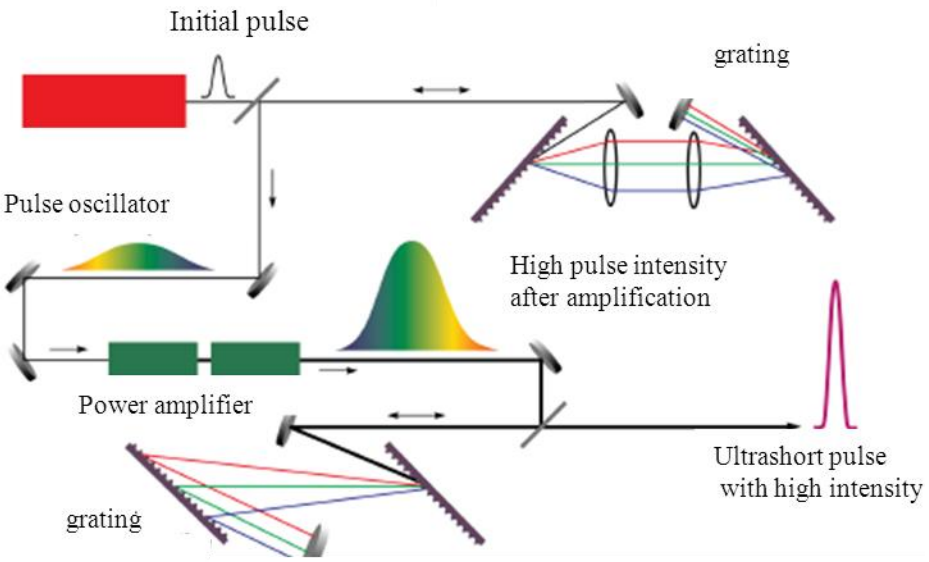

Figure 5-10 Example of an amplifier device with chirped frequency

- OPA parametric amplifier

At the output of the SpitFire, the pulses will be used to pump a parametric amplifier and thus to produce pulses with adjustable wavelength. The OPA consists of a Sapphire crystal, a BBO non-linear crystal and a multipass cavity.

The 800nm beam in OPA is divided into three beams using two beam splitters. The first portion of the beam (less than 5% of the initial intensity) is focused on the Sapphire crystal and will produce a continuous white light. The second portion of the *800 nm* beam (which is about 15% of the initial intensity) is mixed with white light in the BBO crystal, resulting in an amplification of a region of the white light spectrum. The BBO crystal orientation will determine the wavelengths of the white light that will be

amplified. The near infrared light produced is amplified when mixed with the remainder of the *800 nm* beam in the BBO crystal at the second passage.

The principle of the parametric amplifier is based on a principle very different from that of the laser. The gain of an OPA comes directly from a nonlinear interaction.

5.3 Thin air wedge sample and Fizeau principles

A thin air wedge is formed by two reflective plates, placed one upon another so they touch at one side, and are separated by a thinner object on the opposite side, see *Figure 5-11*.

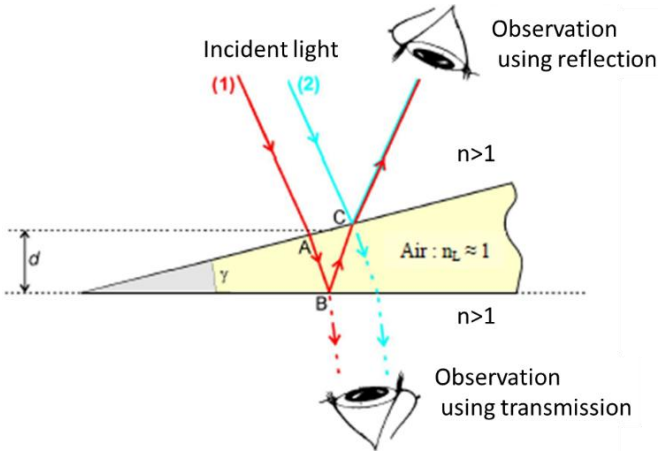

Figure 5-11 thin air wedge

Hereafter, only the simplified case of a perpendicular incident light is considered. The normal incident light is divided into two parts, one part is reflected by the upper plate surface and the other part goes through to reach the lower plate surface where it is reflected.

The geometrical path difference for normal incidence is:

$$\Delta S_{geom} = 2n_L.d = 2d$$

where n_L=1.

Since the air layer is very thin, we can consider that $AB \cong BC \cong d$, where d is the thickness of the air layer.

Observation using reflection

Since the light at the point B is reflected from a higher refractive index to a lower refractive index, we should add a half wavelength (*180°* phase change) to the path difference. The final path length is therefore:

$$\Delta S_{opt} = 2d \pm \lambda/2 \qquad (4.47)$$

Constructive interferences are observed if:

$$\begin{aligned} &\Delta S_{opt} = k.\lambda \ (k = 0,1,2,3...) \\ &\Rightarrow 2\,\mathrm{d} \pm \frac{\lambda}{2} = k.\lambda \qquad (4.48) \\ &d_k = (2k+1).\frac{\lambda}{4} \ (k = 0,1,2,3...) \end{aligned}$$

Destructive interferences are observed if:

$$\begin{aligned} &\Delta S_{opt} = (2k+1).\frac{\lambda}{2} (k = 0,1,2,3...) \\ &\Rightarrow 2\,\mathrm{d} \pm \frac{\lambda}{2} = (2k+1).\frac{\lambda}{2} \qquad (4.49) \\ &d_k = k.\frac{\lambda}{2} \ (k = 0,1,2,3...) \end{aligned}$$

The first dark fringe (destructive interference when *k=0*) is located at the edge of the corner, if the interferences are observed by reflection. The difference between two consecutive dark fringes (resp. bright fringes) is : d_{k+1}-d_k=*λ/2*.

5.4 Results and validation

5.4.1 Contrast of the Michelson Nonlinear fringes versus the angle for Balanced return field

This experiment validates the simulations presented in *Figure 4-23*. We used the setup described previously in *Figure 5-1*. The femtosecond laser at UCL with *800 nm* central wavelength has been used in this setup.

The interferometric signal is observed by a Silicon PIN photo-detector [59]; this latter has an active area of *13* mm^2, a wavelength range from *350* to *1100 nm* with peak sensitivity at *970 nm*, a rise time of *14 ns* and an output voltage between 0 to *10V* . Choosing different angles for the crystal, we obtained results shown in *Figure 5-13*,*Figure 5-14*, *Figure 5-15* and *Figure 5-16*. These measurements were done by scanning periodically at low frequency back and forth, a mirror fixed on the Thorlabs (DRV181) piezo actuator. This scanning creates the delay between the pump and the probe pulses; as expected the contrast of the nonlinear fringe is a function of the angle.

When the angle is set to zero, see *Figure 5-12*, the field E_1 (resp.E_2) that comes from each arm is oriented along the ordinary axis (resp. extraordinary axis), therefore we do not observe interference. By turning the crystal, E_1 (resp. E_2) is decomposed into two components E_{1o} and E_{1e} (resp. E_{2o} and E_{2e}), along each axis. Decompositions of the field between E_{1o} *and* E_{2o} (resp. E_{1e} and E_{2e}) must first be done respectively to the ordinary and extraordinary, before type II wave-mixing. As a result the doubled signal will contain self and non-self-doubling components. When the angle is set to 45^o we observe a maximum intensity for self-doubling and the maximum contrast for the nonlinear fringes.

The FWHM of the autocorrelation function is around *100 fs*, and it is determined from *Figure 5-13*. Despite that the angle in this measurement is 0^o, we observed some fringes; this comes probably from not choosing perfectly the angle zero since the angle of the crystal is chosen each time manually using a mechanical system, or maybe it comes from the improper orientation of the crystal.

In *Figure 5-14* we present a zoom to show the interference fringes, the distance between two adjacent consecutive minima is *400 nm* which corresponds to the half of central wavelength used in our setup.

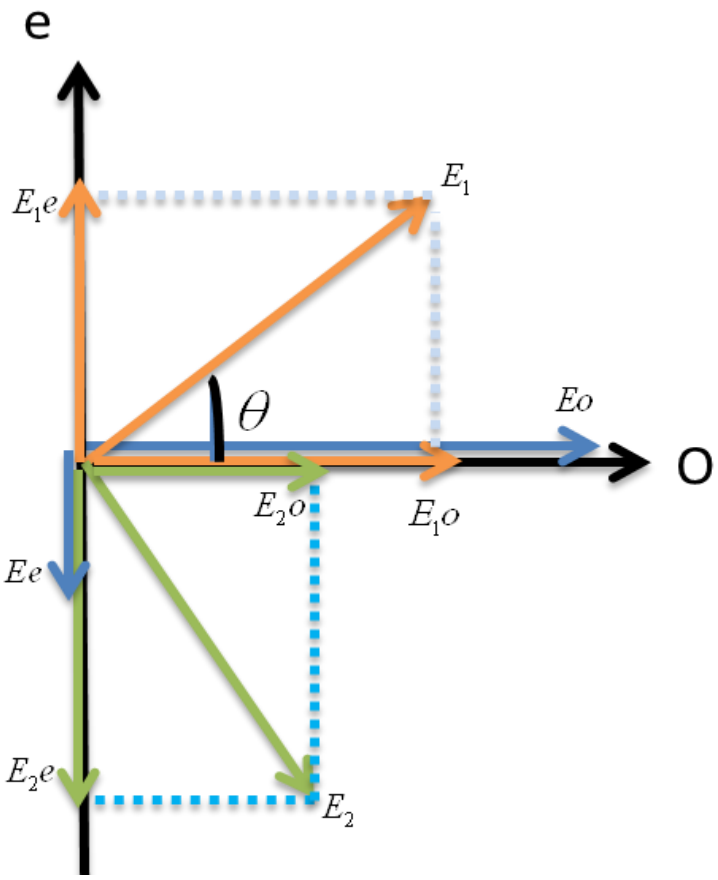

Figure 5-12 the direction of the two orthogonal fields and their components when we turn the crystal

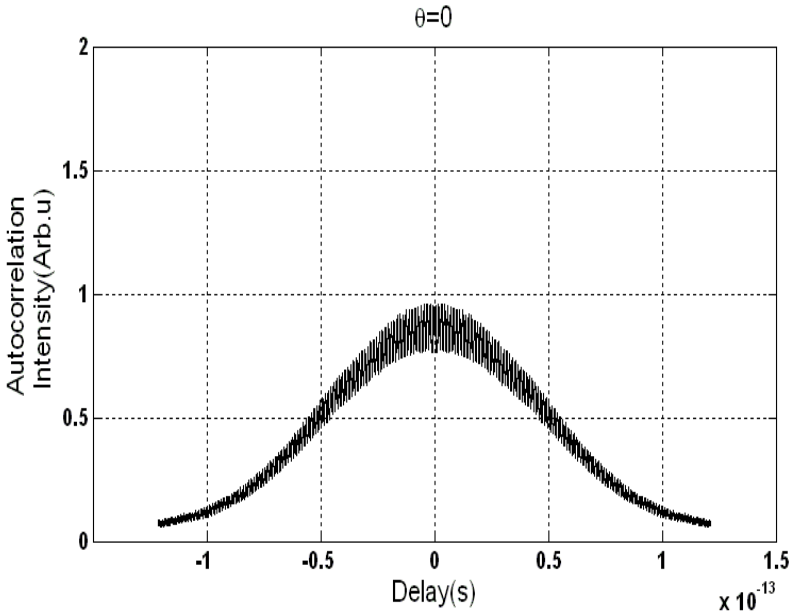

Figure 5-13 Autocorrelation function when the angle is set to zero (Balanced return field)

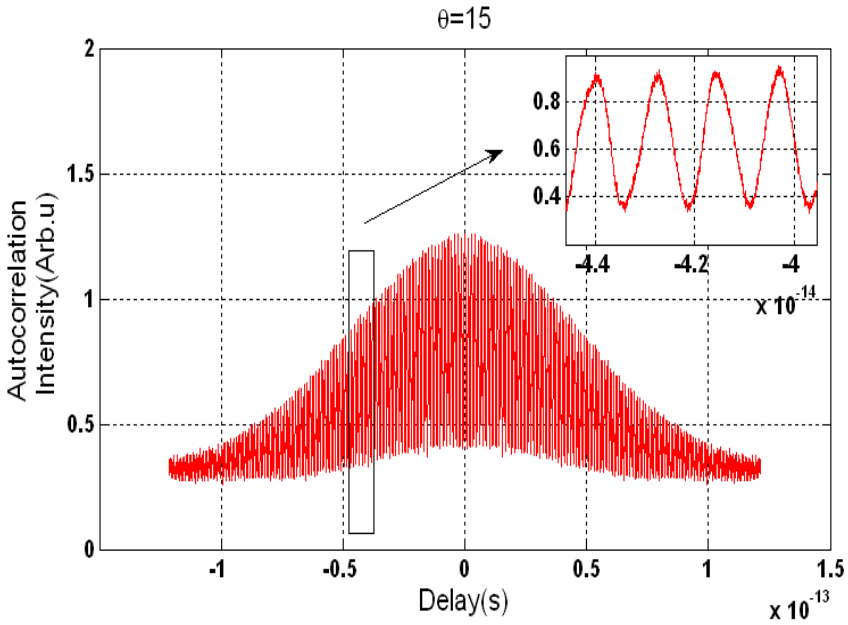

Figure 5-14 Autocorrelation function when the angle is set to 15^0 (Balanced return fields)

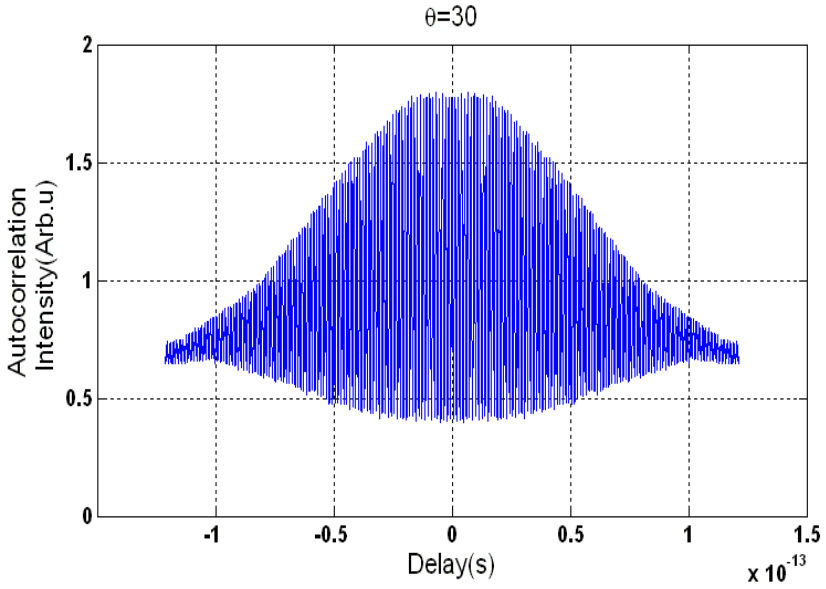

Figure 5-15 Autocorrelation function when the angle is set to 30^0 (Balanced return fields)

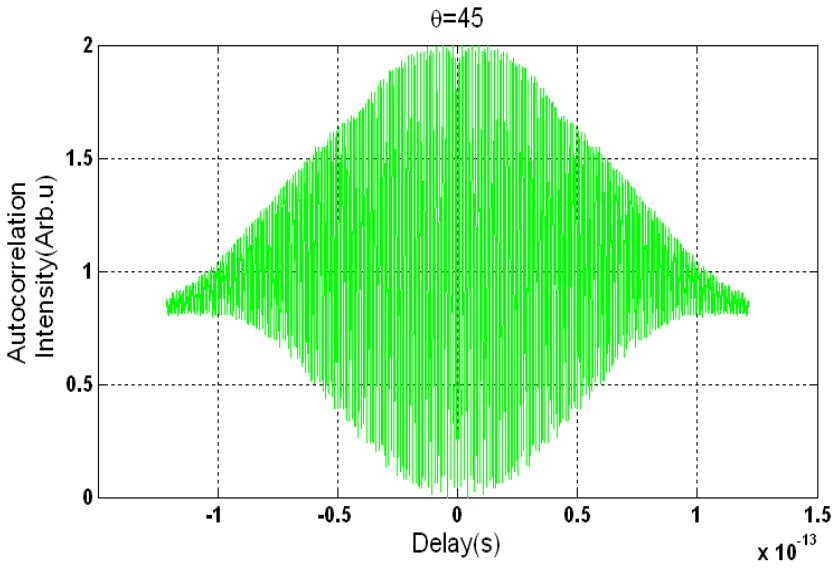

Figure 5-16 Autocorrelation function when the angle is set to 45^0 (Balanced return fields)

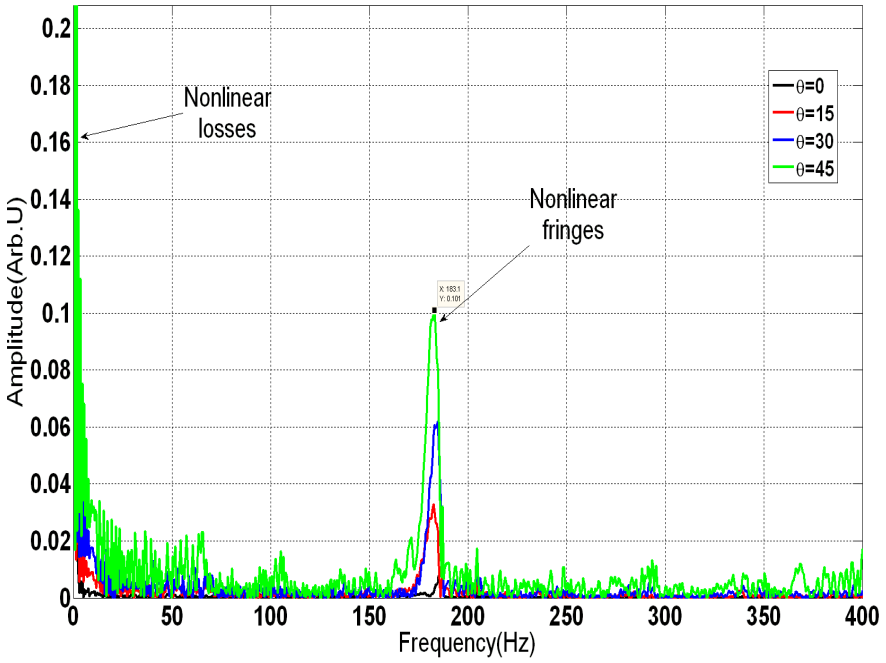

Figure 5-17 Fourier transform of the measured signal for each angle (Balanced return fields)

We present in *Figure 5-17* the fast Fourier transform of each measured signal. The same result was obtained using simulations in *Figure 4-24*. The peak observed at zero frequency represents the DC component, which becomes maximal when the angle is 45^0. On the other hand, the contrast of the nonlinear fringes at the doubled frequency is also proportional on the angle and has its maximum when the angle is set to 45^o.

5.4.2 Experimental Linear and nonlinear Michelson fringes versus delay

- Coherence length of the femtosecond laser of Vigo

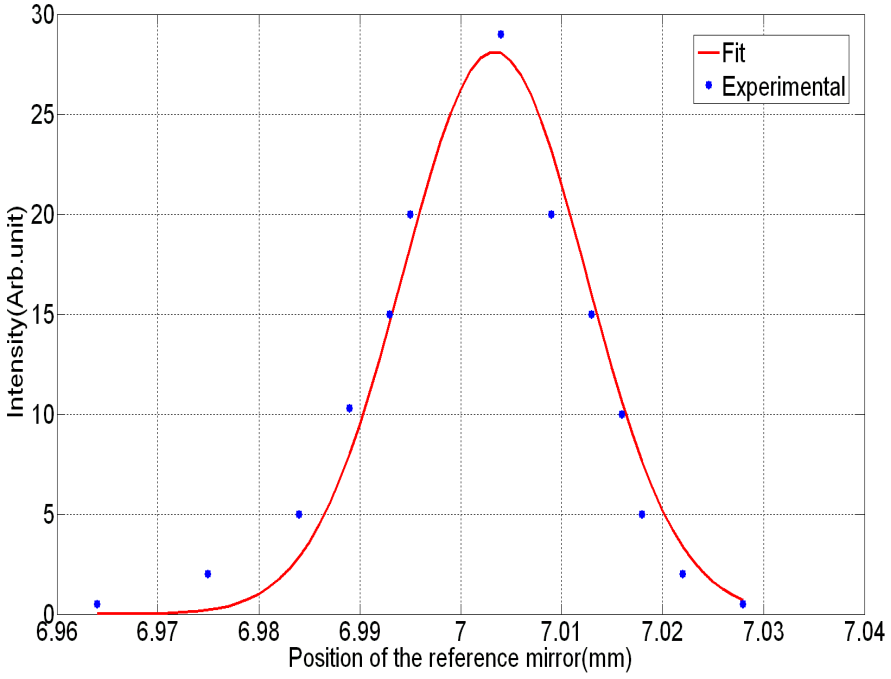

Figure 5-18 Autocorrelation bell of the femtosecond laser.

Figure 5-18 illustrates the autocorrelation bell of the femtosecond laser. In blue we present the experimental measurements and the fit with a Gaussian bell in red. These measurements were done by using a Michelson setup; both arms contain of a mirror, where the position of one of them can be controlled mechanically. The type II crystal was positioned at the angle zero where no Michelson fringes are observed. For each position of the reference mirror we measure the light intensity using a power-meter.

From this figure, we observe that the full width of the correlation bell at the floor level is approximately *(7.03-6.96) mm=70µm*. The FWHM is equal to *20µm*, that converts to (*20µm x 2x 100fs /30µm =133fs*).

- Linear and nonlinear Michelson fringes versus delay

These measurements were done to confirm the dependence between the contrast of the fringes and the delay. It is based on the theory found in equations (4.37) and(4.38), and it was explained and illustrated through simulations in *Figure 4-17* and *Figure 4-19.*

The same setup presented in *Figure 5-1* has been changed in order to do these measurements. The femtosecond laser[1] is centered at *1300 nm*, its autocorrelation bell was presented in *Figure 5-18* the piezo is replaced by a mirror fixed on a translating stage to vary the delay and the photodetector is replaced by a CCD camera to acquire images.

We show in *Figure 5-19, Figure 5-20* and *Figure 5-21* the evolution of the contrast of the Michelson fringes when the angle of the crystal was around 45^0, which means that we have the maximum contrast and the maximum self-doubling. Note that we considered an unbalanced return field ($a_1=3a_2$).

If the delay is equal to -2 μm (near the optical contact), we observe only the nonlinear fringes illustrated by the vertical lines with equal intensity. By moving the translating mirror the delay increases by $2\mu m$, the optical delay causes a difference in the contrast, indicating the optical contact (delay=0 and maximal contrast). Then if we continue to increase the delay far from the optical contact to $20\mu m$, the linear fringes will dominate over the nonlinear fringes, which are observed in *Figure 5-21*. The linear fringes have half spatial frequency than the nonlinear fringes. Note that the CCD has activated the AGC (automatic gain control) which cancels partially the difference in intensity between images.

[1] This experiment was done with the laser chain of the University of Vigo-Spain.

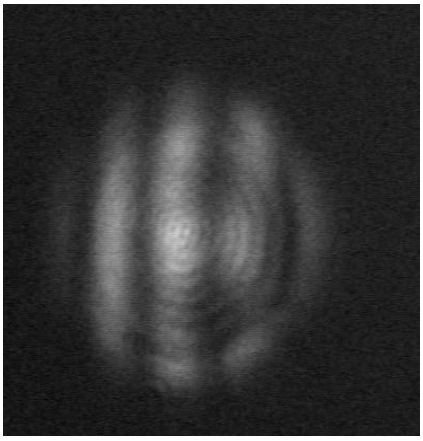

Figure 5-19 Maximum contrast of the Michelson fringes at the maximum self-doubling. Delay=-2µm

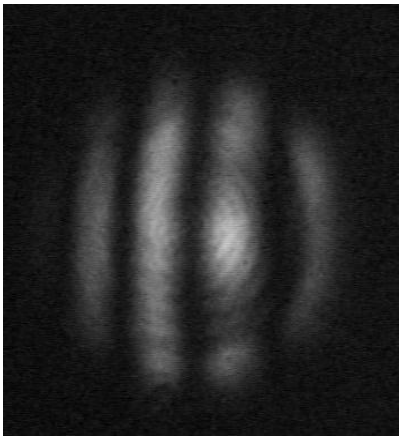

Figure 5-20 Maximum contrast of the Michelson fringes at the maximum self-doubling. Delay=0µm

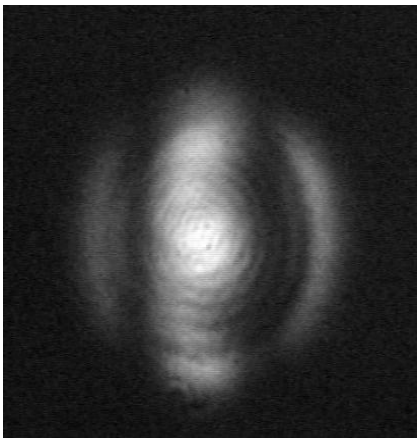

Figure 5-21 Maximum contrast of Michelson fringes at the maximum self-doubling. Delay=20µm

5.4.3 Experimental Fizeau fringes in linear OCT to calibrate the nonlinear OCT setup

In order to compare and understand the linear and nonlinear fringes, we used the sample described in *Figure 5-22*. In fact we know that in linear

optic the distance between two consecutive fringes is equal to half of wavelength, but in nonlinear optic we have a three-wave coupling scheme.

So in order to understand how the three waves couple in nonlinear optic, these measurements were performed. The sample is composed of two layers (disk) of silicon separated by two pieces of paper, to realize a thin air wedge. The thickness of the gap was *69 μm* which is compatible with the full width of the correlation bell at the floor level of the autocorrelation function estimated in *Figure 5-18*. This sample is mounted on a piezo controlled by a DC voltage, which can exert a pressure on the rear surface of the second plate. This pressure can create a shift in the fringes due to the change of the path length.

Note that a cross was carved on the rear surface of the first plate for in order to identify the interface by imaging.

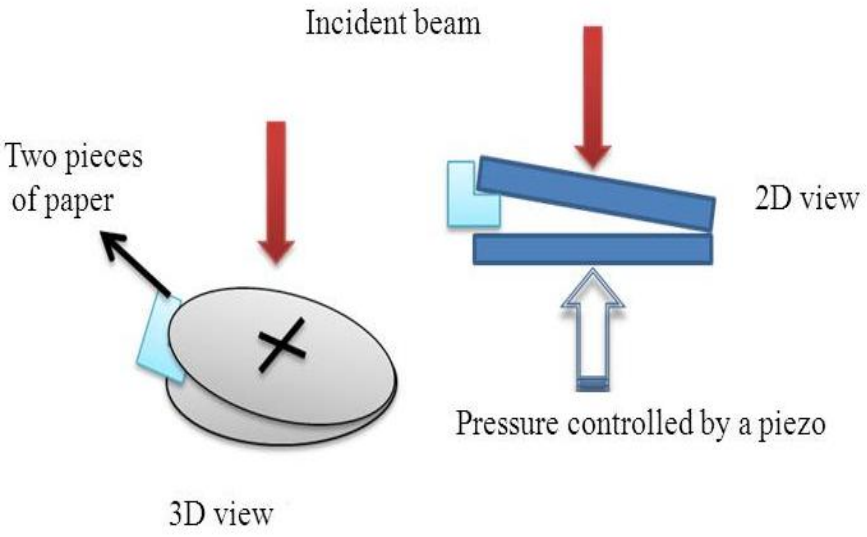

Figure 5-22 3D and 2D view of the sample used for Fizeau pattern

- Linear OCT Fizeau fringes

The images illustrated in *Figure 5-23* and *Figure 5-25* were obtained through our FDOCT imaging setup described in *Figure 2-1* in the first part of the thesis, after replacing the sample arm with our new sample described in *Figure 5-22*. The FDOCT works[1] by acquiring the signal as a function of the wavenumber and then by performing Fourier transform; we can obtain the sample reflectance as a function of the depth. So it is possible numerically using the Fourier transform to select only the tomographic information that comes from the second layer which contains the Fizeau fringes.

In those images, we observe a part of the cross carved at the back of the top plate, and the parallel Fizeau fringes with equal distance. The ASE broadband laser source described in *Figure 2-2* has been used, after reshaping its spectrum into symmetrical Gaussian, the central wavelength was estimated λ_0*=1550nm*.

Then by applying a *30 volts* voltage to the piezo actuator presented in *Figure 5-22*, it creates a pressure which tilts the bottom wafer by compressing the paper spacer. We can see a parallel shift of the fringes, which demonstrates that these fringes are effectively Fizeau fringes. The intensity profile between the same two points from both images is presented in *Figure 5-24* and Figure *5-26*. It represents the intensities of the pixels across a line chosen between two specific points. The x axis corresponds to the distance across the line, and the y axis is the pixel intensity. We see clearly a shift from the position (in pixel) 26 to 52 and 118 to 144.

[1] The FDOCT was explained in the first chapter of the thesis. The images were obtained using the scanning mirror and then by reconstructing pixel per pixel the images

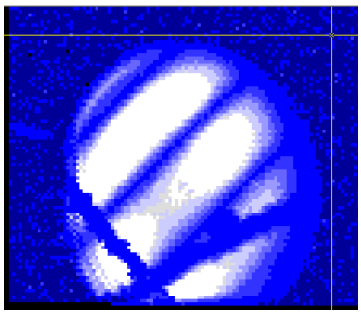

Figure 5-23 linear Fizeau fringe which is taken from our FDOCT. The applied voltage is 0V

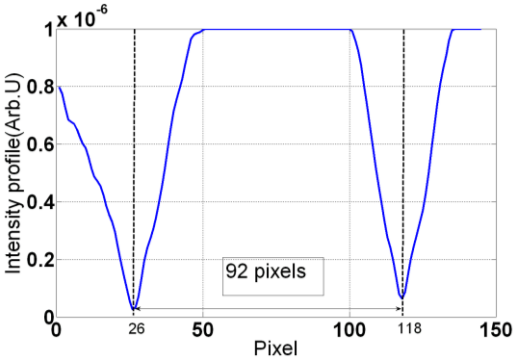

Figure 5-24 Intensity profile when the applied voltage is 0V

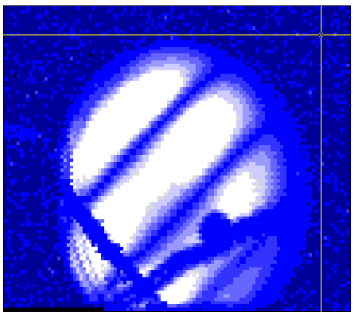

Figure 5-25 Fizeau linear fringe which is taken from our FDOCT. The applied voltage is 30V

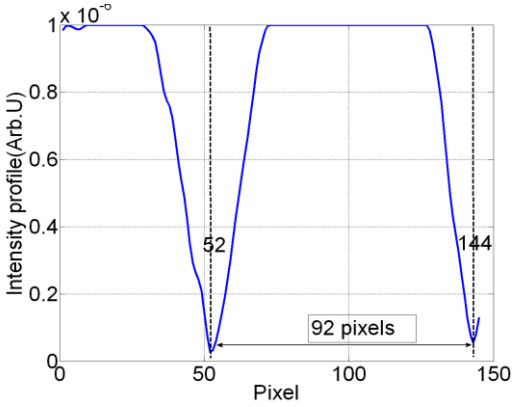

Figure 5-26 Intensity profile when the applied voltage is 30V

Knowing that the distance between two adjacent minima corresponds to half of the wavelength, we can calculate the shift of the fringes when we change the voltage from *0V* to *30V*:

$$\frac{(144-118)}{92}\cdot\frac{1550}{2} = 219\text{nm} \pm 9\text{nm}$$

The uncertainty is estimated by evaluating the distance between two pixels in nm.

- Nonlinear Fizeau fringes

The same sample is now inserted in our nonlinear setup presented in *Figure 5-32*. The photodetector is replaced by a CCD camera to perform imaging, the femtosecond laser has a central wavelength of *1300 nm* to avoid the silicon absorption, and the crystal was set at the angle zero to realize the minimum self-doubling. The femtosecond pulse is sent to a polarizer beam splitter which divides the input field among two orthogonal polarizations. One of the fields (presented in green) probes the reference mirror mounted on a translation stage, and the other one probes our multilayer sample. The return from the multilayer sample consists of three fields: the wavefront from the front face of the sample 1 (in blue), the wavefront from the rear face of the sample 1 (in red) and the wavefront from the front face of the sample 2 (in black). The optical contact is realized between the reference mirror and the mid-space between the rear face of the sample 1 and the front face of the sample 2. The Fizeau fringes are observed between the red and the black wavefront.

The Second Harmonic Generation in a BBO crystal type II ensures that the signal that comes from the front face of the sample (blue color) is eliminated and only the useful component (Fizeau fringes) is doubled.
We present in *Figure 5-27* and *Figure 5-29* the nonlinear Fizeau fringes for the voltages *0* and *30V*; the corresponding intensity profiles are presented in *Figure 5-28* and *Figure 5-30*.

Therefore the shift of the fringes when we change the voltage form 0V to 30V is:

$$\frac{(98-86)}{33}.\frac{1300}{2} = 236\text{nm} \pm 20\text{nm}$$

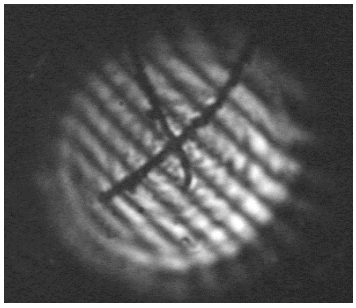

Figure 5-27 Nonlinear Fizeau fringe. The applied voltage is 0V

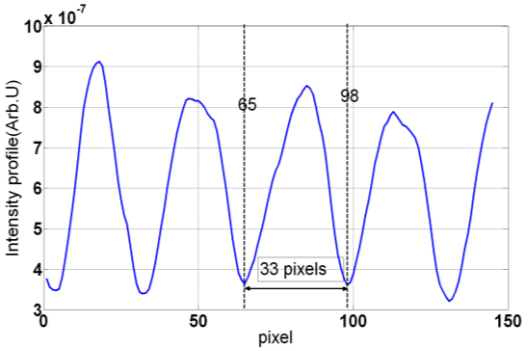

Figure 5-28 Intensity profile when the applied voltage is 0V

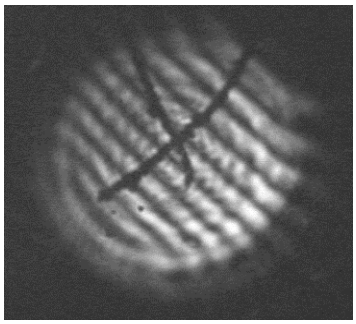

Figure 5-29 Nonlinear Fizeau fringe. The applied voltage is 30V

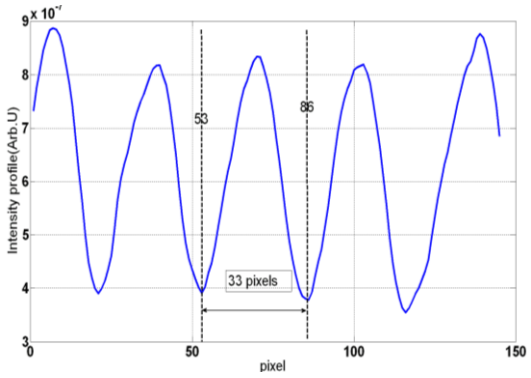

Figure 5-30 Intensity profile when the applied voltage is 30V

We have confirmed in both imaging methods that the shift in the fringes is the same when the voltage has changed from *0* to *30V*. Therefore we can conclude, as predicted, that the distance between two consecutive adjacent fringes is equal to half of the laser source wavelength in linear and nonlinear Fizeau fringes.

Note that the images obtained from the FDOCT setup were acquired using a two axis scanner; on the other hand the images obtained from the femtosecond setup were acquired using a CCD camera. The CCD camera has a larger field of view when we compare the images with those obtained from the FDOCT.

5.4.4 Tomographic application using femtosecond gated method and FDOCT method.

The sample described in *Figure 5-31* is inserted in our FDOCT setup and the nonlinear imaging setup to generate Fizeau fringes. This sample contains a first homogeneous Nickel coating on the front face of the second wafer and then a second Nickel layer which creates an edge of 265nm in the second sample. This edge was measured using the DEKTAK 150 (BRUKER) stylus profilometer: *(265 ± 1) nm*, see *Figure 5-33*. The reason we chose the Nickel is that its transmittance[1] is equal to zero.

Since the slope of the air wedge sample will stay the same, the distance between two adjacent minima will have the same value, except when the light beam is scanned around the edge. Knowing that the thickness will change abruptly when we traverse the edge, this will be displayed as a change of the phase value, and therefore we will observe a unique shift in the Fizeau fringes.

- FDOCT setup

The Fizeau fringes using our FDOCT imaging are shown in *Figure 5-34*. This tomographic image is obtained after selecting numerically, using the Fourier transform, the information that comes from the rear face of the first sample and the front face of the second sample. The inhomogeneity present in the bottom of the image corresponds to the black mark that we have made to identify the position of the edge. The line in the middle indicated by the red arrow corresponds to the edge. This is justified by the fact that the distance between two consecutive fringes has increased when measured around the edge.

[1] http://refractiveindex.info/legacy/?group=METALS&material=Nickel

Figure 5-34 illustrates the intensity profile of the image. It generates the intensities of the pixels across a line chosen around the edge. We observe many minimum peaks with different intensity indicating the black lines in the image. The minimum intensity peak marked with the red circle corresponds to the edge.

Knowing that the distance between two adjacent minima is half the wavelength, we can compute the step height (height of the edge) that separates the two Nickel layers:

$$step = \frac{(38,6 - 28,5)*1550}{2*28,5} = 274nm \pm 27nm$$

- Nonlinear optic imaging setup (femtosecond gated method)

The same sample described in *Figure 5-31* is now inserted in our nonlinear setup presented in *Figure 5-32*. As explained before, by realizing the optical contact between the reference mirror and the Nickel layer, the BBO crystal type II will ensure that the signal that comes from the front face of the sample (blue color) is eliminated and only the useful component (Fizeau fringes) is doubled.

We illustrate in *Figure 5-35* the nonlinear Fizeau fringes that come from the air wedge sample. We observed the black dot on the left of the image which hides the Fizeau fringes; the edge is represented by the horizontal line in the middle with low intensity indicated by the red line. The distance between the Fizeau fringes has increased around the edge and it can be seen on the right where we plotted the intensity profile of a line across the edge.

We see many minimum peaks in the intensity profile, indicating the Fizeau fringes and the edge; the edge has the minimum peak.

Knowing that the distance between two consecutive fringes is equal to half of the laser wavelength except when working around the edge, we can estimate the height of the edge:

$$\text{step} = \frac{54-39}{39}.\frac{1300}{2} = 250\text{nm} \pm 17\text{nm}$$

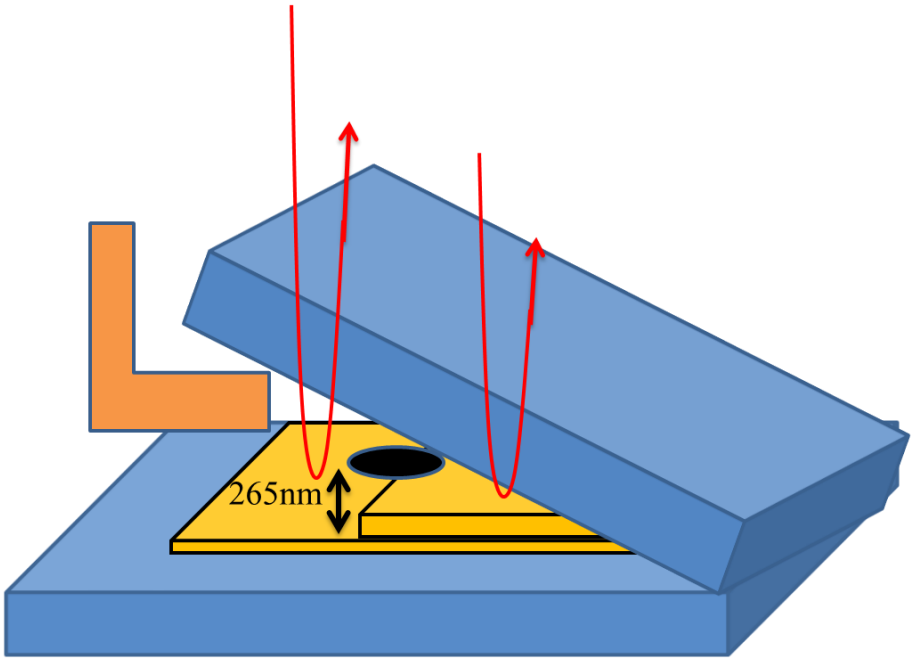

Figure 5-31 Air wedge sample, it consists of two layers presented in the blue colors, two small papers pieces in the pink color to create a slope, Nickel layer to generate an edge, and a black ink mark to locate the edge

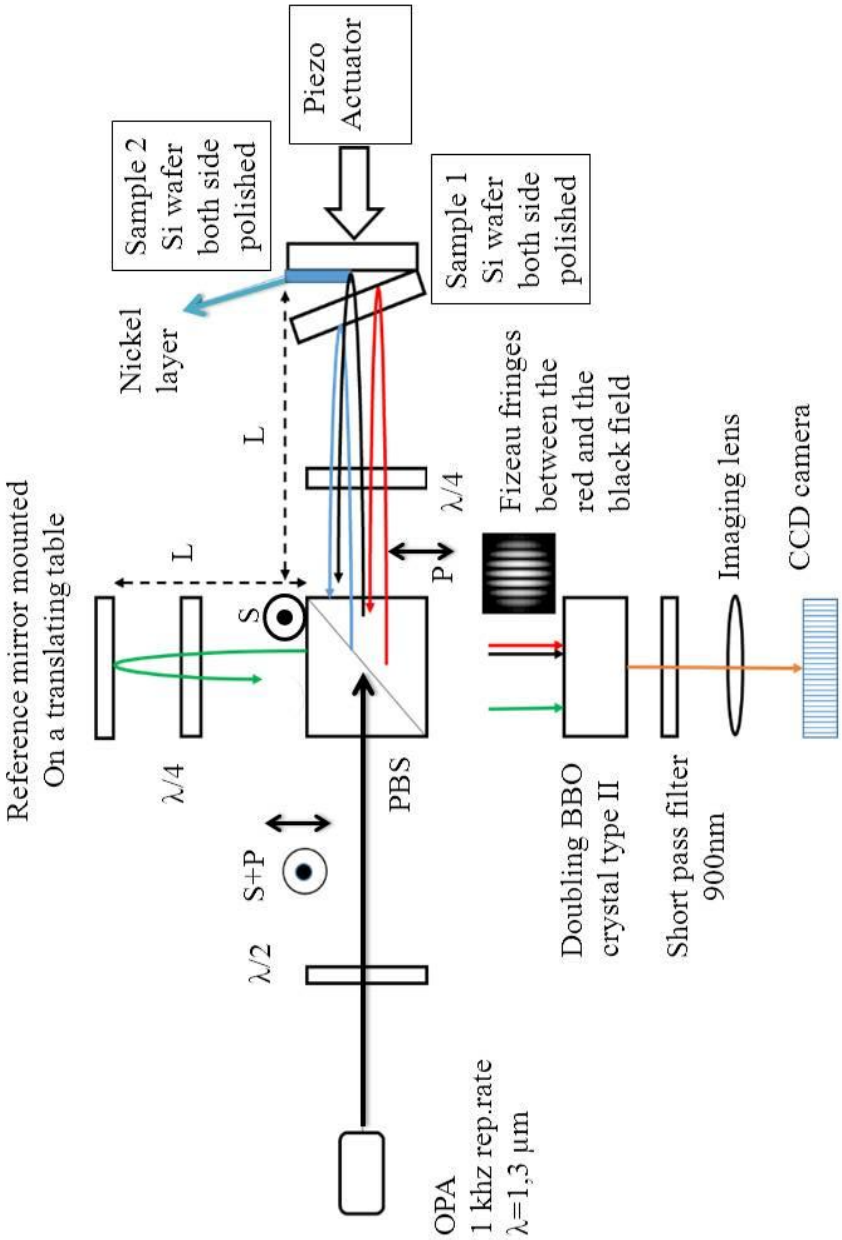

Figure 5-32 Experimental layout

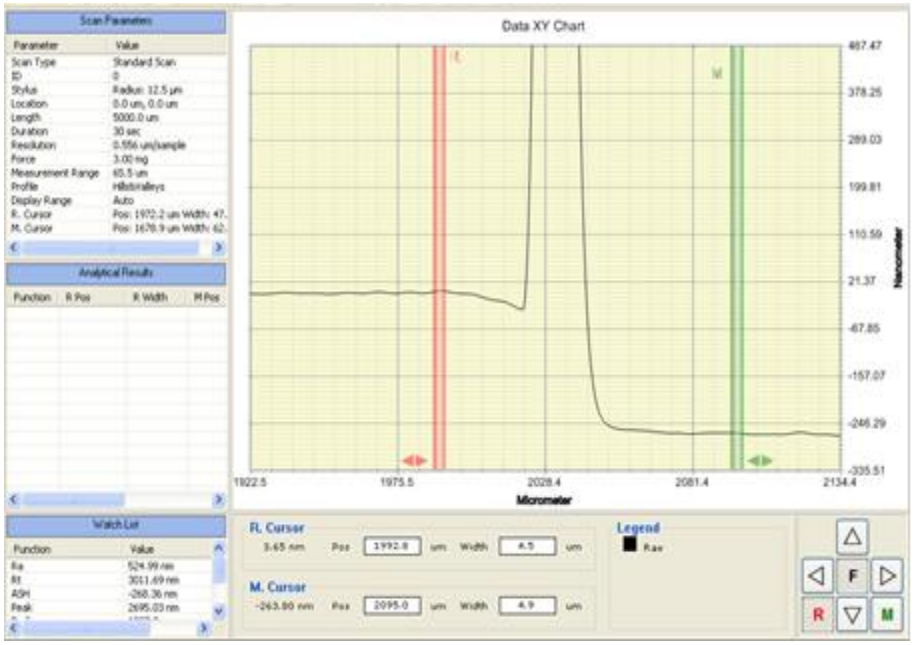

Figure 5-33 Measuring the step edge using the DEKTAK 150(BRUKER).

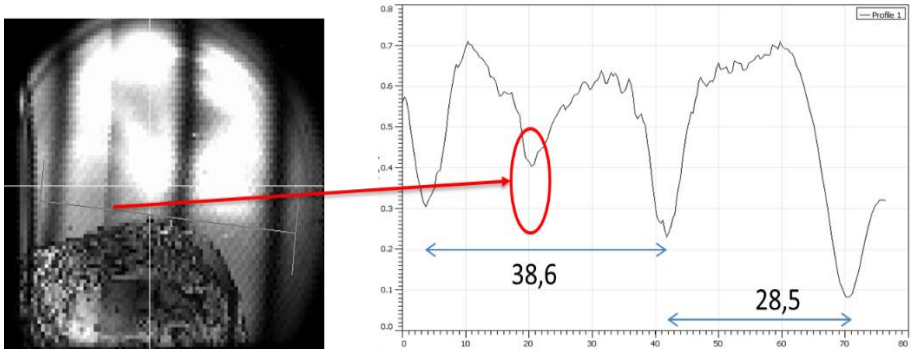

Figure 5-34 On the left: Linear Fizeau fringes which are captured by the FDOCT system. On the right: Intensity profile across the fringes and the edge

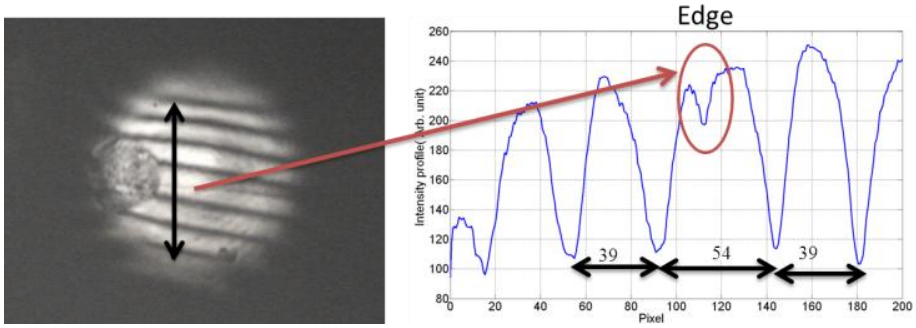

Figure 5-35 On the left: Nonlinear Fizeau fringes which are captured by the Nonlinear gated system at the minimum self-doubling. On the right: Intensity profile across the fringes and the edge.

5.5 Background elimination and interferometric capability in optical coherence tomography

- Dependence of the correlation on the delay

We present in this section a series of images (Figure 5-36) of another zone of the same silicon wafer sandwich with the nickel step of *265 nm* (horizontal) and the edge of both nickel depositions (vertical), Figure 5-37. Different delays, measured by the translation of the reference mirror in μm, were selected. We assigned the "optical contact" or zero-delay arbitrarily to one of the two central images in which the average intensity and fringe contrast are higher. Then if we move away from the optical contact, the intensity diminishes in both directions (up and down) and practically disappears when the displacement is about *35 μm* from the optical contact.

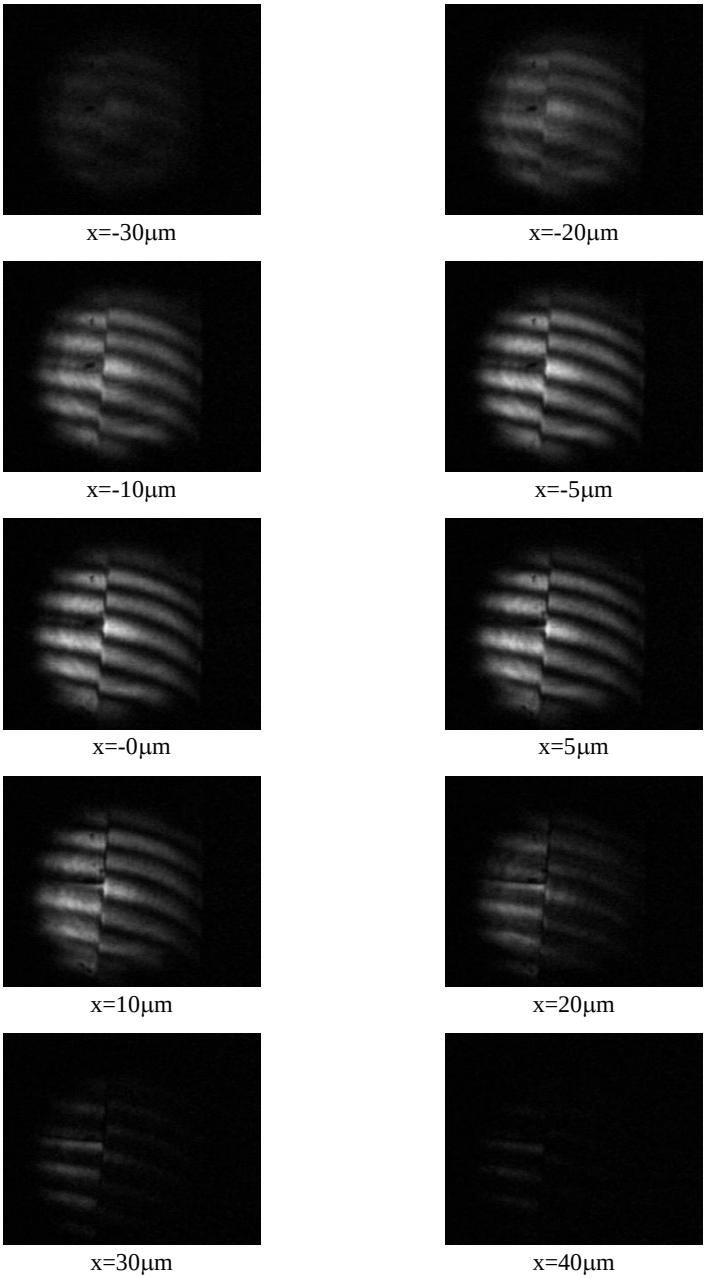

Figure 5-36 Series of images showing the contrast of the images as a function of the delay

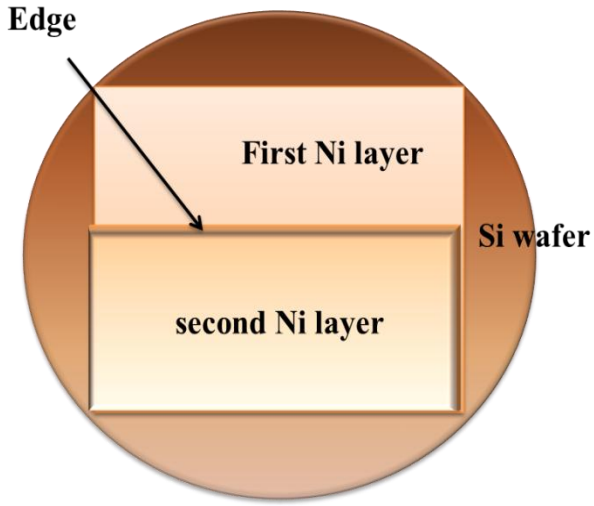

Figure 5-37 silicon wafer sandwich with nickel step of 265 nm (horizontal) and edge of both nickel depositions (vertical)

- **Analysis**

We present here an analysis of the series of images presented in *Figure 5-36.* We chose the first five images from position *6.804 mm* to *6.839 mm*. For each image we reconstructed the intensity profile along the Fizeau fringes and then we performed a Fourier transform (FFT in *Matlab*) of the intensity profile. We illustrate in *Figure 5-38* the five images and the FFT of their intensity profile. The nonlinear peak is located at the frequency 64 (arbitrary unit), it reaches the maximum value *67.3dB* when the position is *6.839 mm* indicating the optical contact. We can see that the contrast can be controlled as a function of the position, and the difference in contrast between the position where no fringes are observed and the position at the optical contact can be estimated to be around *37.3 dB* (see image 5 below). Note that the camera was always operated in the automatic gain mode.

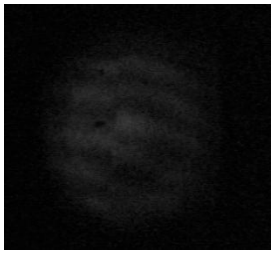

position =6,804mm

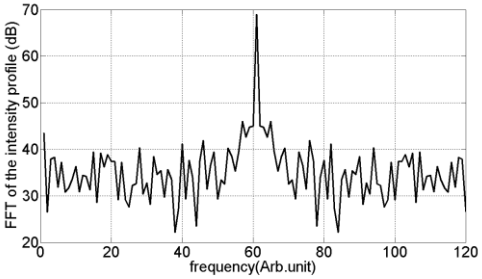

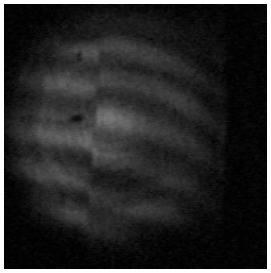

position =6,814mm

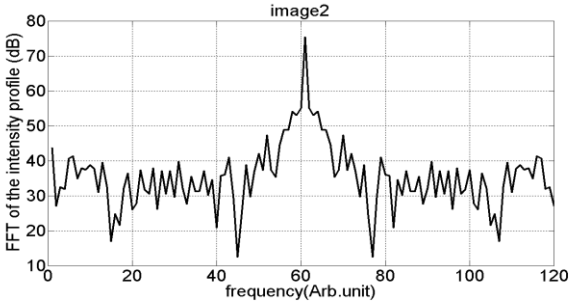

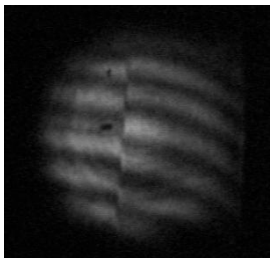

position =6,819mm

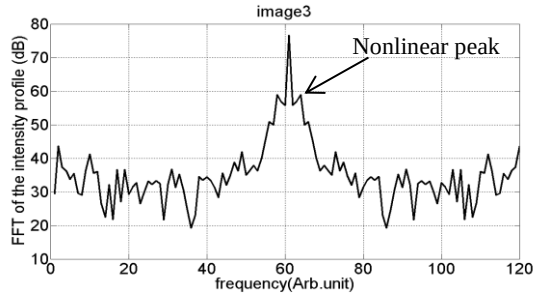

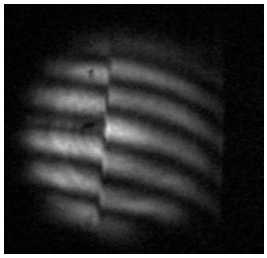

position =6,829mm

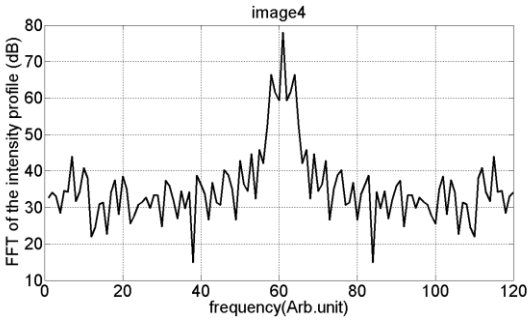

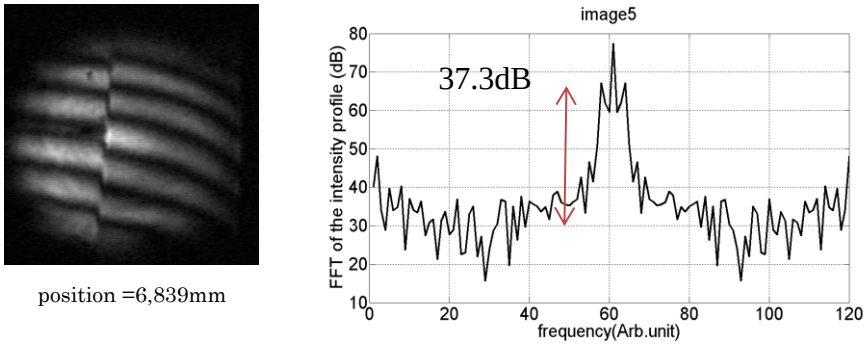

Figure 5-38 FFT of the intensity profile of different images for different positions.

5.7 Summary

We have designed a nonlinear interferometry setup based on the second order autocorrelation technique. We used this setup to validate the theoretical model which we developed previously. We have shown the dependency between the contrast of the fringes and the angle of the crystal and with the delay created between the two arms. The contrast of the Michelson nonlinear fringes is maximal when the angle is 45^o. We also presented a novel setup to work with dark field interferometry which permits to cancel out the DC and to improve the contrast; this was done by generating the Fizeau fringes in one arm and by turning the crystal to reach the zero angle. We explained in the case of the dark field interferometry how the waves couple in the case of three-wave coupling. The useful Fizeau fringes can be selected physically by moving the reference arm to realize the optical contact with the desired scattered light. A test of feasibility was made on a thin air wedge composed of two Silicon samples, where we measured the height of a Nickel layer with a good precision. The same test was performed using the FDOCT setup to calibrate and validate the nonlinear setup.

Conclusion and perspectives

In the present thesis, a novel method was presented and developed to improve the axial resolution of an FDOCT imaging system, and another novel method was validated to eliminate the strong backscattered light that comes from the first layer in a multilayer sample.

A setup for the FDOCT was assembled in our laboratory. It uses the return of the light to reconstruct the images pixel per pixel using a two-axis galvanometric scanner, and a linear CCD camera combined with a spectrometer. The lateral resolution of the setup was estimated to *4.2 µm*.

A proof-of-principle experiment using this setup demonstrated the possibility of improving the axial resolution for a broadband source using a dynamic bilayer sample for MEMS applications. Our two-layer sample consisted of a silicon sample and a mirror mounted on a piezo actuator. Two cases were considered, and in both cases the distance between the two layers was smaller than the axial resolution of our broadband source:

- When the step between the two positions of the dynamic mirror was bigger than 775nm (half of wavelength), we were able to resolve the two layers and therefore improve the axial resolution to a limited value determined by the distance between two pixels in the spatial Fourier domain. The improvement factor was estimated around 13, in comparison to regular OCT, where the resolution is defined by the coherence length.
- For steps smaller than *775 nm* the position of the two layers was resolved, modulo half of wavelength, with a resolution of 65nm. The limitation comes from the noise of our system.

This setup has been also used as a reference to understand and quantify the Fizeau fringes in nonlinear optics.

Further work can be done with this setup; we can for example repeat this experiment with another source at our disposal which is the Fianium supercontinum broadband laser source. We can apply this method to an actual dynamic MEMS sample like an accelerometer, to measure the amplitude and the frequency of an oscillating accelerometer. We can also detect the inhomogeneity or the imperfection inside MEMS, and therefore evaluate if replacement or improvement of the fabrication process is needed. Another novel method was illustrated and developed in detail in this thesis, to improve the contrast of an imaging system by canceling the non-useful backscattered light from the front face of a multilayer sample. The amount of the backscattered light that is eliminated from the imaging detector can be controlled so that the high intensity reflection from the sample can be rejected from the depth scan, which permits to reach a better sensitivity.

A full novel theoretical model was presented in this thesis which explains how the user can control the amount of the uninteresting strong scattering sites within the sample. The optical gating is based on the use of a femtosecond laser combined with a Michelson second order autocorrelation technique and a nonlinear type II BBO crystal under phase matching condition. The selection of the weaker scattering sites of interest within the sample can be realized through the optical contact, by setting the length of the reference arm equal to the position of the desired scattering surface measured from the polarized beam splitter.

We have theoretically demonstrated that the strong undesired scattered beam (DC) can be controlled by turning the crystal around the light propagation axis. The contrast of the linear and nonlinear Michelson fringes is dependent on the angle. In order to eliminate completely the DC, the angle must be set to zero as measured between the light field polarization vector and the ordinary axis of the BBO crystal. It has been also demonstrated that the Michelson fringes will vanish when the angle is set to zero. So to achieve

full elimination of the DC and obtain fringes at the same time, the fringes must be created in the sample arm already. This can be done using Fizeau fringes which is one of the well-known techniques in interferometry.

A second order Michelson autocorrelator setup was used to analyze the quality of generated fringes. We showed that the contrast of the nonlinear fringes is dependent on the crystal angle and has its maximum when the angle is 45^0. We illustrated also using this setup the effect of the return field balancing coefficient and the delay on the appearance and the contrast of the linear fringes.

An application was studied, based on a thin air wedge formed by two silicon samples where a first Nickel layer was covering the front face of the second sample, and a second Nickel layer was covering only partially half of the surface, forming an edge of *265 nm*. Using the nonlinear gate, the strong scattered light from the front face of the first plate was eliminated, while the weaker light of interest was frequency doubled. This weaker light contains the Fizeau fringes which should be equidistant between each other, except when working around the edge. This shift among the fringes can be quantified to measure the height of the edge within the sample which was determined to be 260nm, in excellent agreement with the value obtained with a profilometer.

We have also used the FDOCT setup as a reference to confirm the Fizeau fringe spacing value in nonlinear optics. The measurement of the height was *273 nm* in this case, which was confirming the physical description of the non-linear approach.

The FDOCT setup has the advantage of being inexpensive, but the acquired signal contains the reflected light from all the layers. It can nevertheless be numerically filtered using a Fourier transform of the detected signal, to retrieve only the desired signal on a particular depth position. But

if the undesired scatterings are very strong it may contribute to saturate the detector.

The femtosecond gate method shows on the other hand a great potential for future applications. The undesired scattering is physically eliminated before arriving to the detector. A comparison between different existing methods and our method is presented below in *Figure 5-39*.

An alternative technique as shearing interferometry can be used instead of Fizeau fringes. The application of the Fizeau technique in imaging is limited, since it works only on a thin wedge sample. On the other hand the interference pattern in a shearing interferometer is realized by superimposing two images of the object wavefront. Nevertheless, numerical analysis is needed to correct the wavefront errors, and a laser with high degree of spatial coherence is needed because the interference occurs between the reflections from different parts of the object wavefront. The idea of using the shearing interferometry is not yet ready for application, but some experiments can be conducted with our setup to prove its feasibility.

Method	Wavelength	resolution	SNR improvement	Data acquisition
Black background interferometry(our method)	1300nm	<70µm	No background. Limited by the camera noise.	imaging
Swept-laser-based FDOCT system using an EO phase modulator [22]	1310nm	9 µm	20 dB	scanner
Complex spectral OCT [17]	810nm	14 µm	8dB	scanner
Reduce the depth of view due to the temporal overlap requirements in sum-frequency mixing [61].	1280nm	<10 µm	29dB	scanner
Projection of multiple phase-shifted interferograms onto an orthogonal basis set to reconstruct the complex interferograms [60]	1310nm	9 µm	30dB	imaging

Figure 5-39 Comparison between our method and what exists already in the literature

Bibliography

[1] A. Gupta, and A. Ahmad. "*Microsensors Based on MEMS Technology"*. *Defence Science Journal(2007)*. Vol. 57, No. 3, 225–232.

[2] K. Gilleo," *MEMS Packaging Solutions*". *EP & P(2000)*. p. 49,50, 52, 53, 55, 56.

[3] A. Gupta, R. Singh, A. Ahmad, and M. Kumar. "*Bonding Techniques for Silicon Microsensors*". *In Proceedings of XI International Workshop on Physics of Semiconductor Devices, edited by V. Kumar and P.K. Basu. Allied Publishers, (2001),* p. 519-22.

[4] A. F. Fercher, W. Drexler and T. Lasser."*Optical coherence tomography—principles and applications"*. *INSTITUTE OF PHYSICS PUBLISHING(2003).*

[5] D. Huang, E.A. Swanson, C.P. Lin, J.S. Schuman W.G. Stinson, W. Chang, M.R. Hee, T. Flotte, K. Gregory, C.A. Puliafito and J.G. Fujimoto " *Optical coherence tomography*". *Science(1991)*. vol. 254, p. 1178–1181.

[6] J.M. Schmitt "*Optical coherence tomography*". *J. Biomed .Optics (1996)*. vol. 1, p. 157–173.

[7] S. Haffouz, P. J. Barrios, R. Normandin, D. Poitras and Z. Lu." *Ultrawide-bandwidth, SLED using InAs quantum dots of tuned height"*. *Optics Letters(2012).* vol. 37, p. 1103–1105.

[8] H.Wang, M.W. Jenkins, and A. M. Rollins. " *A combined multiple-SLED broadband light source at 1300 nm for high resolution optical coherence tomography".Optics communications(2008)*. Vol. 281, p. 1896-1900.

[9] C.K. Hitzenberger, A. Baumgartner, A.F. Fercher. "*Dispersion induced multiple signal peak splitting in partial coherence interferometry". Optics Communications(1998)*. Vol. 154, p.179-185.

[10] Y. Zhang, M. Sato, N. Tanno." *Resolution improvement in optical coherence tomography based on destructive interference"*. *Optics Communications (2001)*.Vol. 187, p. 65-70.

[11] S. Chang, X.Cai and C. Flueraru. "*Resolution Enhancement for Tomographical Images of a Full-Field OCT System"*. *The Open Optics Journal*. *(2009).* Vol. 3, p. 24-28.

[12] E. Bousi, I. Charalambous and C. Pitris. "*Optical coherence tomography axial resolution improvement by step frequency encoding"*. *Optical Society of America(2010)*. Vol. 18, p. 11.

[13] I. Shavrin, L. Lipiäinen, K. Kokkonen, S. Novotny, M. Kaivola and H. Ludvigsen. "*Stroboscopic white-light interferometry of vibrating microstructures". Optics Express (2013).* Vol. 21,p. 16901-16907.

[14] S. Zhong, H. Shen and Y. Shen. "*Real-time monitoring of structural vibration using spectral-domain optical coherence tomography". Optics and Lasers in Engineering (2011).* Vol.49, p.127-131.

[15] R. Leitgeb, C. K. Hitzenberger and A.F. Fercher. "*Performance of fourier domain vs. time domain optical coherence tomography". Optics Express* (2003). Vol. 11, p. 889-894.

[16] W. Drexler, J.G. Fujimoto "*Optical Coherence Tomography, Technology and Applications". Springer(2008).*

[17**]** M. Wojtkowski, A. Kowalczyk R. Leitgeb and A.F. Fercher. "*Full range complex spectral optical coherence tomography technique in eye imaging". Optics Letters*(2002). Vol.27,p. 1415–1417.

[18] A. Rainer, A. Leitgeb, K. Christoph, K. Hitzenberger, F. Fercher and T. Bajraszewski." *Phase-shifting algorithm to achieve high-speed long-depth-range probing by frequency-domain optical coherence tomography". Optics Letters (2003).* Vol.28, p. 2201–2203.

[19] M. Sarunic, M. A. Choma, C. Yang and J.A Izatt." *Instantaneous complex conjugate resolved spectral domain and swept-source OCT using 3×3 fiber couplers*". *Optics Express(2005).* Vol.13, p. 957–967.

[20] B. J. Vakoc, S. H. Yun G. J. Tearney and B.E. Bouma." *Elimination of depth degeneracy in optical frequency-domain imaging through polarization-based optical demodulation*". *Optics Letters(2006),* p. 362–364.

[21] K. Lee, P. Meemon, W. Dallas, K. Hsu and J.P. Rolland. "*Dual detection full range frequency domain optical coherence tomography*". *Optics Letters(2010).* Vol.35, 1058–1060.

[22] J. Zhang, J. Stuart Nelson and Z. Chen. *"Removal of a mirror image and enhancement of the signal-to-noise ratio in Fourier-domain optical coherence tomography using an electro-optic phase modulator*". *Optics Letters(2005).* Vol.30, p.147-149.

[23] M. Pircher, C.K. Hitzenberger, U.S. Erfurth." *Polarization-Sensitive Optical Coherence Tomography.* in *Handbook of Optical Coherence Tomography, B. E. Bouma and G. J. Tearney, eds.* (2002), p. 237–274.

[24] M.E. van venlthoven, D.J. Faber, F.D. Verbraak, T.G. van leeuwen, M.D. de Smet. G." *Recent developments in optical coherence tomography for imaging the retina". Prog. Ret. & Eye Res*. (2007), p.57.

[25] B. E. Applegate, C. Yang, A. M. Rollins and J.A. Izatt. "*Polarization-resolved second-harmonic-generation optical coherence*

tomography in collagen". Optics Letters(2004). Vol.29, p. 2252–2254.

[26] C. Vinegoni, J. S. Bredfeldt D. L. Marks and S.A. Boppart. "*Nonlinear optical contrast enhancement for optical coherence tomography". Optics Express(2004).* Vol.12, 331–341.

[27] J. Su, I. V. Tomov, Y. Jiang and Z. Chen. "*Frequency domain second harmonic optical coherence tomography*". *Proc. SPIE 6079, 607901–6 (2006).*

[28] M. V. Sarunic, B. E. Applegate and J.A. Izatt. "*Spectral domain second-harmonic optical coherence tomography*". *Optics Letters(2005).* Vol.30, p. 2391–2393.

[29] Y. Jiang, I. Tomov Y. Wang and Z. Chen. "*High-resolution second-harmonic optical coherence tomography of collagen in rat-tail tendon*". *Applied Phys. Lett (2005).* Vol.86, 133901.

[30] Y. Jiang, I. Tomov Y. Wang and Z. Chen. 2004. "*Second-harmonic optical coherence tomography". Optics Letters(2004).* Vol.29, p. 1090–1092.

[31] X. Gu, S. Akturk, A. Shreenath, Q. Cao and R. Trebino, "*The Measurement of Ultrashort Light Pulses−Simple Devices, Complex Pulses*" *Opt. Rev.(2004)* Vol. 11, p. 141.

[32] C. Dunsby and P. M. W. French, "*Techniques for depth-resolved imaging through turbid media including coherence-gated imaging*," *J. Phys. D: Appl. Phys. 36, R207 (2003).*

[33] J. G. Fujimoto, S. De Silvestri, E. P. Ippen, C. A. Puliafito, R. Margolis and A. Oseroff, "*Femtosecond optical ranging in biological systems*," *Opt. Lett(1986).* Vol. 11, p.150.

[34] Doulé, T. Lépine, P. Georges and A. Brun, "*Video rate depth-resolved two- dimensionalimaging through turbid media by femtosecond parametric amplification*" *Opt. Lett(2000).* Vol. 25,p. 353

[35] M. D. Duncan, R. Mahon, L. L. Tankersley and J. Reintjes, "*Time-gated imaging through scattering media using stimulated Raman amplification*" *Opt. Lett(1991).* Vol. 16, p. 1868 .

[36] T. Yasui, K. Minoshima, E. Abraham and H. Matsumoto, "*Microscopic timeresolved two-dimensional imaging with a femtosecond amplifying optical Kerr gate" Appl. Opt.(2002)* Vol. 41, p. 5191 .

[37] P. A. Franken, A. E. Hill, C. W. Peters, and G. Weinreich. "*Generation of Optical Harmonics*", *Phys. Rev(1961).* Lett. Vol.7, p. 118–119 .

[38] F.Sanchez. *Book* "*Optique non-linéaire*" .*Ellipses, Paris*. (1999).

[39] A. Yariv and P. Yeh. *Book "Optical Waves in Crystals"*. John Wiley & Sons, *New York(1984).*

[40] Y. Wang, , J. Yao. *Book "Nonlinear Optics and Solid-State Lasers" (2012). p. 18.*

[41] F. Zernike, and J.E. Midwinter.. *Applied Nonlinear Optics*. Jhn Wiley(1973).

[42] K. Naganuma, K. Mogi, H. Yamada, "*General method for ultrashort light pulse chirp measurement," IEEE J. of Quant. Elec.(1989).*Vol. 25, p. 1225 -1233

[43] J.C. Diels, J.J. Fontaine, and F. Simoni, "*Phase Sensitive Measurement of Femtosecond Laser Pulses From a Ring Cavity*," in Proceedings of the International Conf. on Lasers. 1983, STS Press: McLean, VA, p. 348-355. J. C. Diels *et al*.,"*Control and measurement of Ultrashort Pulse Shapes (in Amplitude and Phase) with Femtosecond Accuracy*," Applied Optics 24, 1270-82 (1985).

[44] J.W. Nicholson, J.Jasapara, W. Rudolph, F.G. Ometto and A.J. Taylor, "*Full-field characterization of femtosecond pulses by spectrum and crosscorrelation measurements,* "*Opt. Lett(1999)*. 24, 1774 .

[45] S. Santran , M. M. Rosas, L. Canioni, L. Sarger, N. Larissa, A Tirpak, L. B. Glebov. "*Nonlinear refractive index of photo-thermo-refractive glass*". *Optical Materials (2006),* vol. 28, p. 404-407.

[46] J.C M. Diels, J. Fontaine, I. C. McMichael, and S. Francesco. "*Control and measurement of ultrashort pulse shapes (in amplitude and phase) with femtosecond accuracy*". *Applied Optics(1985)*. Vol.24, p.9.

[47] J. Diels and W. Rudolph. second edition "*Ultrashort Laser Pulse Phenomenon: Fundamentals, Techniques and Applications on a Femtosecond Time Scale*". Boston: *Academic Press, (1996),* p.10.

[48] C. Rullière," *Femtosecond laser pulses: principles and experiments. New York*": second edition Springer Science+Business Media, *(2004),* p.32.

[49] S. Santran, M.E Rosas, L. Canioni, L. Sarger. "*Characterization of optical Nonlinearity in semiconductor photodiodes using cross-polarized autocorrelation".* IEEE Journal of selected topics in quantum electronics, *(2004).* **20**(12).

[50] Anthony E.Siegman, "Lasers". University Science Books, p. 373

[51] http://refractiveindex.info/legacy/?group=CRYSTALS&material=Si

[52] www.roperld.com/science/Mathematics/FunctionsRealistic.pdf

[53] P. Hariharan, second edition ."Basic of interferometry" (2007).

[54] Millenia Pro. Diode-Pumbed, CW Visible Lasers Systems. User's Manuel, Spectra- Physics :Lasers & Photonics. (2003).

[55] A. Brun, P. Georges, Sources laser femtosecondes, Institut d'Optique Theorique et Appliquee,URA 14 du CNRS, Universite Paris.

[56] Tsunami. Mode-Locked Ti :sapphire Laser. User's Manual, Spectra-

Physics : Lasers & Photonics. (2003)
[57] http ://micro.magnet.fsu.edu/primer/java/lasers/tsunami/index.html
[58] *Empower. Intracavity-Doubled, Diode-Pumped Nd :YLF Laser Systems. User's Manual ,Spectra-Physics : Lasers & hotonics.(2004).*
[59] http://www.thorlabs.de/thorproduct.cfm?partnumber=DET36A/M
[60] Marinko V. Sarunic, Brian E. Applegate, and Joseph A. Izatt "*Real-time quadrature projection complex conjugate resolved Fourier domain optical coherence tomography*". *OPTICS LETTERS(2006).* Vol. 31, No. 16 .
[61] M.S Muller and J.M Fraser . "*Contrast improvement in Fourier-domain optical coherence tomography through time gating*". Vol. 26, No. 4/ April 2009/J. Opt. Soc. Am. A

Appendix A. Algorithm for separating two layers within the coherence length.

In the figures below, we see the different steps of the method. By hypothesis, the distance between the two layers is smaller than the axial resolution. The amplitude versus depth of many tomograms is presented in *Figure 5-40*, where we clearly see that the two layers are indiscernible. We proceed by studying the movement of a pixel versus time. A sample of 5000 images is taken (the step time depends on the frequency of the camera which is 47khz,). This gives us the temporal evolution of this pixel versus time. This pixel contains the information about the two layers, where we know that one is moving and the other is not, so by taking the Fourier transform of the temporal movement of this pixel we can get the information of the second layer (moving layer) at the right frequency. The reconstruction is plotted versus the depth direction step by step from *Figure 5-41* to *Figure 5-45* . By repeating this procedure for many pixels we are able to get more information on the hidden layer and knowing that the amplitude will be maximal at the center, we obtain the information of the position of the invisible layer.

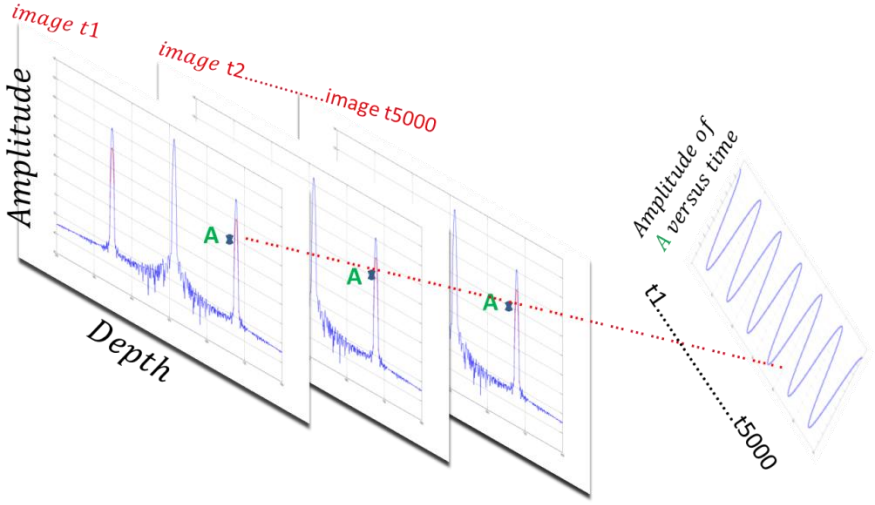

Figure 5-40 At the left: 5000 images presented with one acquisition where each image represents the amplitude versus depth. At the right: the vibration amplitude of a point A chosen versus time

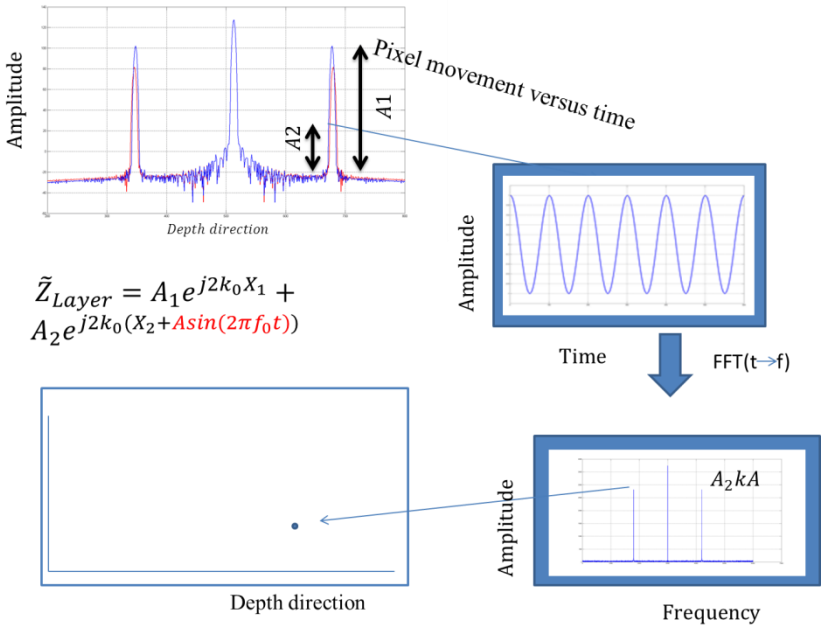

Figure 5-41 Reconstruction of the second layer, step 1. Each data corresponds to the amplitude variation at specific depth z.

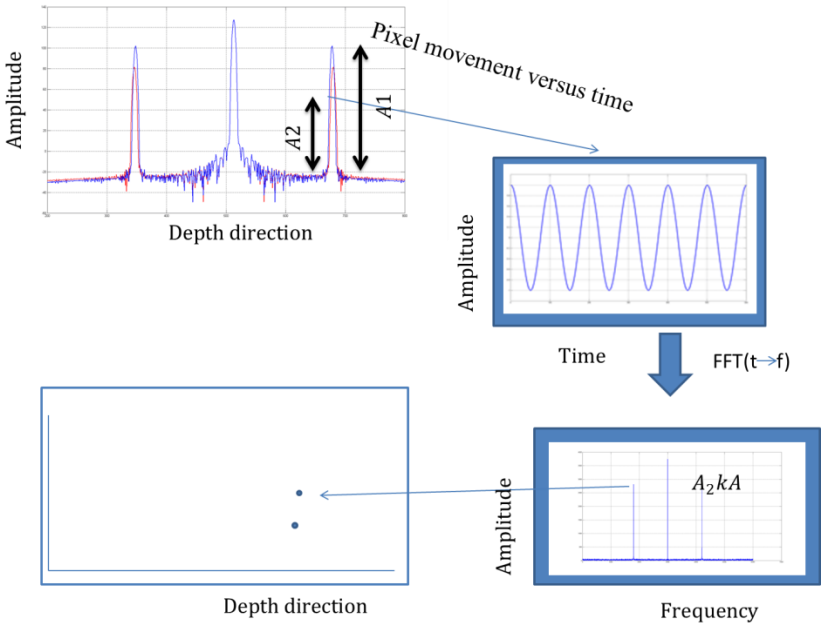

Figure 5-42 Reconstruction of the second layer, step 2

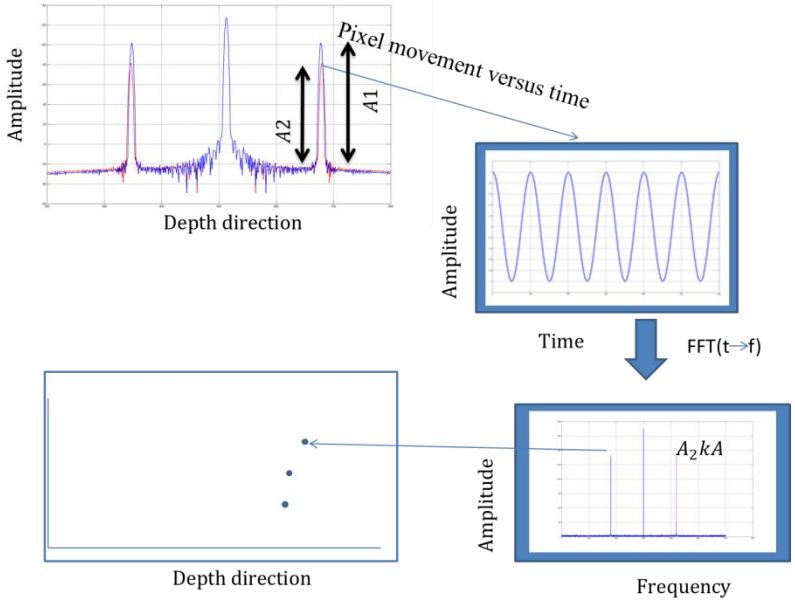

Figure 5-43 *Reconstruction of the second layer, step 3*

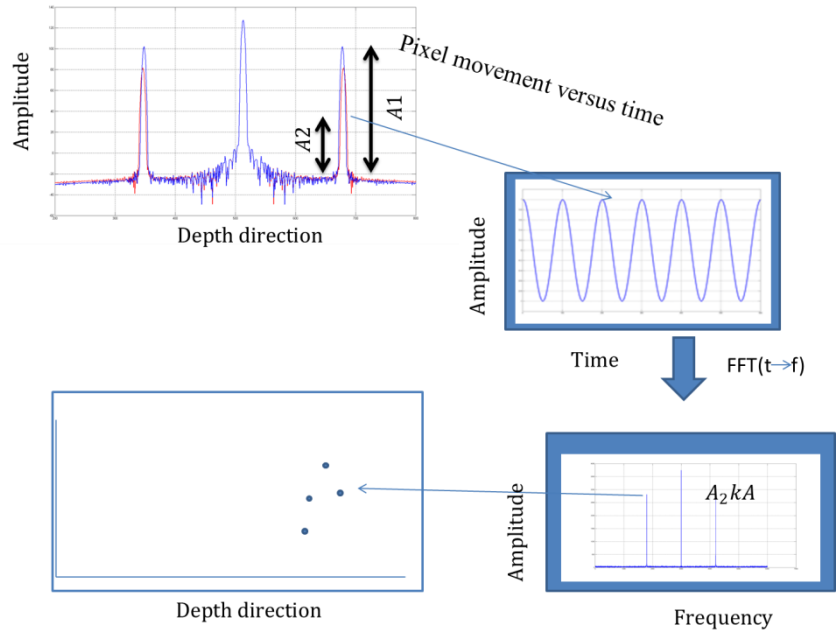

Figure 5-44 Reconstruction of the second layer, step 4

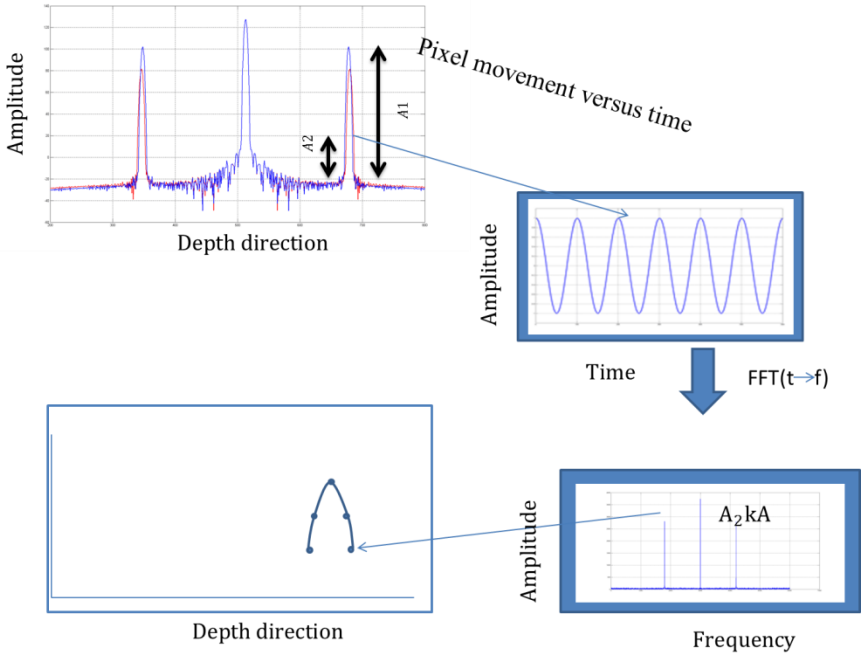

Figure 5-45 Reconstruction of the second layer, step 5

Appendix B. Unbalanced case: Eq (4.33) to (4.34)

We have to split the integral in the equation (4.33) into 3 parts:

The first can be calculated easily and it is equal to

$$\sqrt{\frac{\pi}{2}}\left(a_1{}^4 u + a_2{}^4 h\right)\sin^2(2\theta) \qquad (0.4.50)$$

In order to compute the second integral we have to rewrite $e^{-2\left(\frac{t^2}{u^2}+\frac{(t-m_1)^2}{h^2}\right)}$ as follows:

$$2\left(\frac{t^2}{u^2}+\frac{t^2+m_1{}^2-2m_1 t}{h^2}\right)=\frac{2}{u^2h^2}\left(h^2t^2+u^2t^2+u^2m_1{}^2-2u^2m_1 t\right)$$

$$=\frac{2\left(h^2+u^2\right)}{u^2h^2}\left(t^2-2\frac{u^2m_1 t}{u^2+h^2}+\frac{m_1{}^2u^4}{(u^2+h^2)^2}-\frac{m_1{}^2u^4}{(u^2+h^2)^2}+\frac{u^2m_1{}^2}{h^2+u^2}\right)$$

$$=\frac{2\left(h^2+u^2\right)}{u^2h^2}\left(\left(t-\frac{u^2m_1}{u^2+h^2}\right)^2+\frac{u^2m_1{}^2h^2}{h^2+u^2}\right)$$

$$=\frac{2\left(h^2+u^2\right)}{u^2h^2}\left(t-\frac{u^2m_1}{u^2+h^2}\right)^2+\frac{2m_1{}^2}{h^2+u^2}$$

We note $\frac{1}{g_1{}^2}=\frac{2(h^2+u^2)}{u^2h^2}; n_1=\frac{m_1u^2}{h^2+u^2}$

Therefore *(II)* becomes

$$=-2a_1{}^2a_2{}^2e^{-\frac{2m_1{}^2}{u^2+h^2}}\int_{-\infty}^{+\infty}e^{-\frac{(t-n_1)^2}{g_1{}^2}}\begin{pmatrix}\cos\left(2m_2+2\alpha(t-m_1)^2\right)\sin^2(2\theta)\\-2\cos^2(2\theta)\end{pmatrix}dt$$

By changing the t variable with $t'=t-n_1$, *(II)* becomes

$$= -2a_1{}^2 a_2{}^2 e^{-\frac{2m_1{}^2}{u^2+h^2}} \int_{-\infty}^{+\infty} \left(\begin{array}{l} e^{-\frac{t'^2}{g_1{}^2}} \cos\left(2m_2 + 2\alpha(t' + n_1 - m_1)^2\right) \sin^2(2\theta) - \\ 2e^{-\frac{t'^2}{g_1{}^2}} \cos^2(2\theta) \end{array} \right) dt'$$

We note $l_1 = n_1 - m_1$ and we use $\cos x = \frac{e^{jx} + e^{-jx}}{2}$

(*II*)

$$= -2a_1{}^2 a_2{}^2 e^{-\frac{2m_1{}^2}{u^2+h^2}} \int_{-\infty}^{+\infty} \left(\frac{1}{2} \left(\begin{array}{l} e^{-\frac{t'^2}{g_1{}^2} + j\left(2m_2 + 2\alpha(t'+l_1)^2\right)} \\ e^{-\frac{t'^2}{g_1{}^2} - j\left(2m_2 + 2\alpha(t'+l_1)^2\right)} \end{array} \right) + \sin^2(2\theta) - 2e^{-\frac{t'^2}{g_1{}^2}} \cos^2(2\theta) \right) dt'$$

Let's note $A_1 = \int_{-\infty}^{+\infty} \frac{1}{2} e^{-\frac{t'^2}{g_1{}^2} + j\left(2m_2 + 2\alpha(t'+l_1)^2\right)} dt' = \frac{e^{-\frac{2\alpha l_1{}^2}{j + 2\alpha g_1{}^2} + 2jm_2}}{2\sqrt{-2j\alpha + 1/g_1{}^2}} . \sqrt{\pi}$

Therefore (*II)*

$$= -2a_1{}^2 a_2{}^2 e^{-\frac{2m_1{}^2}{u^2+h^2}} \left(2\,\mathrm{Re}(A_1) \sin^2(2\theta) - 2g_1\sqrt{\pi} \cos^2(2\theta) \right)$$

To develop this term we have to calculate Re (A_1):

$$\frac{g_1\sqrt{\pi}}{2} \frac{e^{-\frac{2\alpha l_1{}^2}{j + 2\alpha g_1{}^2} + 2jm_2}}{2\sqrt{-2j\alpha + 1/g_1{}^2}} = \frac{g_1\sqrt{\pi}}{2} \cdot \frac{e^{-\frac{4\alpha^2 g_1{}^2 l_1{}^2}{1+4\alpha^2 g_1{}^4}} e^{j\left(2m_2 + \frac{2\alpha l_1{}^2}{1+4\alpha^2 g_1{}^4}\right)}}{\sqrt{\frac{1+f_1}{2}} - j\sqrt{\frac{f_1 - 1}{2}}}$$

where $f_1 = \sqrt{1 + 4\alpha^2 g_1{}^4}$

$$\text{Therefore } \mathrm{Re}(A_1)=\frac{g_1\sqrt{\pi}}{2f_1}e^{-\frac{4\alpha^2 g_1^{\,2}l_1^{\,2}}{1+4\alpha^2 g_1^{\,4}}}\left(\begin{array}{l}\cos\left(2m_2+\dfrac{2\alpha l_1^{\,2}}{1+4\alpha^2 g_1^{\,4}}\right)\sqrt{\dfrac{f_1+1}{2}}-\\ \sin\left(2m_2+\dfrac{2\alpha l_1^{\,2}}{1+4\alpha^2 g_1^{\,4}}\right)\sqrt{\dfrac{f_1-1}{2}}\end{array}\right)$$

Finally the second integral (*II):*

$$=-2a_1^{\,2}a_2^{\,2}g_1e^{-\frac{2m_1^2}{u^2+h^2}}\left(\begin{array}{l}\dfrac{\sqrt{\pi}}{f_1}e^{-\frac{4\alpha^2 g_1^{\,2}l_1^{\,2}}{1+4\alpha^2 g_1^{\,4}}}\left(\left(\begin{array}{l}\cos\left(2m_2+\dfrac{2\alpha l_1^{\,2}}{f_1^{\,2}}\right)\sqrt{\dfrac{f_1+1}{2}}-\\ \sin\left(2m_2+\dfrac{2\alpha l_1^{\,2}}{f_1^{\,2}}\right)\sqrt{\dfrac{f_1-1}{2}}\end{array}\right)\sin^2(2\theta)\right)\\ -2\sqrt{\pi}\cos^2(2\theta)\end{array}\right)$$

(0.4.51)

Now we have to compute the (*III)* integral

$$(III)=-2a_1a_2\sin(4\theta)\int_{-\infty}^{+\infty}\cos(m_2+\alpha(t-m_1)^2)\left(\begin{array}{l}a_1^{\,2}e^{-\left(3\frac{t^2}{u^2}+\frac{(t-m_1)^2}{h^2}\right)}-\\ a_2^{\,2}e^{-\left(\frac{t^2}{u^2}+3\frac{(t-m_1)^2}{h^2}\right)}\end{array}\right)dt$$

We split this integral into two parts

$$(III\text{-}a)=\int_{-\infty}^{+\infty}a_1^{\,2}\cos(m_2+\alpha(t-m_1)^2)e^{-\left(3\frac{t^2}{u^2}+\frac{(t-m_1)^2}{h^2}\right)}dt$$

We use that $\dfrac{3t^2}{u^2}+\dfrac{(t-m_1)^2}{h^2}=\dfrac{3h^2+u^2}{u^2h^2}\left(t-\dfrac{m_1u^2}{3h^2+u^2}\right)^2+\dfrac{3m_1^{\,2}}{u^2+3h^2}$

We note $\dfrac{1}{g_2^{\,2}}=\dfrac{3h^2+u^2}{u^2h^2};n_2=\dfrac{m_1u^2}{3h^2+u^2}$

$$(III\text{-}a)=a_1^{\,2}e^{-\frac{3m_1^2}{u^2+3h^2}}\int_{-\infty}^{+\infty}\left(e^{-\frac{(t-n_2)^2}{g_2^{\,2}}}\cos\left(m_2+\alpha(t-m_1)^2\right)\right)dt$$

And by using $t' = t - n_2$ we get

$$(III\text{-}a) = a_1{}^2 e^{-\frac{3m_1{}^2}{u^2+3h^2}} \int_{-\infty}^{+\infty} \left(e^{-\frac{t'^2}{g_2{}^2}} \cos\left(m_2 + \alpha(t' + n_2 - m_1)^2 \right) \right) dt'$$

We note $l_2 = n_2 - m_1$ and we use $\cos x = \frac{e^{jx} + e^{-jx}}{2}$

$$(III\text{-}a) = a_1{}^2 e^{-\frac{3m_1{}^2}{u^2+3h^2}} \int_{-\infty}^{+\infty} \left(\frac{1}{2} e^{-\frac{t'^2}{g_2{}^2} + j\left(m_2 + \alpha(t'+l_2)^2\right)} + \frac{1}{2} e^{-\frac{t'^2}{g_2{}^2} - j\left(m_2 + \alpha(t'+l_2)^2\right)} \right) dt'$$

We note $A_2 = \int_{-\infty}^{+\infty} \frac{1}{2} e^{-\frac{t'^2}{g_2{}^2} + j\left(m_2 + \alpha(t'+l_2)^2\right)} dt' = \frac{e^{-\frac{\alpha l_1{}^2}{j+\alpha g_1{}^2} + jm_2}}{2\sqrt{-j\alpha + 1/g_1{}^2}} . \sqrt{\pi}$

As a result (*III-a)* becomes

$$= a_1{}^2 e^{-\frac{3m_1{}^2}{u^2+3h^2}} . 2\,\mathrm{Re}(A_2)$$

$$= a_1{}^2 e^{-\frac{3m_1{}^2}{u^2+3h^2}} \frac{g_2\sqrt{\pi}}{f_2} e^{-\frac{\alpha^2 g_2{}^2 l_2{}^2}{1+\alpha^2 g_2{}^4}} \left(\cos\left(m_2 + \frac{\alpha l_2{}^2}{f_2{}^2} \right) \sqrt{\frac{f_2+1}{2}} - \sin\left(m_2 + \frac{\alpha l_2{}^2}{f_2{}^2} \right) \sqrt{\frac{f_2-1}{2}} \right)$$

(0.4.52)

where $f_2 = \sqrt{1 + \alpha^2 g_2{}^4}$

(*III-b)* can be obtained similarly and the result is

$$= a_2{}^2 e^{-\frac{3m_1{}^2}{3u^2+h^2}} \frac{g_3\sqrt{\pi}}{f_3} e^{-\frac{\alpha^2 g_3{}^2 l_3{}^2}{1+\alpha^2 g_3{}^4}} \begin{pmatrix} \cos\left(m_2 + \frac{\alpha l_3{}^2}{f_3{}^2}\right)\sqrt{\frac{f_3+1}{2}} - \\ \sin\left(m_2 + \frac{\alpha l_3{}^2}{f_3{}^2}\right)\sqrt{\frac{f_3-1}{2}} \end{pmatrix}$$

(0.4.53)

where $f_3 = \sqrt{1+\alpha^2 g_3{}^4}; l_3 = n_3 - m_1; \frac{1}{g_3{}^2} = \frac{h^2+3u^2}{u^2 h^2}; n_3 = \frac{3m_1 u^2}{h^2+3u^2}$

Therefore (*III)* becomes

$$= 2a_1 a_2 \sin(4\theta) \left[\begin{array}{l} a_1{}^2 e^{-\frac{3m_1{}^2}{u^2+3h^2}} \frac{g_2\sqrt{\pi}}{f_2} e^{-\frac{\alpha^2 g_2{}^2 l_2{}^2}{1+\alpha^2 g_2{}^4}} \begin{pmatrix} \cos\left(m_2 + \frac{\alpha l_2{}^2}{f_2{}^2}\right)\sqrt{\frac{f_2+1}{2}} - \\ \sin\left(m_2 + \frac{\alpha l_2{}^2}{f_2{}^2}\right)\sqrt{\frac{f_2-1}{2}} \end{pmatrix} \\ -a_2{}^2 e^{-\frac{3m_1{}^2}{3u^2+h^2}} \frac{g_3\sqrt{\pi}}{f_3} e^{-\frac{\alpha^2 g_3{}^2 l_3{}^2}{1+\alpha^2 g_3{}^4}} \begin{pmatrix} \cos\left(m_2 + \frac{\alpha l_3{}^2}{f_3{}^2}\right)\sqrt{\frac{f_3+1}{2}} - \\ \sin\left(m_2 + \frac{\alpha l_3{}^2}{f_3{}^2}\right)\sqrt{\frac{f_3-1}{2}} \end{pmatrix} \end{array} \right]$$

(0.4.54)

So the final expression of the autocorrelation function in the case of dispersion:

$$G(\tau) \propto \sqrt{\frac{\pi}{2}}\left(a_1^{\,4}u + a_2^{\,4}h\right)\sin^2(2\theta)$$

$$-2a_1^{\,2}a_2^{\,2}g_1 e^{-\frac{2m_1^{\,2}}{u^2+h^2}}\begin{pmatrix}\dfrac{\sqrt{\pi}}{f_1}e^{-\frac{4\alpha^2 g_1^{\,2}l_1^{\,2}}{1+4\alpha^2 g_1^{\,4}}}\left(\begin{pmatrix}\cos\left(2m_2+\dfrac{2\alpha l_1^{\,2}}{f_1^{\,2}}\right)\sqrt{\dfrac{f_1+1}{2}}-\\ \sin\left(2m_2+\dfrac{2\alpha l_1^{\,2}}{f_1^{\,2}}\right)\sqrt{\dfrac{f_1-1}{2}}\end{pmatrix}\sin^2(2\theta)\right)\\ -2\sqrt{\pi}\cos^2(2\theta)\end{pmatrix}$$

$$+2a_1a_2\sin(4\theta)\begin{bmatrix}a_1^{\,2}e^{-\frac{3m_1^{\,2}}{u^2+3h^2}}\dfrac{g_2\sqrt{\pi}}{f_2}e^{-\frac{\alpha^2 g_2^{\,2}l_2^{\,2}}{1+\alpha^2 g_2^{\,4}}}\begin{pmatrix}\cos\left(m_2+\dfrac{\alpha l_2^{\,2}}{f_2^{\,2}}\right)\sqrt{\dfrac{f_2+1}{2}}-\\ \sin\left(m_2+\dfrac{\alpha l_2^{\,2}}{f_2^{\,2}}\right)\sqrt{\dfrac{f_2-1}{2}}\end{pmatrix}\\ -a_2^{\,2}e^{-\frac{3m_1^{\,2}}{3u^2+h^2}}\dfrac{g_3\sqrt{\pi}}{f_3}e^{-\frac{\alpha^2 g_3^{\,2}l_3^{\,2}}{1+\alpha^2 g_3^{\,4}}}\begin{pmatrix}\cos\left(m_2+\dfrac{\alpha l_3^{\,2}}{f_3^{\,2}}\right)\sqrt{\dfrac{f_3+1}{2}}-\\ \sin\left(m_2+\dfrac{\alpha l_3^{\,2}}{f_3^{\,2}}\right)\sqrt{\dfrac{f_3-1}{2}}\end{pmatrix}\end{bmatrix}$$

(0.4.55)

Appendix C. Autocorrelation function for both asymmetry and unbalanced return field

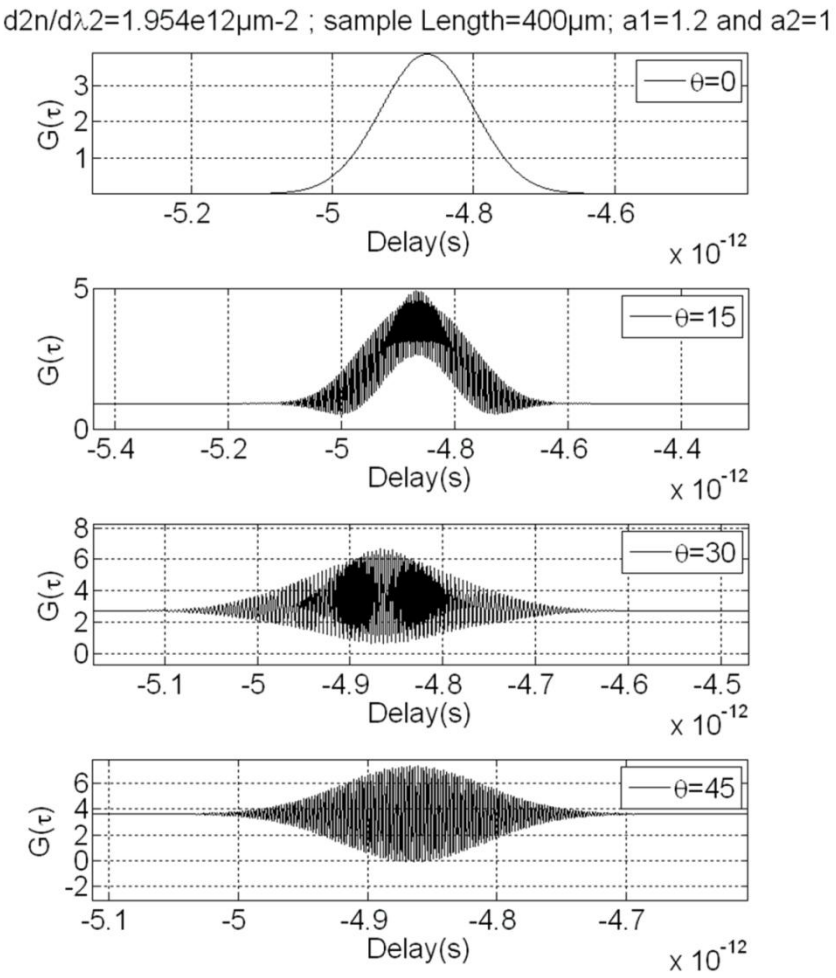

Figure 5-46 Autocorrelation function when dispersion unbalanced return field are taken into consideration. $d^2n/d\lambda^2 = 1.95x10^{12}\mu m^{-2}$

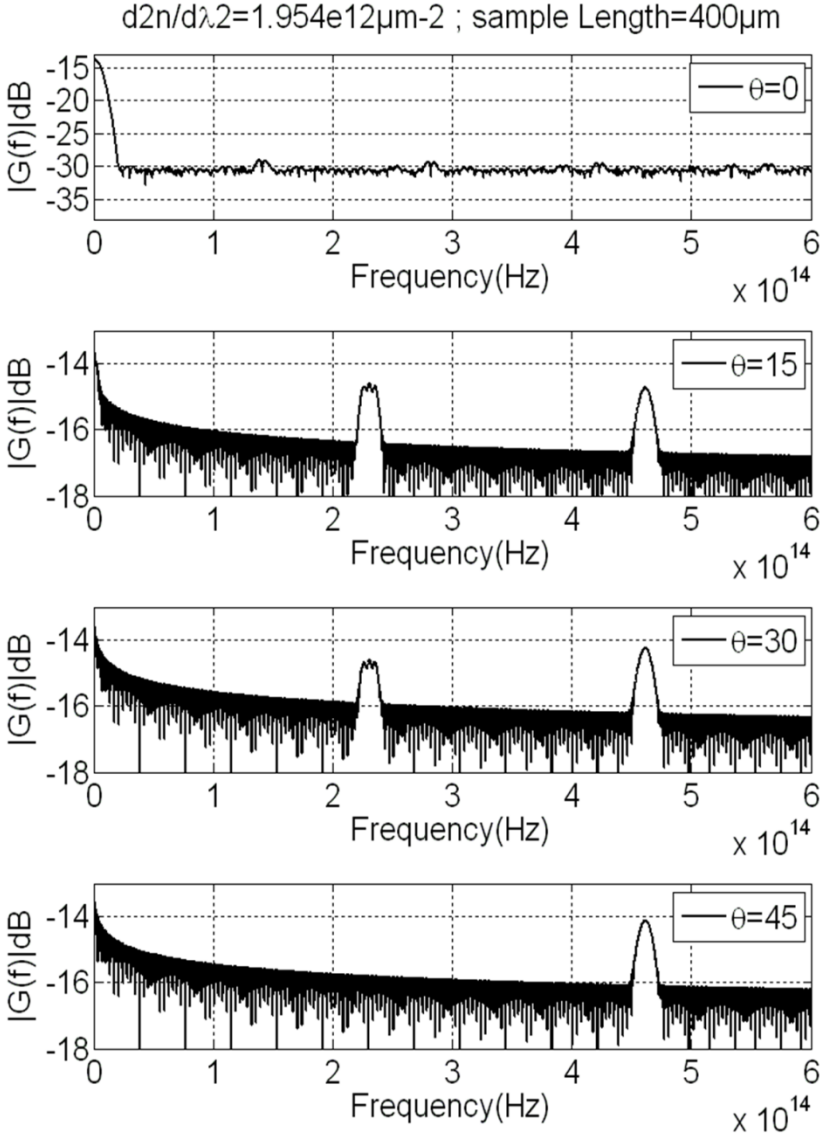

Figure 5-47 Fourier transform of the autocorrelation function when the dispersion and unbalanced return field are taken into account. $d^2n/d\lambda^2 = 1.95x10^{13}\mu m^{-2}$

Appendix D. TDOCT VS FDOCT

Time Domain Optical Coherence Tomography	Fourier Domain Optical coherence Tomography
• Movable sample arm • Limited acquisition speed • Photo-detector • Lower sensitivity	• Fixed sample arm • Faster acquisition speed • CCD camera detector • Better sensitivity(+10dB)

Appendix E. Fourier transform of the autocorrelation function using the formula (4.18)

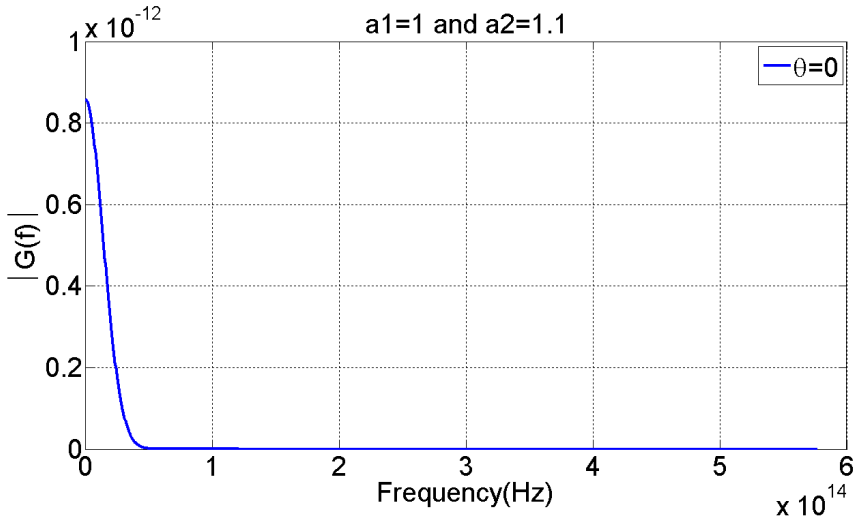

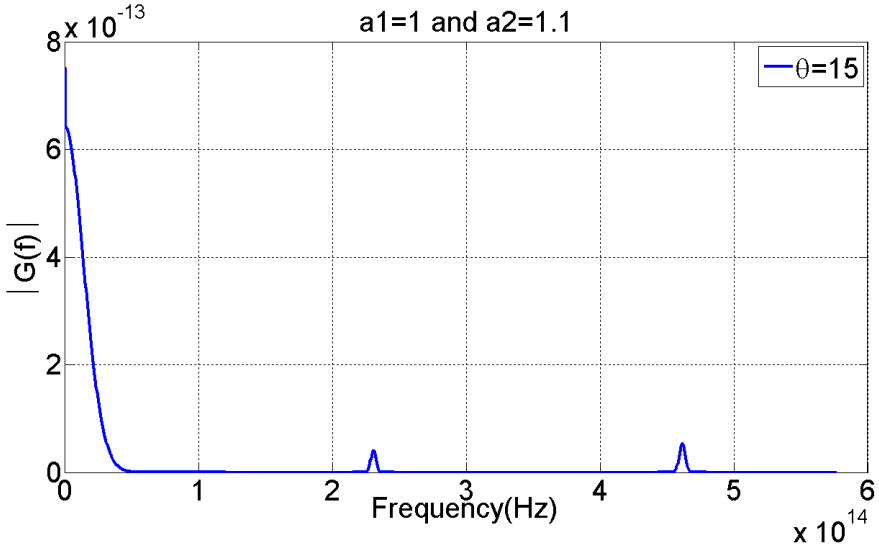

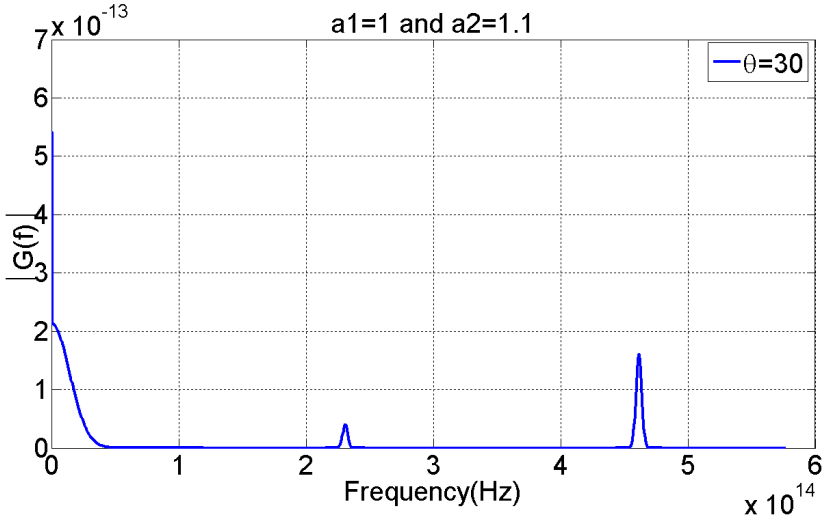
a1=1 and a2=1.1
x 10^-13
θ=30
|G(f)|
Frequency(Hz)
x 10^14

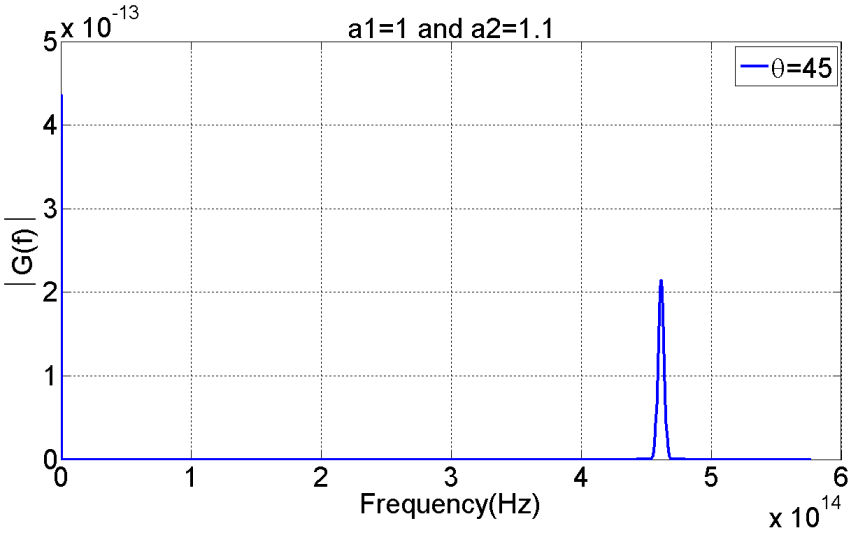
a1=1 and a2=1.1
x 10^-13
θ=45
|G(f)|
Frequency(Hz)
x 10^14